

Old Dominion University

ODU Digital Commons

Electrical & Computer Engineering Theses & Dissertations

Electrical & Computer Engineering

Spring 2020

Diagnostic Studies of Non-Thermal Atmospheric Pressure Nanosecond Plasma Jets

Shutong Song

Old Dominion University, ssong003@odu.edu

Follow this and additional works at: https://digitalcommons.odu.edu/ece_etds



Part of the [Electrical and Computer Engineering Commons](#)

Recommended Citation

Song, Shutong. "Diagnostic Studies of Non-Thermal Atmospheric Pressure Nanosecond Plasma Jets" (2020). Doctor of Philosophy (PhD), Dissertation, Electrical & Computer Engineering, Old Dominion University, DOI: 10.25777/c38j-st04
https://digitalcommons.odu.edu/ece_etds/217

This Dissertation is brought to you for free and open access by the Electrical & Computer Engineering at ODU Digital Commons. It has been accepted for inclusion in Electrical & Computer Engineering Theses & Dissertations by an authorized administrator of ODU Digital Commons. For more information, please contact digitalcommons@odu.edu.

DIAGNOSTIC STUDIES OF NON-THERMAL ATMOSPHERIC PRESSURE NANOSECOND PLASMA JETS

by

Shutong Song

M.S. March 2013, Donghua University, China

B.S. July 2010, Donghua University, China

A Dissertation Submitted to the Faculty of Old Dominion
University in Partial Fulfillment of the Requirements for the
Degree of

DOCTOR OF PHILOSOPHY

ELECTRICAL AND COMPUTER ENGINEERING

Old Dominion University

May 2020

Approved by:

Chunqi Jiang (Director)

Lepsha Vuskovic (Member)

Shirshak Dhali (Member)

Shu Xiao (Member)

Abstract

Diagnostic Studies of Non-thermal Atmospheric Pressure Nanosecond Plasma Jets

Non-thermal atmospheric pressure plasma jets attract a lot of attentions due to its growing interest in plasma medicine. In this study, reactive species (e.g. excited He, O, OH) in a helium single-electrode non-thermal atmospheric pressure nanosecond plasma jet (APNPJ) driven by a nanosecond pulsed power supply have been studied via electrical measurements (e.g. voltage, current) and optical emission spectroscopy. It is shown that the gas temperature of the APNPJs remained near 300 ± 50 K by fitting $N_2(C-B)$ second positive system and OH(A-X) emission spectrum. Higher excited N_2^+ (by a factor of 1.3) but less excited N_2 , He, O, and OH productions are observed when compared two APNPJs driven by a short pulse (5 ns pulse width) and a long pulse (164 ns), respectively. Importantly, comparable or more excited species were produced by the 5-ns pulsed plasma for the first 100 ns which implies shorter rise time of a pulsed voltage can influence the plasma chemistry by boosting the production of excited species. Further studies indicate that enhanced ionization near the single-electrode nozzle, earlier streamer formation and stronger emissions by excited N_2 , N_2^+ , OH, and O are observed when the 164-ns plasma jet impinges onto the water surface. Interestingly, maximal OH(A-X) emissions are obtained at pulse width of 600 – 800 ns when a plasma jet impinges onto the water surface with examining of pulse widths from 200 ns to 5000 ns at 7 kV, 200 ns at 1 kHz. More importantly, temporally-resolved emission spectroscopy shows that more than 40% OH(A-X) emissions is produced during the first 200 ns of the voltage pulse regardless of the pulse width.

Plume dynamics indicate that increasing both amplitude (ranging from 5 kV to 10 kV) and helium flow rate (from 8 SCCM to 164 SCCM) resulted in faster propagation of ionization fronts

hence longer plasma plumes, meanwhile, higher repetition rate (from 10 Hz to 4 kHz) and longer pulse width (from 200 ns to 990 μ s) created earlier inception of ionization fronts but shorter plume lengths. Study of repeatability of both air corona discharge and plasma jets pertinent to breakdown probability are investigated in further details.

Acknowledgements

I would like to thank my committees Dr. Lepsha Vuskovic, Dr. Shirshak Dhali, Dr. Shu Xiao, and especially my advisor Dr. Chunqi Jiang. This dissertation would not be possible without their valuable suggestions and comments.

My sincere thanks to Dr. Esin B. Sozer who provided a lot of help on designing experiments on our collaborated research. I would like to express my sincere thanks to Dr. Jamie Lane who navigated me through a lot of experimental designs and data manipulation skills.

Copyright, 2020, by Shutong Song, All Rights Reserved

TABLE OF CONTENTS

LIST OF TABLES.....	vi
LIST OF FIGURES.....	vii
 I. CHAPTER 1 INTRODUCTION	
1-1. Brief introduction of gas discharge.....	1
1-2. An introduction to non-thermal atmospheric pressure plasma jets.....	2
1-3. Topics covered in this research.....	5
1-4. Experimental methods.....	17
 II. CHAPTER 2 DIAGNOSTICS OF REACTIVE SPECIES IN ATMOSPHERIC PRESSURE NANOSECOND PLASMA JETS	
4-1. Abstract.....	23
4-2. Study of spatiotemporally-resolved optical emissions between a long (164 ns) and short (5 ns) nanosecond plasma jets.....	24
4-3. Comparison study of spatiotemporally resolved emissions in APNPJs with and without water.....	30
4-4. Evaluation of pulse width on effect of OH(A-X) in APNPJs impinged onto water.....	36
 III. CHAPTER 3 CHARACTERISTICS OF ATMOSPHERIC PRESSURE NANOSECOND PLASMA JETS	
3-1. Abstract.....	41
3-2. Properties of a plasma plume in APNPJs.....	42
3-3. Effects of operation parameters on ‘guided streamer’ in ambient air... ..	52
 IV. CHAPTER 4 ELECTRICAL BREAKDOWN IN AIR CORONA AND ATMOSPHERIC PRESSURE NANOSECOND PLASMA JETS	
2-1. Abstract.....	60
2-2. A general observation of breakdown in APNPJs.....	61
2-3. Breakdown in corona discharges.....	63
2-4. Breakdown in APNPJs.....	73
2-5. Inception of air corona and plasma jets.....	42
V. CHAPTER 5 CONCLUSIONS.....	78
VI. APPENDIX A VOLTAGE CURRENT MEANSUREMENTS.....	80
VII. APPENDIX B PERMISSIONS FROM THE COPYRIGHT HOLDER	85
VIII. REFERENCES.....	86
VITA.....	92

LIST OF TABLES

Table	Page
2-1. Maximum intensity of identified species from Fig. 2-3 for both 5 ns and 164 ns pulses.....vi	vi
2-2. Maximum emission intensities of reactive species from Fig. 2-8.....vii	vii
4-1. Excitation energy, lifetime and excitation cross sections of atoms and molecules.....viii	viii

LIST OF FIGURES

Figure	Page
1-1. A plasma jet by a single-needle electrode powered by 8 kV, 200 ns pulses at 500 Hz with helium flow of 200 SCCM, diameter of the needle tip is 0.508 mm.....	3
1-2. A nanosecond plasma jet in ambient air driven by 7 kV, 200 ns at 1 kHz with helium flow of 70 SCCM. Time indicated here correspond to time of a voltage pulse in Fig. 3-3 (a), each image is at exposure time of 5 ns with combination of 100 frames.....	4
1-3. (a) Electric field distribution caused by space charge (E') and external electric field (E_0) and (b) the resultant total electric field ($E = E_0 + E'$).....	8
1-4. (a) Cathode-directed streamer with two consecutive times ($t_2 > t_1$) and (b) the electric field distribution at the streamer head.....	9
1-5. An electron avalanche at two consecutive time, external electric field E_0 and electron drift direction with drift velocity V_d	11
1-6. Ionization coefficient for a wide range of gases (a) molecules and (b) inertial gases.....	12
1-7. Breakdown potentials on various gases over a wide range of pd values.....	13
1-8. Voltage-current characteristics of a typical discharge between two parallel plates.....	14
2-1. (a) Schematic of optical emission spectroscopy for nanosecond pulsed plasma jets and (b) a plasma plume with short pulse (5 ns pulse width).....	25
2-2. Voltage and current waveforms of pulsed plasma jet at 8 kV with pulse width of (a) 5 ns and (b) 164 ns at 500 Hz.....	26
2-3. Total emission spectra of APNPJs integrated along the axial direction.....	27

2-4. (a) Normalized emissions of excited species N_2 , He, O, OH, and N_2^+ for the 5 ns pulse (red dot) and 164 ns pulse (blue solid) along the axial direction. Jet nozzle is at $z = 0$. (b) Spatiotemporal distributions of identified species at two different delay time indicated in Fig. 2-2 for 5 ns and 164 ns pulsed plasma jets.....	28
2-5. Experimental and simulation emission spectra of N_2 second positive system $N_2(C^3\Pi_u - B^3\Pi_g)$ (a) at (0-0) band for rotational temperature and (b) at $\Delta v = 2$ transitions for vibrational temperature.....	29
2-6. (a) Experimental setup of optical emission spectroscopy for APNPJ and (b) a helium jet impinged onto the water surface, the gap from nozzle to water surface is 10 mm.....	31
2-7. Voltage (black solid line) and jet currents of APNPJs interacting with (red solid line) and without water (blue dot line).....	32
2-8. Integrated optical emission spectroscopy along the axial direction for APNPJs (a) with and (b) without water.....	33
2-9. Comparison of identified species spatiotemporally-wise for APNPJs with and without interacting with water. (a) N_2 , (c) N_2^+ , (e) He, (g) OH and (i) O are identified species without water. (b) N_2 , (d) N_2^+ , (f) He, (h) OH and (j) O are corresponding species with water.....	34
2-10. (a) Voltage waveforms with varying pulse width from 200 ns to 5000 ns and (b) jet currents from pulse width of 200 ns to 1000 ns with increment of 200 ns.....	37
2-11. Experimental (solid lines) and simulated (dot line) emission spectra of the OH(A-X) band for pulse widths ranging from 200 ns to 5000 ns.....	38

2-12. (a) Segmentation of a 600 ns pulse into four different phases: Primary-phase, Plateau-phase, Fall-phase and Post-decay and (b) Total OH(A-X) emission intensities at each phases with respect to the pulse width ranging from 200 ns to 5000 ns.....	39
3-1. Applying DC polarity (positive or negative voltage) beneath plasma jets, the DC power supply connected to a 7×7 cm ² copper plate with interelectrode gap of 2.5 cm.....	43
3-2. (a) Apply positive DC voltage and (b) apply negative DC voltage.....	44
3-3. Abnormal plume counts among total 50 under 200 ns at 4 kHz with He flow 400 SCCM with varying amplitude from 5 kV to 10 kV.....	45
3-4. Abnormal plume counts among total 50 under 10 kV, 200 ns with He flow 400 SCCM with varying repetition rate from 500 Hz to 5 kHz.....	46
3-5. Abnormal plume counts among total 50 under 10 kV, 200 ns at 4 kHz at He flow from 100 to 900 SCCM.....	46
3-6. Peak emission intensity from secondary discharge at 7 kV, 200 ns at 1 kHz with He flow of 70 SCCM with varying pulse width from 200 ns to 5000 ns.....	48
3-7. Emission intensities of secondary discharge during the falling edge of a voltage pulse with 7 kV, 200 ns at 1 kHz with varying He flow rate from 24 SCCM to 164 SCCM (too weak at He 8 SCCM).....	49
3-8. A dipole formed in the discharge gap with two parallel plate containing an electron avalanche, A and C are the anode and cathode, respectively.....	50

3-9. Initial emission intensities of secondary discharge during the falling edge of a voltage pulse with 7 kV, 200 ns at 1 kHz with varying pulse widths from 1000 ns to 5000 ns and He flow 70 SCCM.....	51
3-10. (a) Propagation distance of ionization front from nozzle and (b) fitted projectiles of propagation at different time regarding a voltage pulse of 200 ns at 1 kHz at He 70 SCCM with varying amplitude from 5 kV to 10 kV.....	53
3-11. (a) Voltage and (b) current waveforms with a voltage pulse of 200 ns at 1 kHz at He 70 SCCM with varying amplitude from 5 kV to 10 kV.....	53
3-12. (a) Propagation distance of ionization front from nozzle and (b) fitted projectiles of propagation regarding different time of a voltage pulse at 7 kV, 200 ns and 1 kHz with varying He flow rate from 8 SCCM to 164 SCCM.....	54
3-13. Current waveforms regarding a voltage pulse of 7 kV, 200 ns at 1 kHz with varying He flow rate from 8 SCCM to 164 SCCM.....	55
3-14. (a) Current waveforms and (b) propagation distance of ionization fronts with a voltage pulse of 7 kV, 200 ns at He 70 SCCM with varying repetition rate from 10 Hz to 4 kHz.....	56
3-15. (a) Current waveforms and (b) propagation distance of ionization fronts regarding voltage pulses of 7 kV, 200 ns at He 70 SCCM with varying pulse width from 200 ns to 990 μ s.....	57
3-16. (a) Current waveforms and (b) propagation of ionization fronts regarding voltage pulses of 7 kV, 200 ns at He 70 SCCM with varying needle diameters.....	58
4-1. Experimental setup of a nanosecond pulsed corona discharge in ambient air without He flow.....	62

4-2. Typical discharge from single-needle electrode (a) corona discharge in ambient air and (b) plasma jet imping into ambient air with He flow of 70 SCCM, both at 10 kV, 200 ns pulses at 1 Hz.....	63
4-3. Breakdown probability of air corona with time at 8 kV, 200 ns pulse with 1 Hz.....	64
4-4. Breakdown probability of air corona versus time under normal discharge at 8 kV, 200 ns pulses with 1 Hz.....	65
4-5. Breakdown probability of air corona with time under excessive electrons at 8 kV, 200 ns pulses at 1 Hz. With pencil ignition for 15 seconds.....	66
4-6. Breakdown probability of air corona with time under with depletion electrons at 8 kV, 200 ns pulses at 1 Hz. with strong air flow 6 L/min, $d1=1$ mm, $d2=3$ mm, distance between exit of the air flow tubing to outer edge of the needle $d3=2.8$ cm.....	67
4-7. Breakdown probability of He plasma jet at 9 kV, 200 ns pulses at 1 Hz with varying He flow at 300 SCCM during the first 90 mins, 600 SCCM from 90 mins to 125 mins, 800 SCCM from 125 mins to 190 mins and 300 SCCM from 190 mins to 220 mins.....	68
4-8. Breakdown probability of air corona with varying amplitude (6 – 10 kV) for 200 ns pulses at 1 Hz, two repeated normal operations and one under excessive operation condition.....	70
4-9. Breakdown images of air corona with varying amplitude for 200 ns pulses at 1 Hz, single shot images (a) 8 kV, (b) 9 kV and (c) 10 kV.....	70
4-10. Breakdown probability of air corona with pulse width (200 – 5000 ns) at 7 kV pulses at 1 Hz.....	71

4-11. Breakdown images of air corona with varying pulse widths for 7 kV pulses at 1 Hz, single shot (a) 400 ns, (b) 1000 ns, (c) 3000 ns and (d) 4000 ns.....	71
Fig. 4-12. Breakdown probability of air corona with various repetition rate (3 – 6 kHz) at 7 kV, 200 ns pulses.....	72
4-13. Breakdown probability of plasma jet with varying amplitude (5 – 10 kV) for 200 ns pulses at 1 Hz with He flow 70 SCCM.....	73
4-14. Breakdown images of plasma jet with varying amplitude for 200 ns pulses at 1 Hz with He flow 70 SCCM with (a) 7 kV, (b) 8 kV, (c) 9 kV and (d) 10 kV.....	74
4-15. Breakdown probability of air corona with repetition rate (1 – 1000 Hz) at 7 kV, 200 ns pulses.....	74
4-16. Breakdown images of plasma jet with repetition rate at 7 kV, 200 ns pulses (a) 1 Hz, (b) 10 Hz, (c) 100 Hz, (d) 1000 Hz and (e) 5000 Hz.....	75
4-17. Breakdown probability of plasma jet with pulse width (200 – 1000 ns) at 7 kV, 1 Hz with 200 ns to 1000 ns.....	76
4-18. Breakdown images of plasma jet with pulse width at 7 kV, 1 Hz with (a) 200 ns, (b) 1000 ns and (c) 5000 ns.....	76
4-19. Breakdown probability of plasma jet at 7 kV, 200 ns at 1 Hz with He flow rate from 35 SCCM to 200 SCCM.....	77
4-20. Breakdown images of plasma jet at 7 kV, 200 ns pulses at 1 Hz with varying flow rate (a) 35 SCCM, (b) 70 SCCM, (c) 100 SCCM, (d) 150 SCCM and (e) 200 SCCM.....	77

A1. Coaxial cable through two ferrites (left) and Coaxial cable through a ferrite clamp (right).....	81
A2. (a) Experimental setup for current measurement at 8 kV, 200 ns pulse at 1 kHz with He flow rate at 164 SCCM and (b) currents measured from plasma jets using Pearson 6585 with (black solid line) and without (red solid line) two ferrite clamps.....	81
A3. (a) Experimental setup for current measurement (black line is ground wire, red is the center core) and (b) the equivalent circuit of (a).....	82
A4. Current measured using Pearson 6585 as in Fig. 3(a) with (black solid line) and without (red solid line) connecting to the transmission line shield.....	83
A5. Comparison of coaxial cable RG 58/U and 58 C/U with specifications.....	83
A6. Currents measured using Pearson 6585 with coaxial cable RG 58/U (black solid line) and 58 C/U (red solid line).....	84

Chapter 1

INTRODUCTION

1-1. BRIEF INTRODUCTION OF GAS DISCHARGE

It is probably more intuitive to start with a nature phenomenon ‘lightening’. Separation of positive and negative charges in the cloud results in a strong electric field which leads to breakdown in air. The lightening is often zigzag and branching out in a random manner with luminous heads (called ‘ionization fronts’) propagating at speeds in the level of $10^7 \sim 10^8$ m/s. This is a discharge in the form of a ‘leader’. The main focus of this research, however, is breakdown and development of streamer discharge which resembles the leader discharge. The principle difference between a leader and a streamer lies in the properties of the two plasmas. That is, a streamer tends to lose its conductivity in the bulk plasma due to attachment while leader does not [1]. Illuminations around the sharp edges of high power transmission lines are thought to be a streamer (called ‘corona discharge’).

Corona discharge can be observed in a highly non-uniform electric field (i.e. the electric field near electrodes has to be much higher than rest of the discharge gap). If it is a single positive electrode with sharp edges, positive corona (‘cathode-directed streamer’) is generated. Multiple thin ionized channels will be observed near the electrode and flashing out like filaments. It is also in a zigzag and branching manner similar to the leader discharge if observed carefully. Depending on the structures of discharges at atmospheric pressure, discharges could be dominant by avalanche multiplications or streamers. If the discharge gap (i.e. anode-to-cathode distance) is not too large (roughly $d < 5$ cm and $pd < 4000$ Torr · cm), Townsend breakdown mechanism of avalanche

multiplication is predominant [1]. Generally, breakdown in air at atmospheric pressure goes via avalanche multiplication if $d < 5$ cm and via the streamer mechanism if $d > 6$ cm.

The two main mechanisms of discharge, namely, Townsend avalanche multiplications and streamer theory, which are probably the two most important theories in gas discharge. At low pressure and small overvoltage, Townsend avalanche multiplication is usually dominant, while at high pressure (large pd) and overvoltage, strong distortion of external electric field caused by space charges in the plasma essentially results in streamer discharge. Discharge mechanisms regarding the two theories are illustrated in detail in section 1-3.

Mechanisms of gas discharge concern with the formation and development of discharges while discharges itself extended much further in applications. For example, it is considered to be very important in modern life, such as plasma etching [2], food decontamination [3], biomedical applications (such as cancer cell treatment etc. [4, 5]), which are the core of modern technologies. Even though this research is mainly focused on fundamental research of gas discharge, the driven force from potential applications should not be underestimated. In fact, one would realize in chapter 2 that the study of hydroxyl radicals in a non-thermal atmospheric pressure plasma jet interacting with substrates is of great importance in plasma biomedical applications [6-9].

1-2. INTRODUCTION TO NON-THERMAL ATMOSPHERIC PRESSURE PLASMA JETS

Aforementioned non-thermal atmospheric pressure plasma jets may sound unfamiliar to you since it emerged in only about two decades ago [10]. Non-thermal atmospheric pressure plasma jets are plasmas produced by gas discharges, operating in non-confined electrodes, and projected

into the ambient air due to the gas flow (mostly noble gas). Three components, i.e. a jet device, a carrier gas and a power supply are necessary for generating a plasma jet. High voltage generated by power supply elevated the electric field near the electrode which breakdowns the flowing gas hence forming a visible plume in ambient air (Fig. 1-1). Design of jet devices is a rich field with practical applications (e.g. large plasma brush for surface decontamination, small needle-jet for root canal disinfection etc. [11, 12]). In principle, it can be categorized into dielectric barrier plasma jets (DBD-jets) and barrier-free plasma jets (corona-jets) [13]. Fig. 1-1 presents a corona type jet which consists of a single-needle hollow electrode with flowing helium driven by a pulsed power.



Fig. 1-1. A plasma jet by a single-needle electrode powered by 8 kV, 200 ns pulses at 500 Hz with helium flow of 200 SCCM, diameter of the needle tip is 0.508 mm.

Such plasma assisted by a gas flowing into ambient air that generates a visible plume in several centimeters. It is highly non-equilibrium (i.e. electron temperature is much higher than ions $T_e \gg T_i$). At atmospheric pressure, it is common to assume that a rotational Boltzmann distribution of molecules is at equilibrium with its surrounding gas (i.e. $T_{\text{rot}} = T_{\text{gas}}$) since the time constant of a rotational energy transfer ($\sim 10^{-11}$ s) is much faster than its lifetime ($\sim 10^{-9}$ s). In chapter 2, gas temperature will be estimated via optical emission spectroscopy under such assumption. Excited $\text{N}_2(\text{C-B})$ and $\text{OH}(\text{A-X})$ will be employed with simulated gas temperature from their rotational spectrum. Generally, temperature of such plasmas is in the range of 300 - 1000 K which can be called ‘cold plasma jets’. In this research, all the plasma jets are cold plasmas at about 300 K which is around room temperature.

A pulsed helium plasma jet is violetish in ambient air. The color of the plume is determined by emissions from excited species in the plasma (dominant by excited nitrogen from ~ 300 nm to 400 nm for this plasma jet in Fig.1-1). Chapter 2 also investigates reactive species generated in plasma plume in detail. These continuous emissions, however, have a discrete nature if looked at with a high speed camera (in the time duration of nanosecond). As seen from Fig. 1-2, it acts like a discrete pack propagates away from the powered electrode. The small pack (also called ‘plasma bullet’) travels at a high speed $\sim 10^7$ m/s which is impossible to be detected by bare eyes.

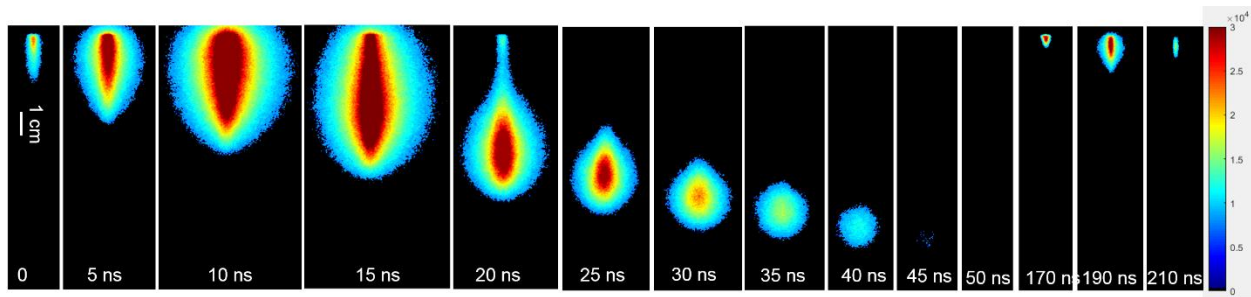


Fig. 1-2. A nanosecond plasma jet in ambient air driven by 7 kV, 200 ns at 1 kHz with helium flow of 70 SCCM. Time indicated here correspond to time of a voltage pulse in Fig. 3-3 (a), each image is at exposure time of 5 ns with combination of 100 frames.

This interesting phenomena of the plasma jet have been intensively studied for over ten years [13-15] due to several unique properties. At first glance, it is, in most cases, a uniform and straight plume without any branching; secondly, the ionization front travels at such high speed as a small pack and leaves a dark channel behind it as it propagates away from the electrode; thirdly, such propagation is somewhat highly repeatable in space and time from pulse to pulse (if powered by pulsed sources); fourthly, there are usually two discharge events that can be detected at the rising and falling phases of a voltage pulse (if pulse voltage is applied) which are called ‘primary discharge’ and ‘secondary discharge’, respectively. These properties (including bright bullet, dark channel, repeatability, uniform emissions (i.e. no filament branching), and multiple discharge events) are not only a rich research field for fundamental science (i.e. physics, mechanics and chemistry) but also provides great potential in many applications.

1-3. TOPICS COVERED IN THIS RESEARCH

A complete review of current progress of plasma bullet can be found in Ref. [15]. In short, results from various research groups support that the dark channel left behind of ionization front is somewhat conductive [16-18]. Study of seed electrons and photoionization on formation and propagation of ionization fronts showed that when it is lack of seed electrons, the role of photoionization is essential for propagation of ionization front [19-21]. However, most of these reports are from computational modeling due to the difficulties in experimental design. Both experimental and computational results were carried out to understand the effect of penning ionization on forming of donut shape of ionization fronts [22-24]. It is found that complete opposite

conclusions were drawn from these results. Some confirmed that the donut shape is attributed to Penning ionization while others showed that Penning ionization has a rather weak effect on forming of donut shape. Further investigation is required to clear this out. Study of repeatability and amorphousness of ionization fronts indicate that ionization fronts are not always repeatable in space and time. The repeatability is thought to relate to seed electrons provided by memory effect [25] and can be affected by repetition rate and flow rate [26-28].

Considering effects of operation parameters (i.e. pulse rise time, amplitude, repetition rate, pulse width, gas flow, gas mixture and electrode diameter), it is found that, on one hand, lower pulse repetition rate (PRR) increases plasma length from 1 to 75 Hz and then keeps almost constant [29]; on the other hand, results shown that higher repetition rates lead to higher propagation velocity hence leading to longer plasma plume [30]. Generally, it is assumed that shorter rise time of a pulsed voltage could result in overvoltage breakdown which further enhances excitation and ionization process in plasma. Research has shown that shorter pulse rise time and faster propagation of ionization front is associated with longer plasma plume [31]. However, when pulse rise time is reduced further from 150 ns to 10 ns in a dielectric barrier discharge (DBD), it showed no obvious change [32]. More research is needed to clear these contradicted results regarding pulsed plasma jets. Pulse width is an important parameter pertinent to dynamics of plasma plume. Studies have shown that when pulse width is short (few hundred ns) increase pulse width results in longer plume and more energy deposited into plasmas. Consequently, higher discharge current [33, 34] could be detected. With long pulse, further increasing pulse width presented no appreciable effect on plasma plume [16]. When pulse-off time between two consecutive pulses is short enough, exotic plume structures were observed [35]. Effect of tube diameter on plume dynamics revealed that smaller diameter, higher propagation speed of ionization fronts and higher

plasma densities hence, longer plume [21]. Study of gas flow rate on plume dynamics indicates that plume length increased linearly with helium flow rate when the flow is in laminar region [36-39]. Varying pulse amplitude resulted in longer plume length at low voltage and saturated length at higher voltage [40-42].

Numerous research has been carried out to understand characteristics of plasma jets. However, from the perspective of reactive species, how would short pulse rise time, long pulse width and substrates affect the chemical pathways in plasma jets (covered in chapter 2)? Extra experiments needed to clarify the effect of pulse repetition rate, pulse width, amplitude, and gas flow rate and electrode configuration on plume characteristics (presented in chapter 3). The effect of seed electrons and memory effect on initiation and development of a plasma jet also remains unclear. For example, how would seed electrons affect breakdown probability of discharges (detailed investigation is illustrated in chapter 4)?

From those properties mentioned above on plasma jets, it is assumed that such plasma is a ‘guided streamer’ which has the same mechanism of a streamer discharge and guided by metastable, electrons and ions preserved from previous discharges [25, 34]. Streamer theory was developed by Loeb, Meek and Raether in 1940) [43-45]. It built upon several important experimental facts that are inconsistent with the Townsend theory:

1. The spark discharge at atmospheric pressure has been found to be independent of cathode material, i.e. Townsend secondary emission coefficient for cathode (γ) is invalid in this condition [46].

2. The time lag of forming a spark discharge from applying a voltage to occurrence of the actual discharge is several order of magnitude smaller (10^{-7} s) than predicted by Townsend theory (10^{-4} s) [47]. In Townsend theory, it states that positive ions have to move to the cathode and

bombard the cathode surface in order to generate the discharge in the case of 1 cm gap at small overvoltages [48].

A streamer is formed when the field of space charges increases to the level of the external field. It starts with an electron avalanche which is an inescapable process of any breakdown. The primary individual avalanche generates electron-ion pairs as it develops. Once electrons at the avalanche head reach the anode and sink into the electrode, streamer is initiated and developed with following the positively charged trail developed by previous avalanche (as seen from Fig. 1-3). Numerous of electrons generated by secondary avalanches are pulled into the primary trail by the field. These secondary avalanches are initiated by new electrons generated by photons emitted by excited atoms from primary and secondary avalanches.

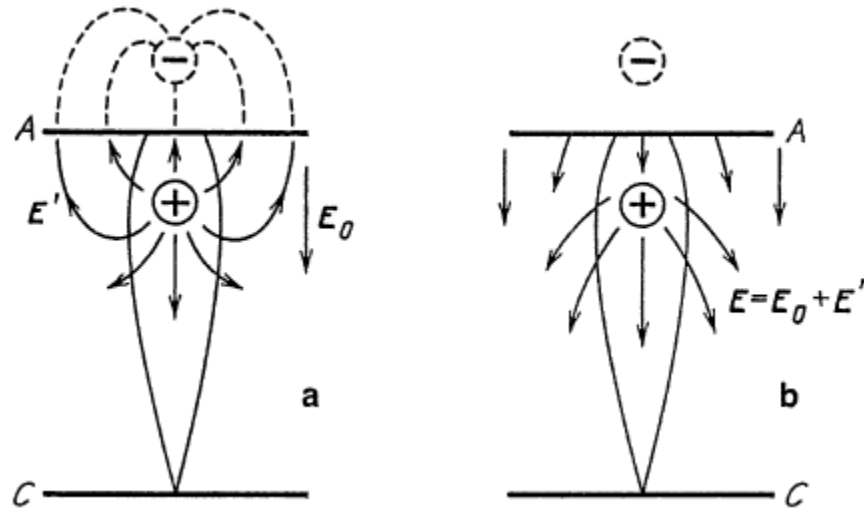


Fig. 1-3. (a) Electric field distribution caused by space charge (E') and external electric field (E_0) and (b) the resultant total electric field ($E = E_0 + E'$) [1].

In order to transform from an avalanche into a streamer, electron avalanches have to reach a sufficient high amplification (i.e. electric field produced by space charges has to reach the same level of external electric field). The streamer formation criterion [1]:

$$\alpha d \approx 18 - 20 \quad (1-1)$$

Where α and d are the first Townsend coefficient and distance of interelectrode, respectively. Once the primary avalanche reached such a high amplification, streamer is developed on the vicinity of the strongest electric field. In the case of small overvoltage and short interelectrode gap, the avalanche transforms into streamer when the avalanche reaches the anode. The streamer then initiated at the anode surface where the space charge is highest. Then it propagates towards the cathode. It is known as a cathode-directed streamer or a positive streamer (Fig. 1-4).

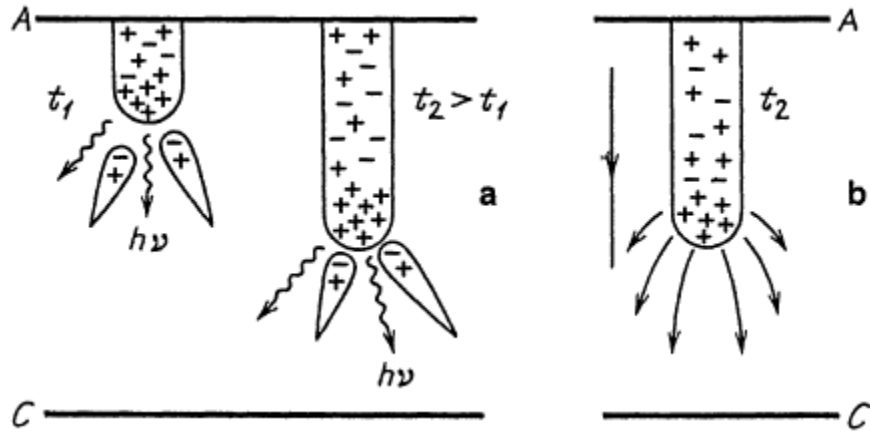


Fig. 1-4. (a) Cathode-directed streamer with two consecutive times ($t_2 > t_1$) and (b) the electric field distribution at the streamer head [1].

In general, streamer occurs at relative high pressure and long gap distance with sufficient overvoltage. Comparably, at low pressure and small gap distance (low pd), Townsend avalanche multiplications are dominant.

Townsend theory is developed by J. S. Townsend with assistance by his students. Consider discharge between two parallel electrodes, at x distance from cathode, there are n electrons, and one electron will generate α electrons as it travels 1 cm (this is the interpretation of α), so when it passes dx distance, n electrons could generate $n\alpha dx$ electrons which equals to the increment of electrons (dn) at dx . Thus,

$$dn = n\alpha dx \quad (1-2)$$

$$n = n_0 e^{\alpha x} \quad (1-3)$$

Where n_0 is the number of electrons at $x = 0$ (i.e. at the cathode). Equation (1-2) and (1-3) are derivative form and integrative form of the same equation. It indicates that the number of electrons increases exponentially with first Townsend ionization coefficient and its travelling distance. The carrier currents of an avalanche caused by moving electrons at location x can be estimated as [45]:

$$I_e \propto e n_0 v_d e^{\alpha x} \quad (1-4)$$

where v_d is the electron drift velocity. Equation (1-4) shows the electron current increases exponentially as electrons travel from cathode to anode due to the electron proliferation from electron ionized collisions.

Similarly, the ion current caused by positive ions moving towards cathode [45]. Since an electron could ionize to form an electron-ion pair due to ionization collision, the number of electrons are equal to the number of ions.

$$I_+ \propto e n_0 v_+ e^{\alpha x} \quad (1-5)$$

where v_+ is the drift velocity of ions. The current generated by positive ions is proportional to the drift velocity of ions and number of ions. Usually $v_+ \ll v_d$, at atmospheric air with electric field ~ 30 kV/cm, $v_+ = 10^5$ m/s while $v_d = 10^7$ m/s [1].

If we consider Townsend primary ionization coefficient (α), ionization coefficient by positive ions (β) and generalized secondary ionization coefficient (γ) [49].

$$i_e = \frac{i_0(\alpha-\beta)+(\alpha\gamma+\beta)i}{(1+\gamma)(\alpha-\beta)} e^{(\alpha-\beta)x} - \frac{\beta}{\alpha-\beta} i \quad (1-6)$$

where i_e is electron current, i is the total current (i.e. summation of electron and ions currents).

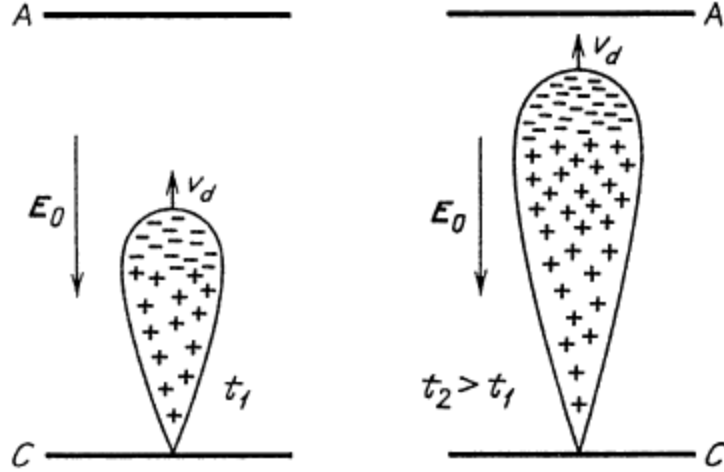


Fig. 1-5. An electron avalanche at two consecutive time, external electric field E_0 and electron drift direction with drift velocity V_d [1].

Ionization coefficient by positive ions is negligible and at the anode where $x = d$ the electron current equals total current so equation (1-6) can be simplified as [1]:

$$i = i_0 e^{\alpha d} \frac{1}{1 - \gamma(e^{\alpha d} - 1)} \quad (1-7)$$

i_0 and d are electron current and interelectrode gap distance, respectively. The discharge current derived from equation (1-7) indicates it determined by the number of electrons as well as the γ coefficient.

In electronegative gases (e.g. air), electrons can be attached by molecules form negative ions. The total current is then can be described as:

$$i = \frac{ev_d}{d} e^{(\alpha - a)v_e t} \quad (1-8)$$

where d is the interelectrode distance, a is the attachment coefficient. α is steeply depend on electric field as shown in Fig. 1-6. It is a function of pressure and electric field (equation (1-9) [1]. where A and B are constant depending on gas properties, p and E are pressure and electric field, respectively).

$$\alpha = Ape^{-\frac{Bp}{E}} \quad (1-9)$$

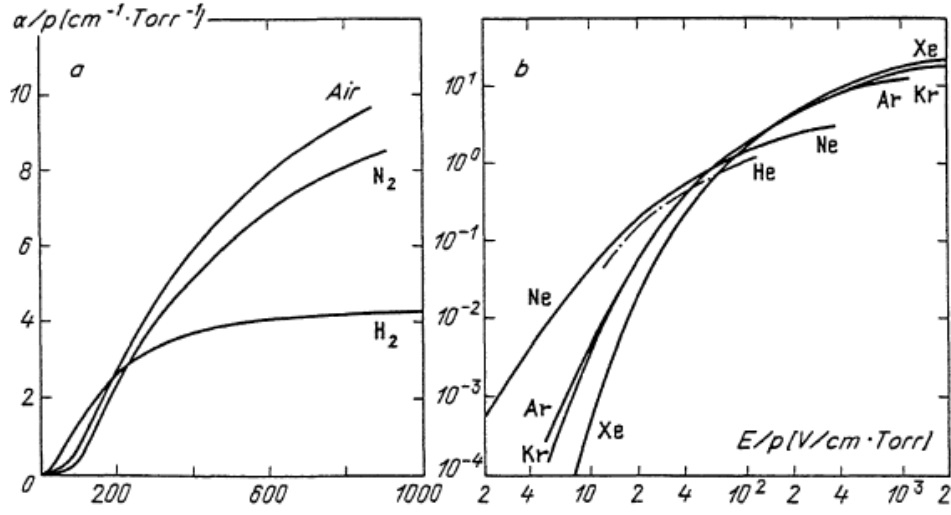


Fig. 1-6. Ionization coefficient for a wide range of gases (a) molecules and (b) inertial gases [1].

Breakdown ignition potential (V_t) under uniform electric field can be calculated with combination of equation (1-7) and (1-9) [1]:

$$V_t = \frac{Bpd}{C + \ln(pd)} \quad (1-10)$$

$$C = \ln\left(\frac{A}{\ln\left(\frac{1}{\gamma}\right) + 1}\right)$$

The experimental curves V_t (namely Paschen curves) are shown in Fig. 1-7. As one can see from the figure, it exists the minimal breakdown voltage at certain pd .

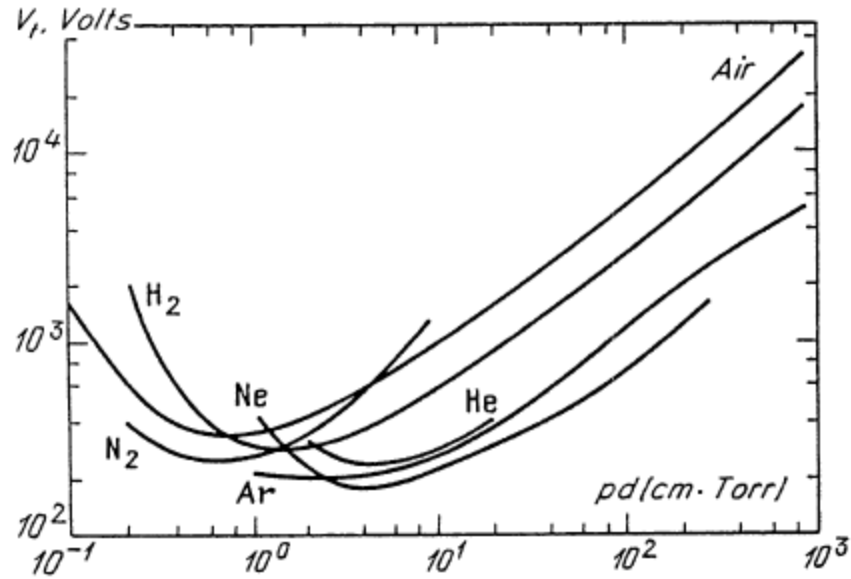


Fig. 1-7. Breakdown potentials on various gases over a wide range of pd values [1].

Breakdown in Townsend theory is well studied, however, for streamer discharges at atmospheric pressure, especially when a single-electrode and a highly non-uniform electric field are involved, the breakdown could be quite different compared with convention uniform field in Townsend or streamer theory. Chapter 4 concentrates on breakdown in a highly non-uniform electric field produced by a single-needle electrode.

Breakdown is the process which can transform a non-conducting medium into a conductive one by applying a sufficient strong field [1]. From electrical perspective of breakdown, a sudden voltage drop between two electrodes may be observed with a dramatic increase of current. Typical DC voltage-current characteristics under constant electric field between two parallel metal plates is shown in Fig.1-8 [50].

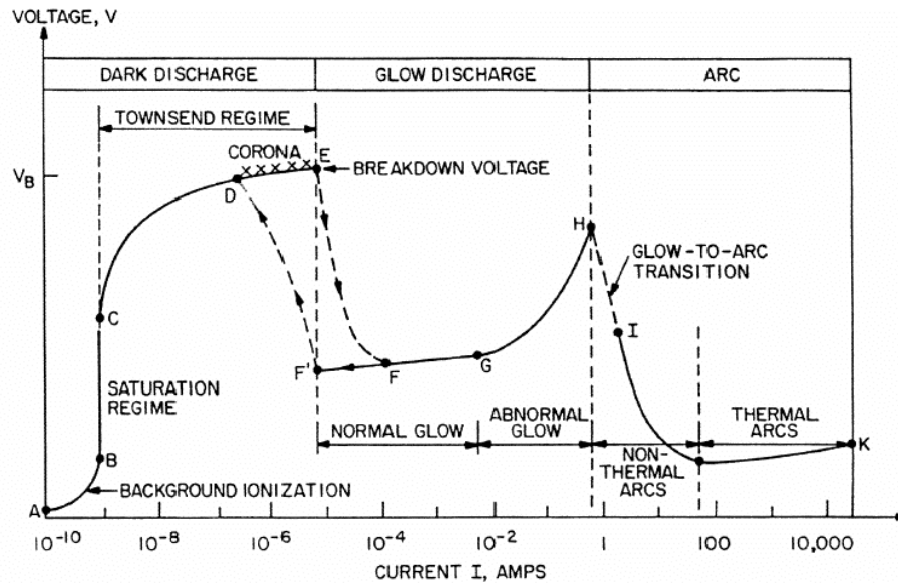


Fig. 1-8. Voltage-current characteristics of a typical discharge between two parallel plates [50].

As one can see in Fig.1-8 from range A to B, when applied voltage is not high, the positive and negative charges caused by cosmic ray will be pulled by the electric field towards their opposite-sign electrodes, producing a current as low as $10^{-15} \sim 10^{-9}$, which can only be detected by a sensitive instrument. With increasing the applied voltage (around several tens of volts), all charges generated by the cosmic ray are pulled away to electrodes hence the current ceased to grow (Fig.1-8 point B to C), limited by the rate of ionization. If the voltage is raised further, the current suddenly increases abruptly with appreciable light emissions. This is the manifest of breakdown (Fig.1-8 Point C to E) with the voltage exceeding a certain voltage. The Townsend regime is usually called 'dark discharge' because ionization is so small that the gas emits no appreciable light. At such condition, if the pressure is relatively low (e.g. at 1 Torr) and we increase the discharge current by decreasing the resistance of the circuit, the voltage between the two electrodes will further decrease into which called 'glow discharge'. If the discharge circuit allows more current flow, the voltage will further decrease as the current increases, which leads to arc discharge.

However, at high pressure (e.g. at atmospheric pressure), if a sufficient high voltage is applied with current not suppressed by external resistor, a spark discharge is developed with a plasma channel rapidly bridge two electrodes. Finally, if a strongly non-uniform electric field is formed between two electrodes by high voltage, a corona could be formed with a radiant in the region of high electric field while totally dark in the low field region.

Breakdown at low pressure is obvious which is usually characterized by a sharp decrease of voltage with exponential growth of current and accompanied with appreciable light emission. At high pressure, however, it is slightly complicated. An air corona discharge has no obvious voltage drop but it's a breakdown with current rising substantially and associated with a visible light.

A discharge transitioning from non-self-sustaining to self-sustaining can be thought of as a breakdown. Fig. 1-8 from point A to C is 'non-self-sustaining' discharge since the current mainly determined by charges generated due to an outside source (such as cosmic ray). The transition from 'non-self-sustaining' discharge to 'self-sustaining' discharge is determined by equation (1-7):

When $\gamma(e^{\alpha d} - 1) = 1$, the transition occurs in which the discharge ensures reproduction of electrons removed by the field without the help of an external source. From 'non-self-sustaining' discharge to 'self-sustaining' is the process of breakdown. The inception (onset) of breakdown is the early stage of such transition.

In this research, a single-needle electrode is employed to study the inception and breakdown in air without gas flow (i.e. corona discharge) and with helium flow (plasma jets) driven by pulsed power supply via high speed imaging. Several interesting characteristics of the plasma jets (i.e. charge polarity and repeatability of ionization fronts and secondary discharge at falling edge of a voltage pulse) are investigated using high speed imaging as well as electrical measurements.

Operation parameters (i.e. voltage amplitude, repetition rate, pulse width and gas flow rate) of plasma jets are examined to understand their effect on development of ionization fronts. Importantly, chemical reactions inside plasma jets are studied via optical emission spectroscopy and laser-induced fluorescence.

The following chapters are organized as the following:

Chapter 2 illustrates the chemical reactions in plasma jets, mainly during the development phase. Spatiotemporal optical emission spectroscopy is employed to understand how reactive species in the plume evolves with time and space. Long (i.e. 164 ns pulse width) and short (i.e. 5 ns pulse width) pulses are used to drive the single-needle electrode which produces two different emissions behaviors. The study centers on the effect of short pulse on generation of excited species. Further study of a single-electrode plasma jet interacting with a water electrode are carried out. By introducing a water electrode, the evolution of excited species is examined compared without water electrode. Furthermore, excited OH(A-X) radicals are studied when a pulsed plasma jet interacting with the water electrode. It focuses on investigation of pulse width on effect of OH(A-X) temporal distribution.

Chapter 2 starts with a general observation of a single-needle electrode discharge with and without He flow. The interaction between corona discharges and plasma jets leads to study of corona discharge in air which further extended to plasma jet. Both discharges are focused on pulse parameters that affect their breakdown probabilities. Such study leads to investigation of inception of corona discharges and plasma jets which are the early phase of breakdown. Chapter 2 mainly concentrates on breakdown of corona discharges and plasma jets.

In chapter 3, dynamics of a plasma jet (i.e. ionization fronts, repeatability and secondary discharge) driven by pulsed voltages are carefully examined. Subsequently, varying of operation

parameters (e.g. pulse parameters, gas flow etc.) on development of a plasma jet is studied. Chapter 3 focuses on development of a plasma jet, i.e. the discharge process after breakdown.

Chapter 4 starts with a general observation of a single-needle electrode discharge with and without He flow. The interaction between corona discharges and plasma jets leads to study of corona discharge in air which further extended to plasma jet. Both discharges are focused on pulse parameters that affect their breakdown probabilities. Such study leads to investigation of inception of corona discharges and plasma jets which are the early phase of breakdown. Chapter 4 mainly concentrates on breakdown of corona discharges and plasma jets.

Conclusions are drawn in chapter 5 with illustration of main findings in this research. In the meantime, topics on future research are discussed.

1-4. EXPERIMENTAL METHODS

Terms and notations used in this manuscript are illustrated here. APPJ and APNPJ are short for Atmospheric Pressure Plasma jet and Atmospheric Pressure Nanosecond Plasma Jet. Throughout this research, pulsed power supply (mostly nanosecond pulses) is employed in the range of nanosecond to millisecond. Regardless of the pulse width, such pulsed plasma jet is called ‘APNPJ’ for simplicity. Electrode is a stainless steel single hollow needle electrode with various inner and outer diameters with or without substrates. ‘Single-needle electrode’ will be used to specifically infer such electrode unless indicated otherwise. Ultra-high purity helium is the only gas used for flowing through the hollow of the single-needle electrode and will be abbreviated as He. Diagnostic methods such as electrical measurements, high speed imaging, optical emission spectroscopy and laser-induced fluorescence are employed. Voltage-current waveforms specifically present the voltage and current waveforms measured by voltage probes and current

monitors. OES and SPOES are short for optical emission spectroscopy and spatiotemporal optical emission spectroscopy, respectively. Laser-induced fluorescence is abbreviated as LIF.

The reason for selecting such jet device and instruments (e.g. single-needle electrode, pulsed power supply etc.) is explained here. Even though these choices are limited by the sources of the lab I worked with, it is designed with cautions. Compared with plasmas generated with kilohertz AC and RF sources, Pulsed plasmas attracted a lot of attention due to its relative higher efficiency [51, 52] in producing some reactive species as well as their flexible tuning parameters (i.e. pulse amplitude, repetition rate, rise time, and pulse width). As one would notice, observation of inception of the corona discharges and APNPIs (chapter 4-5) are attributed to the flexible tuning parameters of pulsed voltages. Jet device is an important aspect as mentioned before in chapter 1-2. There are many advantages regarding the single-needle electrode, the most important one, however, is that discharges generated by such electrode are always initiated at its needle tip where the strongest electric field resides. Such advantage strongly correlates with our research (i.e. study of the breakdown and development of plasma jets). It is important to notice that the secondary discharge of a voltage pulse is relatively short in length compared with the primary one hence for most DBD-jets that have their electrodes covered by dielectric would hide such discharge from observations. This is the reason that secondary discharge for APNPJ is investigated much later compared with the study of primary discharge [33].

Breakdown process can be observed via three main methods [45]: Cloud chamber which makes the condensation of nuclei of ions observable, could be represented by the profile of electron avalanche. The electrical method could monitor the electrical voltage and current generated by the drifting electrons and ions of avalanche. Optical method such as high speed imaging is also

applicable because the drifting electrons not only ionize the gas but also excite the gas which gave a resemble image produce by the cloud chamber method.

Optical diagnostics usually involves imaging and spectroscopy. The ignition and development of the discharge processes are on the order of $10^4 \sim 10^6$ m/s [13, 14, 53, 54] in atmospheric pressure plasmas, thus high speed imaging (nanosecond or sub-nanosecond) is required to have sufficient temporal resolution. High speed imaging can be achieved by ICCD (intensified charge-coupled device) camera and provides visualized images on evolution of the discharge processes. Experimental setups for electrical measurements and high speed imaging is shown in Fig. 2-1. Measurements details are varied depending on each experimental need.

Two main types of spectroscopy (absorption and emission spectroscopy) are mostly used in many applications. We focus on only emission spectroscopy in our studies. Emission spectroscopy is a technique that uses some means to excite the targeted sample. Lights then emit from atoms or molecules when they relax from the electronically excited states in which the emission spectrum can be associated with a unique atom or molecule.

The techniques pertinent to emission spectroscopic are mainly optical emission spectroscopy (OES) and laser-based techniques such as laser-induced fluorescence (LIF). Various perspectives include but not limited to spatiotemporal evolution of excited species, electron density by Stark broadening and line-ratio method, and electric field by Stark polarization spectroscopy were investigated via emission spectroscopy. Excited species including excited O, OH, N₂, N₂⁺, and He were identified in a pulsed helium plasma jet via optical emission spectroscopy [55]. The propagation dynamics of these identified species indicate that the N₂ emission in the plume travels fast along the entire plume; the N₂⁺ presents a bright streamer head with weak tail and travel shorter

than N₂. The O and OH, however, mostly localized near the high positive voltage electrode without any propagation behavior. Although helium is the carrier gas, its propagation distance is short with a low speed [56, 57]. Dependence of pulsed voltages on the optical emission intensity of the plasma jet were studied. Spatiotemporally-resolved optical emission spectroscopy revealed that the species including excited O, N₂, N₂⁺, and He propagated faster with increasing the voltage amplitude [58]. Not only the dynamic properties can be observed by OES, but also parameters like gas temperature, electron density, and electric field can be examined via OES related technique. Electric fields were estimated from direct electron impact excitation from N₂(C) and N₂(B) bands using optical emission spectroscopy and the maximum local electric field is estimated to be 95 kV/cm at the 1.2 cm from jet nozzle [59]. The electric field distribution was measured in the cathode region of a helium dielectric barrier discharge using emission spectroscopy coupled with the polarization-dependent Stark splitting and shifting of He line at 492.19 nm [60]. Measurement of OH radicals (ground and excited states) in atmospheric pressure plasma jets (APPJs) are important due to the increasing interests on APPJs assisted plasma medicine [4, 61, 62]. OH radical is the most reactive oxidizing species and play an important role in biomedical applications. Many investigations on OH measurement by laser-induced fluorescence have been reported. It is found that the maximum OH concentration was measured to be $\sim 5 \times 10^{14} \text{ cm}^{-3}$ at 2 mm away from the nozzle in an argon RF plasma jet [63]. The OH radicals are measured in a nanosecond pulsed filamentary discharge with pin-pin electrodes in flowing with He-H₂O mixture [64]. It is found that the maximum OH density is at the center of the filament discharge when low voltage applied (1.5 kV), while in high voltage (5 kV) the highest OH density is observed on the edge of the discharge. Study of OH radicals in both gas and liquid phases using LIF and a chemical probe method in a pulsed surface streamer discharge was also reported. The gas phase OH radicals have

been examined in respect to the temporal distributions. After the OH radicals dissolved from the gas phase into the liquid, A chemical probe that introduced terephthalic acid to trap OH radicals and the absolute concentration of OH radicals was measured to be of the order of $10^{-9} \text{ M}^{-1}\text{s}^{-1}$ from the fluorescence of 2-hydroxyterephthalic acid in presented conditions [65].

Spectroscopy is a tool used for studying the structures of atoms and molecules by observing a set of wavelengths missing from the incident light source (absorption) or emitted from substances (emission). The missing or emitted spectrum from the atoms or molecules are their fingerprint since they depend on the energies of the excited and ground states of electrons in atoms or molecules. The development of spectroscopic techniques enriches the detectable parameters including gas temperature, electron density, electric field and density of transient species when flames or plasmas are studied. Fig. 2-1 presents schematic of optical emission spectroscopy.

The applied voltage and total current were measured at the load of the transmission line using a high voltage probe (Tektronix 6015A) and a current monitor (Pearson 6585), respectively. For spatiotemporally resolved imaging, an ICCD (Princeton Instrument PI-MAX 4) that was coupled with a UV–visible, fused silica bi-convex lens (focal length = 75 mm) was synchronized with the pulsed voltage to collect the plasma emission. At a given delay time, the plasma image was obtained from integration of many exposures (depending on the signal) with each exposure time of 5 ns and an ICCD gain of 100.

For optical emission spectroscopy, a Czerny-Turner spectragraph (Acton SP-2758) coupled with an ICCD camera is employed to detect emission spectra. The grating is 1800 g/mm which is tunable and optimized on visible wavelength. To focus the plasma emissions, two UV enhanced metallic aluminum mirrors (a plano and a concave mirror) are used to direct light into the spectragraph. The concave mirror has a focal length of 75 mm. Magnification is set to 1:1 ratio

between the plasma jet and its image on ICCD camera. A spectral resolution of 0.02 nm is achieved when the slit width is set to 20 μm . For all the integrated emission spectra from plasma jets, emissions ranging from 250 nm to 850 nm are recorded. To avoid the second order dispersions of emissions below 450 nm, a longpass filter (Thorlabs FEL0450) is used to filter out higher order interferences. For spatiotemporally resolved emission spectroscopy, the ICCD camera is synchronized with the voltage pulses to control triggering time.

CHAPTER 2

DIAGNOSTICS OF REACTIVE SPECIES IN ATMOSPHERIC PRESSURE NANOSECOND PLASMA JETS

2-1. ABSTRACT

In the last decade, non-thermal atmospheric pressure plasma jets draw a lot of attentions due to its wide applications (e.g. surface modification, plasma medicine). The plasma jets have shown promising potential in various applications of plasma medicine (e.g. wound healing, surface decontamination and cancer cell treatment [66-68]). Reactive oxygen and nitrogen species are of peculiar interest in fundamental research of plasma jets due to their induced biological effect in treatments [6, 69, 70]. This chapter studies the effect of extreme short pulse (5-ns pulse width), water electrode and pulse width on production of excited reactive species (e.g. N_2 , N_2^+ , He, O, and OH) in APNPJs driven by 6 – 8 kV, 5 – 5000 ns pulses at 0.5 – 1 kHz with helium flow. Optical emission spectroscopy and electrical measurements are employed to study the relationship between energy deposition and production of reactive species.

Emission spectrum of N_2 (C-B) second positive system and OH(A-X) revealed the average gas temperature of APNPJs remained near room temperature (~ 300 K). Further study indicates that comparable or more reactive species (including N_2 , N_2^+ , He, O, and OH) are detected during the first 100 ns of the voltage pulse when compare the short pulse (5- ns) with the long pulse (164-ns). When the APNPJ impinged onto the water surface, excited species including N_2 , N_2^+ , OH, and O

present stronger emissions, meanwhile, enhanced ionization near the single-electrode nozzle and earlier streamer formation are observed compared with APNPJ impinged into a container without water. More importantly, study of excited OH(A-X) reveals that the maximal energy efficiency of OH(A-X) emission is obtained with pulse widths of 600 – 800 ns when pulse widths ranged from 200 ns to 5000 ns. Temporally-resolved emission spectroscopy shows that more than 40% of OH(A-X) emission is produced during the first 200 ns of the voltage pulse regardless of the pulse width.

2-2. STUDY OF SPATIOTEMPORALLY-RESOLVED OPTICAL EMISSIONS BETWEEN A LONG (164 NS) AND SHORT (5 NS) NANOSECOND PLASMA JETS

Growing interests in plasma jets due to its potential biomedical applications attract a lot of attention regarding study of reactive species in plasma plume. However, effect of pulse rise time on reactive species remained unclear. Recent studies shown that short pulse rise time could produce more excited species due to reinforced ionization. [14]. It is found that a significant increase in argon emissions was detected with decreasing of pulse rise time from 4 μ s to 140 ns [15]. Generally, results suggested that shorter pulse rise time could result in longer and faster plasma plumes when powered with pulse rise time of 50 ns or longer [16]. However, it is still unclear for short pulse rise time (≤ 50 ns) and pulse duration (≤ 164 ns) on effect of APNPJs. In this study, a single-needle electrode driven by nanosecond high voltage pulses: 5 ns or 164 ns pulses at 8 kV is examined with flowing of He gas. Driven by two different pulsed power supplies, allow the plasma to be investigated in terms of the high voltage pulse characteristics (i.e., voltage pulse duration and rise time). Subsequently, effects of such pulse parameters on composition and distribution of reactive species are evaluated.

Fig. 2-1 showed the schematic for optical emission spectroscopy. A spectragraph (Acton SP-2758) with grating at 1800G/mm coupled with an ICCD camera was employed to detect emission spectra. Two UV enhanced mirrors (i.e. one plano and one concave mirrors) are used to focus the plume onto the slit of spectragraph with magnification ratio of 1:1. The slit width is 20 μm with a spectral resolution about 0.02 nm. Wavelength range from 200 to 850 nm were recorded. To avoid second order dispersions from emissions below 450 nm, a long pass filter is applied to the slit to eliminate this interference. Spectral emissions are obtained with ICCD exposure of 100 ns with combination of 4000 frames (Fig. 2-2).

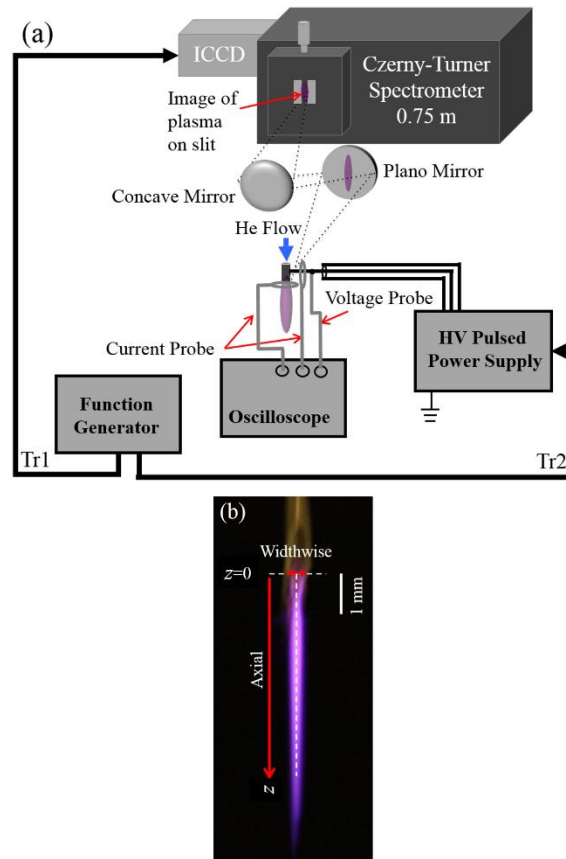


Fig. 2-1. (a) Schematic of optical emission spectroscopy for nanosecond pulsed plasma jets and (b) a plasma plume with short pulse (5 ns pulse width) [71].

Voltage and current waveforms when powered by 5 ns and 164 ns pulses are shown in Fig. 2-2. The primary maximum voltage pulse for 5 ns pulses is about 8 kV with a pulse rise time of 5.1 ns. For the longer pulse (164 ns pulses), it has a pulse rise time of 50 ns with amplitude of 8 kV. Discharge currents showed two peaks for both pulses with each current consisting of replacement and conduction components.

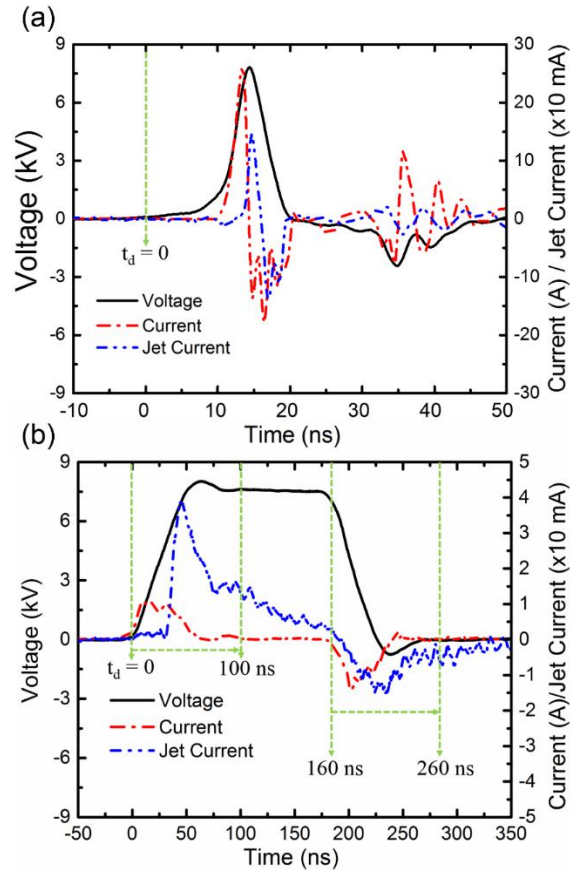


Fig. 2-2. Voltage and current waveforms of pulsed plasma jet at 8 kV with pulse width of (a) 5 ns and (b) 164 ns at 500 Hz [71].

Fig. 2-3 presents the integrated emission intensity of reactive species. Emissions along the axial direction (shown in Fig. 2-1 (b)) are captured using optical emission spectroscopy and followed by integration along the axial direction to generate total emission intensities of all

identified species. As one can see, a number of excited species are identified including OH ($A^2\Sigma_+$), N₂ ($C^3\Pi_u$), N₂⁺ ($B^2\Sigma_u^+$), He (3^3D), and O ($3p^5P$). Dominant emissions are N₂ $C^3\Pi_u$ - $B^3\Pi_g$ (0-0), N₂⁺ $B^2\Sigma_u^+$ - $X^2\Sigma_g^+$ (0-0) and He 3^3D - 2^3P . Table I lists the integrated emission intensity of identified species. It is found that for the shorter pulse generated less excited N₂, He, OH, and O. However, emission of N₂⁺ increased by a factor of 1.3 with shorter pulse (i.e. 5 ns).

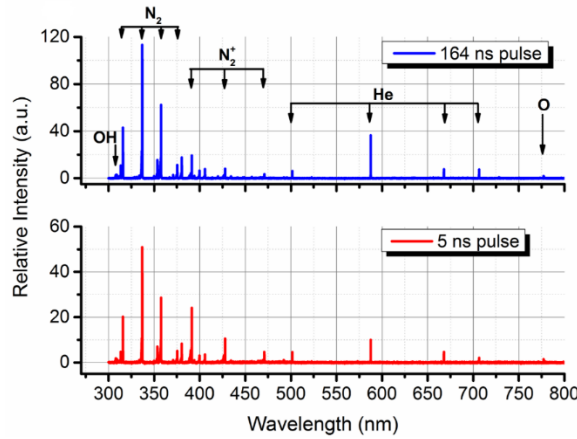


Fig. 2-3. Total emission spectra of APNPJs integrated along the axial direction [71].

TABLE 2-1

Maximum intensity of identified species from Fig. 2-3 for both 5 ns and 164 ns pulses [71]

Transition Wavelength (nm)	Maximum Emission Intensity (a. u.)				
	OH (309 nm)	N ₂ (337 nm)	N ₂ ⁺ (391 nm)	He (587 nm)	O (777 nm)
164 ns	2.90	113	19	36	1.86
5 ns	1.86	51	25	10	1.45

Spatial distribution of normalized emissions from reactive species are shown in Fig. 2-4 (a). It is found that the strongest emissions of all transitions re-observed within 4 mm from the nozzle surface for both plasma jets. Even more, it is within the first 2 mm for the 5 ns plasma jet. Slightly earlier rising of emissions from N₂, N₂⁺, and OH are detected for the 5 ns pulsed plasma compared with the long pulse. OH emissions for both plasma jets is comparable. It is found that for the 164

ns pulsed plasma, the N_2 emission extended further distance, up to 9 mm, corresponding to the plasma plume length.

Time-dependent emission intensities for both plasma jets are examined. Fig. 2-4 (b) showed the temporally-resolved optical emission spectra along the axial direction. Emissions were taken at different delay times (t_d) with an integration time of 100 ns (shown in Fig. 2-2 dot green lines). It is found that emissions from O and N_2^+ were stronger for the 5 ns pulsed plasma jet compared with the 164 ns one during the first 100 ns. For N_2 emissions, the 5 ns pulsed plasma had slightly stronger or comparable emission for a distance of 4 mm from the nozzle and decreased rapidly for longer distance. Moreover, peak emissions of all excited species are higher for 5 ns plasma jet except He. At $t_d = 160$ ns, the 164 ns pulse started to fall with a secondary emission detected again near the needle nozzle. The emission of N_2^+ has a restrike during the pulse falling phase while other emissions including N_2 , He, O, and OH increased by a factor of 3 or higher. After $t_d = 160$ ns, emissions of all excited species gradually decayed until $t_d = 400$ ns.

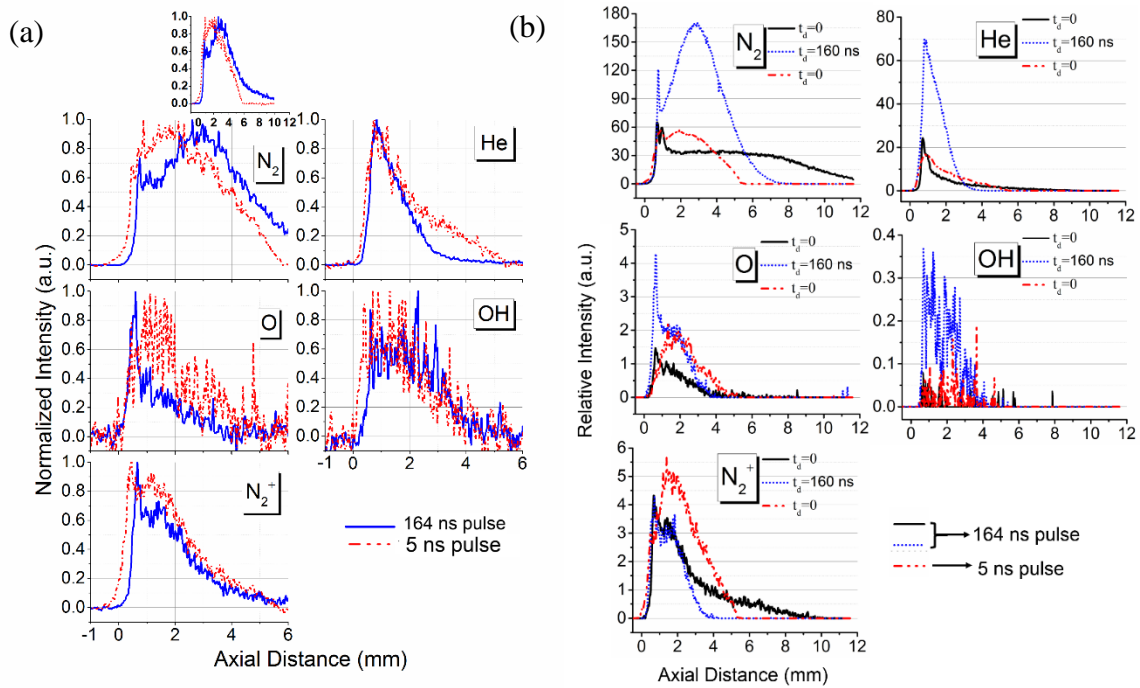


Fig. 2-4. (a) Normalized emissions of excited species N_2 , He, O, OH, and N_2^+ for the 5 ns pulse (red dot) and 164 ns pulse (blue solid) along the axial direction. Jet nozzle is at $z = 0$. (b) Spatiotemporal distributions of identified species at two different delay time indicated in Fig. 2-2 for 5 ns and 164 ns pulsed plasma jets [71].

As introduced in chapter 1 section 2, the rotational and vibrational temperatures along the axis of the plasma jets are analyzed with N_2 second positive system with a simulation in Specair using a least-square fitting procedure (Fig. 2-5). The N_2 (0-0) emission band revealed a rotational temperature around $300 \text{ K} \pm 50 \text{ K}$ for both 5 ns and 164 ns plasma jets. Fitting several of the axially measured rovibronic transitions of N_2 (C-B) indicated that the vibrational temperature was approximately $3200 \text{ K} \pm 300 \text{ K}$ for the 5 ns pulse plasma and approximately $3100 \text{ K} \pm 250 \text{ K}$ for the 164 ns pulse plasma. Temperature measurements indicate that these pulsed plasma jets are under highly non-equilibrium conditions, hence it may favor the plasma chemistry.

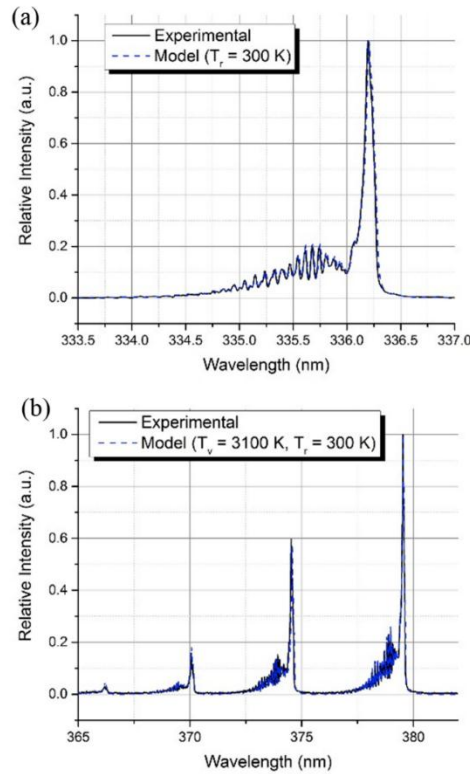


Fig. 2-5. Experimental and simulation emission spectra of N₂ second positive system N₂ (C³Π_u – B³Π_g) (a) at (0-0) band for rotational temperature and (b) at Δv = 2 transitions for vibrational temperature [71].

In summary, effects of pulse rise time and pulse width are investigated regarding optical emissions on a 5 ns and a 164 ns pulsed plasma jets. A He plasma jet is produced when powered by 5 ns or 164 ns 8 kV pulses at 500 Hz on a single-needle electrode. It is found that for 5 ns plasma, more excited N₂⁺ (by a factor of 1.3) is generated compared with 164 ns plasma. However, less excited N₂, He, O and OH productions in shorter pulse. Maximal emissions of all the excited species localized near the needle nozzle which imply that direct electron impact reactions played an import role in generating these reactive species. For the first 100 ns under spatially-resolve emissions, it is found that comparable or higher emissions are observed for the 5 ns plasma. However, longer pulse (164 ns) could generate more total excited species indicating that pulse width is critical for driven plasma and producing higher total amount of reactive species. Measurements of rotational and vibrational emissions of N₂ (C-B) showed that both plasma jets had comparable rotational and vibrational temperatures of 300 K and 3000 K, respectively.

2-3. COMPARISON STUDY OF SPATIOTEMPORALLY RESOLVED EMISSIONS IN ATMOSPHERIC PRESSURE NANOSECOND PLASMA JETS WITH AND WITHOUT WATER

A plasma jet could impinge onto a substrate surface when applied to biomedical applications. The substrate, on one hand, served as a ground; on the other hand, it usually covered by a thin layer of water or in liquid solution. Subsequently, study of plasma jet interacting with water is of great importance on application-wise. Chemical pathways play a key role for plasma induced

biology effect [4, 6, 72]. In this study, a single-needle electrode driven by pulsed power is employed to interacting with water. The water is contained in a $75 \times 25 \times 25 \text{ mm}^3$ container with bottom is made of copper plate and walls of fused silica glass. Distance from needle nozzle to water surface is kept fixed at 10 mm (as shown in Fig. 2-6). The stainless steel needle has an outer nozzle diameter of 0.254 mm with helium flow of 200 SCCM through the hollow needle. Schematic of electrical measurements as well as optical emission spectroscopy can be found on chapter 1 section 4. This study presents studies of electrical and optical properties of APPJs with and without water. The water container (grounded) is removed in the without water case.

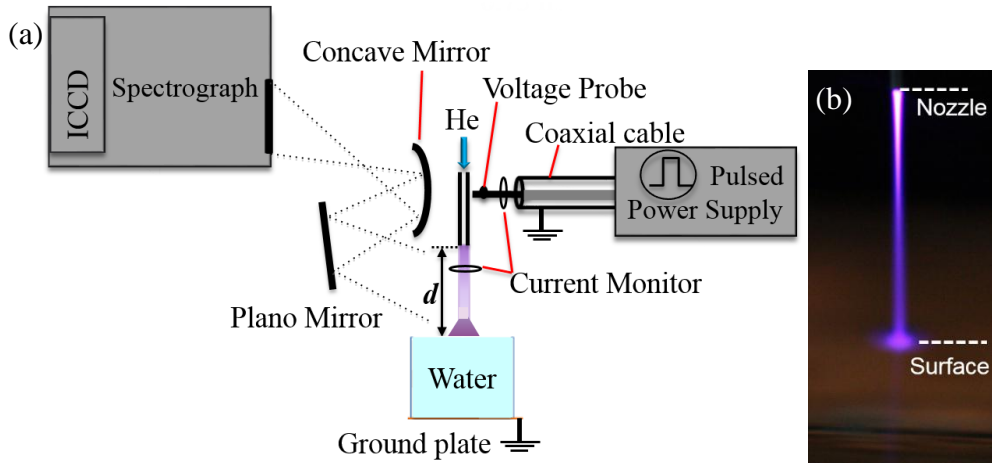


Fig. 2-6. (a) Experimental setup of optical emission spectroscopy for APNPJ and (b) a helium jet impinging onto the water surface, the gap from nozzle to water surface is 10 mm [73].

Fig. 2-7 presents voltage and current waveforms of plasma jets with and without water. The voltage pulse has a full-width half-maximum (FWHM) of 164 ns with a rise time of 49 ns at amplitude of 7 kV at 1 kHz. For both cases, the applied voltage stays the same while their jet currents which obtained from the current monitor are vastly different. Energy per pulse was calculated by integrating the product of the voltage and discharge current pulses over a sufficient period of time, e.g., 350 ns. They are 115 and 50 μJ for the plasma with and without the water

electrode, respectively. The peak jet currents are 45 mA and 15 mA for with and without water, respectively. The jet current in the with water case had an earlier onset. Integration of the positive pulse of the jet current over time gives the total charges per pulse deposited from power to plasma. It is 5 times more in the presence of water electrode: 2.39 nC vs 0.46 nC for the plasmas with and without water. Additionally, a negative jet current pulse with a lower magnitude, ~ 7 mA, was observed in absence of water during the falling phase of the voltage pulse.

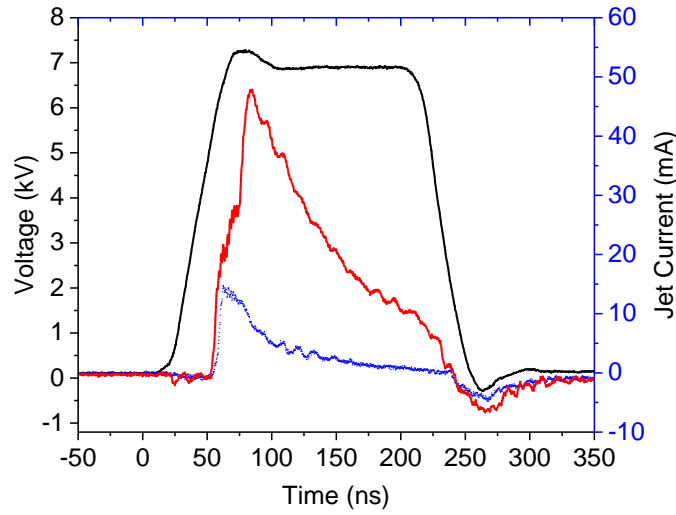


Fig. 2-7. Voltage (black solid line) and jet currents of APNPs interacting with (red solid line) and without water (blue dot line).

Integrated optical emissions from identified species are shown in Fig. 2-8. It is found that with presence of water, emissions from excited OH, N_2 , N_2^+ , He, and O have higher intensities compared with corresponding species without water. Table 2.2 shows their maximum intensities for both cases. Excited OH, N_2 , and O increase by factors of 2.7, 1.2, and 1.6, respectively in the case of with water. Comparable intensities of N_2^+ , H_α , and He for both cases are found.

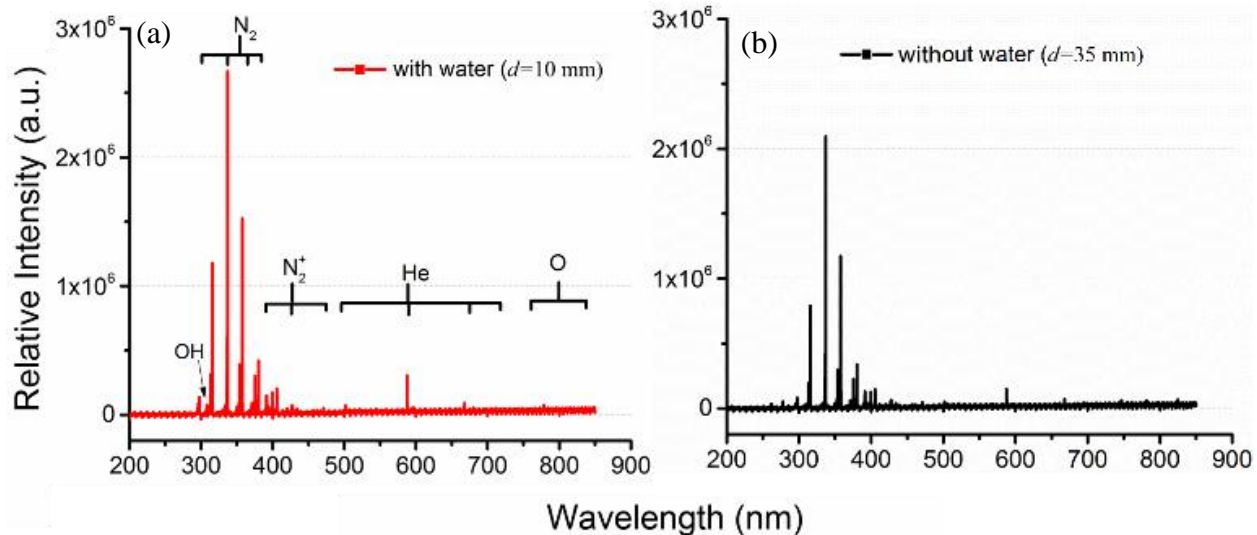


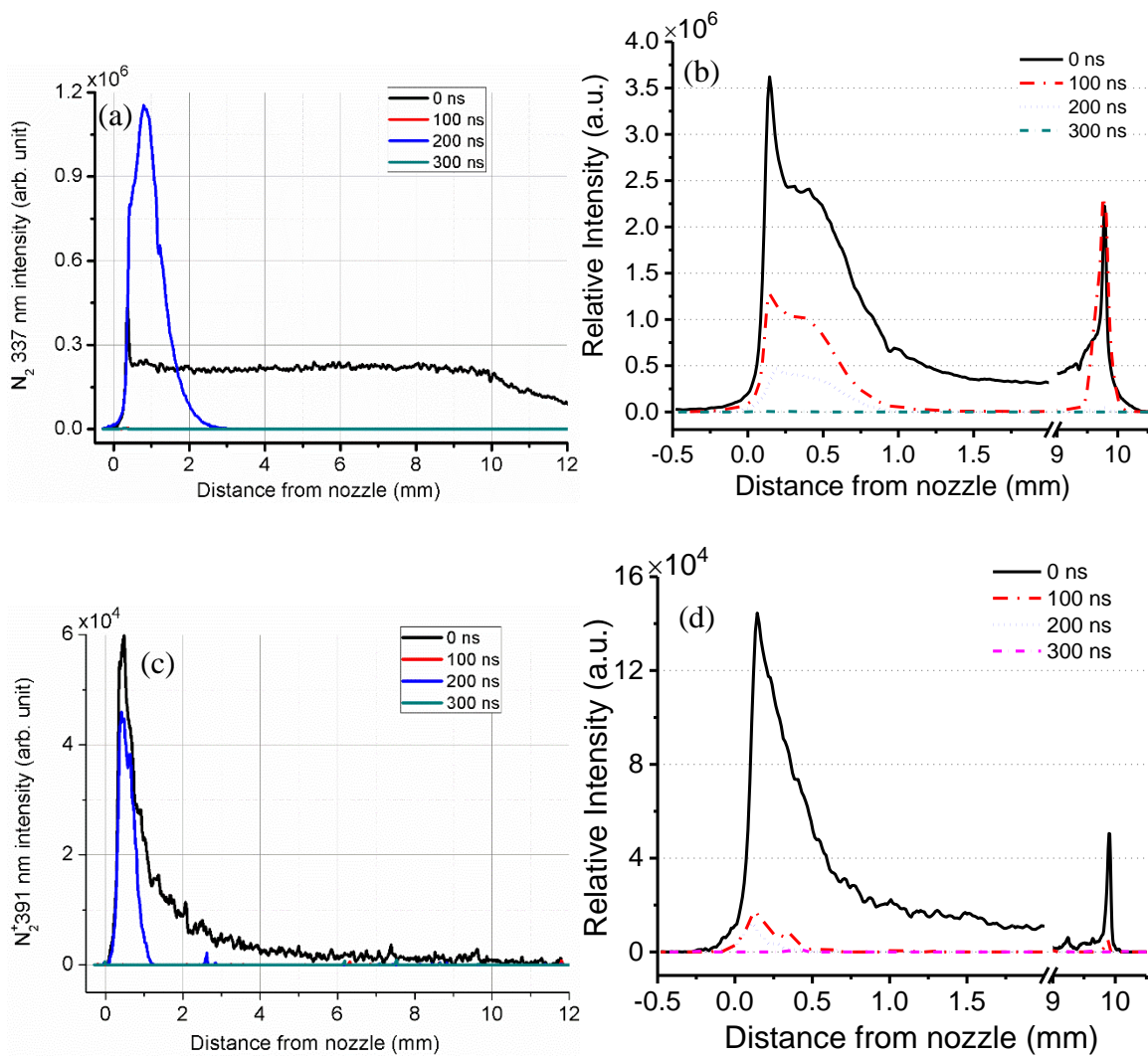
Fig. 2-8. Integrated optical emission spectroscopy along the axial direction for APNPIs (a) with and (b) without water [73].

Table 2.2 maximum emission intensities of reactive species from Fig. 2-8 [73].

Transition Wavelength (nm)	Emission Intensity (a.u.)					
	OH($A^2\Sigma-X^2\Pi$)	N ₂ ($C^3\Pi_u-B^3\Pi_g$)	N ₂ ⁺ ($B^2\Sigma_u-X^2\Sigma_g$)	H _u ($^3D-^2P$)	He($^3S_1-^3P$)	O($^5P_3-^5S_2$)
	309.0	337.1	391.4	656.3	706.5	777.3
Plasma without water	1.67	100.01	8.13	2.02	2.33	1.41
Plasma with water	6.12	121.12	8.54	2.03	2.16	2.28

Spatiotemporally distribution of reactive species OH, N₂, N₂⁺, He, and O are investigated (as shown in Fig. 2-9). If one examines the emissions without water, it is found that strong emissions are at time 0 and 100 ns which corresponds to the rising and falling phases of a voltage pulse. On the other hand, emissions of all species are localized within 2 mm from needle nozzle except for N₂ (337 nm) at time 0. It is revealed that direct electron impact reactions may be attributed to generation of these species since strong electric field presents near the needle electric field. Considering emissions from presence of water electrode, it is found that temporal distribution of emissions not only during the rising and falling phases of a voltage pulse but also including the

pulse plateau and after glow. Additionally, spatial distribution shows that emission intensities not only localized near the needle electrode but also near the water surface.



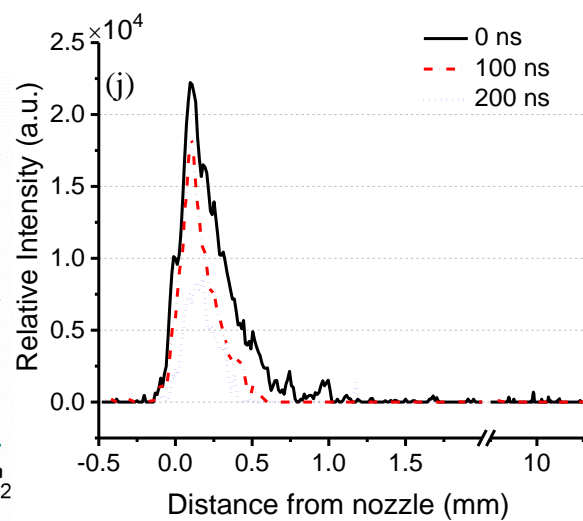
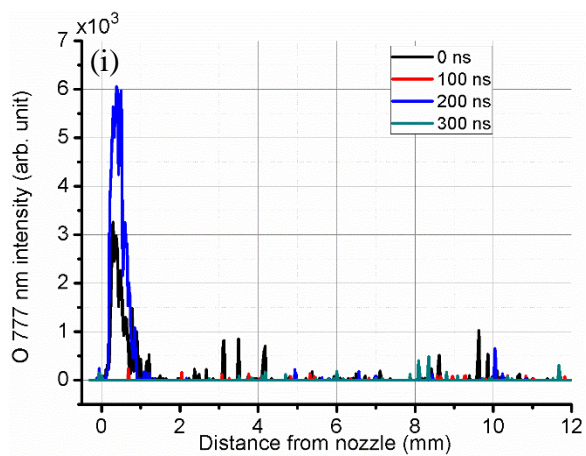
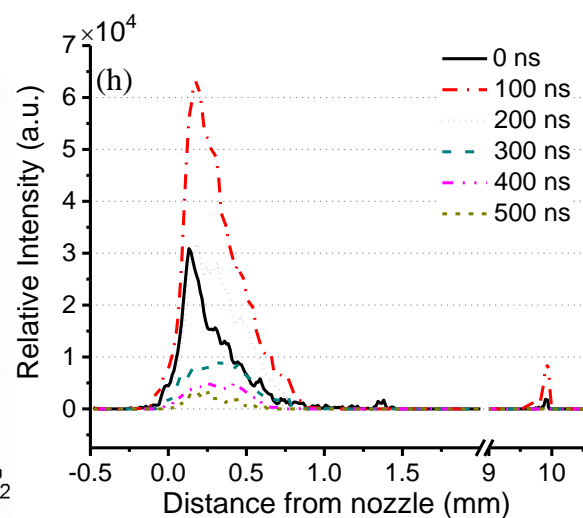
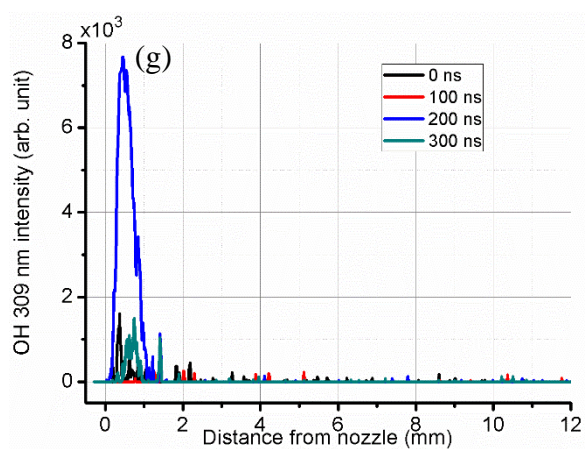
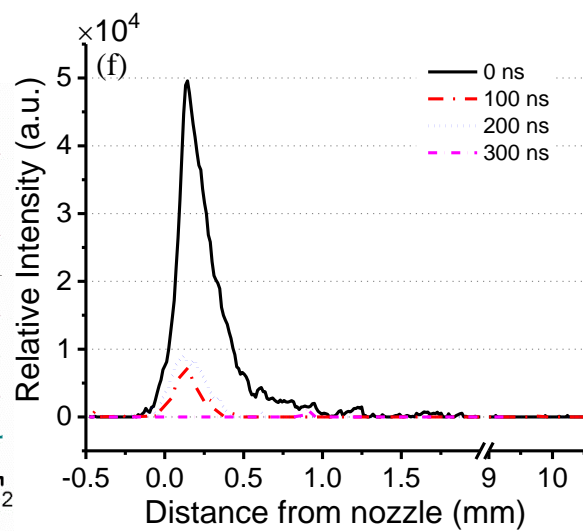
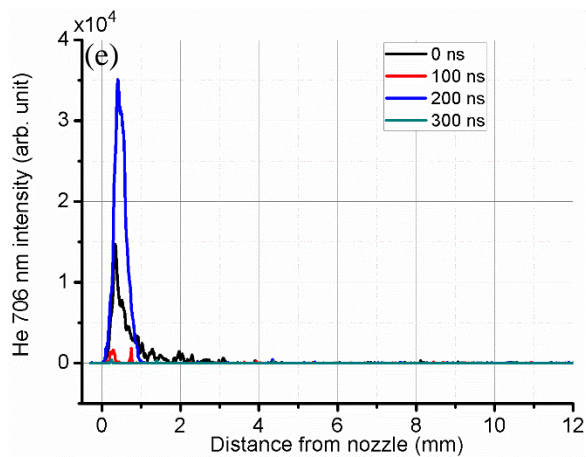


Fig. 2-9. Comparison of identified species spatiotemporally-wise for APNPJs with and without interacting with water. (a) N_2 , (c) N_2^+ , (e) He, (g) OH and (i) O are identified species without water. (b) N_2 , (d) N_2^+ , (f) He, (h) OH and (j) O are corresponding species with water [73].

In summary, study of reactive species using electrical and optical methods are carried out with and without water electrode. It is found that higher emissions of OH, N_2 , and O are greatly enhanced by introducing water electrode. The presence of water electrode strengthens the electric field of the discharge gap which favors chemical reactions in the plume. Higher electric field resulted in earlier onset of ‘guided streamer’ as well as higher jet current. Total integrated optical emissions revealed that comparable or higher intensities of identified species with water electrode.

2-4. EVALUATION OF PULSE WIDTH ON EFFECT OF OH (A-X) IN ATMOSPHERIC PRESSURE NANOSECOND PLASMA JETS IMPINGED ONTO WATER

Plasma medicine is a growing field which attracted a lot of attentions recently [4, 5, 74]. It encourages studies of ‘cold plasma jets’, especially, it is considered with interacting with water since the biological targets (cells or tissues) are either in aqueous solutions or covered by a thin layer of water [8, 69, 70]. Reactive oxygen and nitrogen species (RONS) produced in the plasma jets penetrate through the wet surface, which induce further reactions. Consequently, it affects cells and tissues in liquids [6, 70, 75]. Considering RONS generated in plasma jets, OH is of peculiar interest in many biomedical applications due to its high oxidative effect [7, 9, 76] and is considered to play an important role in cell treatment [6, 8]. Studies on effect of pulse width regarding OH generation in both gas- and liquid- phase show that the production of reactive plasma species on pulse width is not consistent. Recently, research show that liquid phase OH_{aq} was found to decrease

with increasing of pulse width from 2 μs to 10 μs [77]. Systematic studies of pulse width effects on APNPJs, especially, with short pulse widths (e.g. <500 ns) are rare. This study focuses on OH(A-X) emissions with respect to pulse width in the range of 200 ns - 5000 ns via spatiotemporal optical emission spectroscopy. The dependence of different pulse phases regarding to OH(A-X) emission intensities are investigated in details.

Experimental setup is the same as shown in Fig. 2-6 except the needle outer diameter is 0.508 mm with He flow rate of 70 SCCM and powered by 6 kV, 200 ns pulses at 1 kHz. The water electrode is grounded with the transmission line ground from the power supply.

Fig. 2-10 shows the voltage and jet currents from varying pulse widths. The voltage waveforms indicate that they all have the same shape of rising- and falling phases while the plateau is longer for longer pulse width. Jet currents for pulse widths from 200 ns to 1000 ns show that they almost stay the same except longer pulse width extended longer during the plateau of voltage pulse. Additionally, Jet currents during the falling phases are different depending on the pulse widths. The positive peaks of the jet currents for various pulse widths are the same at 52 mA which are 10 times higher than their correspondent negative peaks.

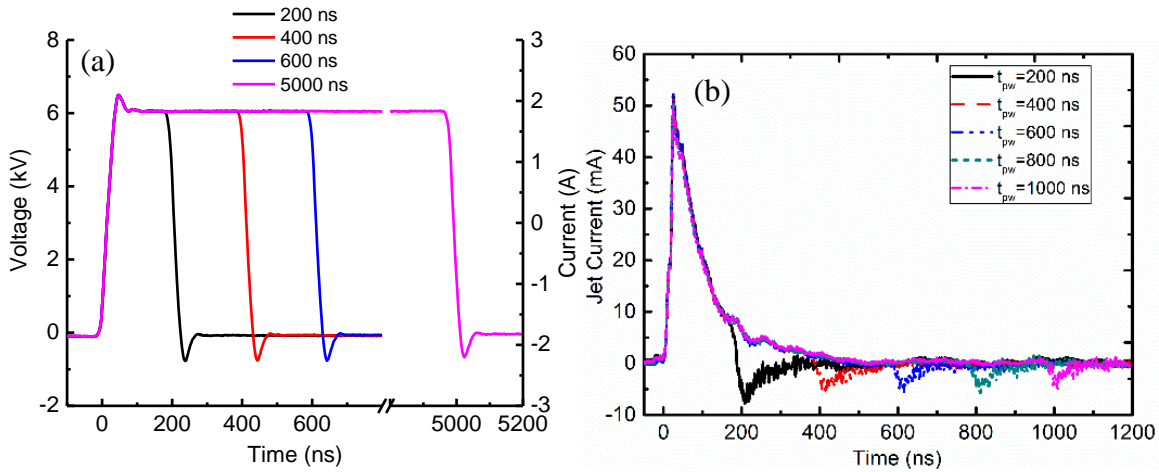


Fig. 2-10. (a) Voltage waveforms with varying pulse width from 200 ns to 5000 ns and (b) jet currents from pulse width of 200 ns to 1000 ns with increment of 200 ns [78].

Fig. 2-11 showed the time-averaged emission spectra of OH (A-X) of APNPIs compared with the simulated (Specair®) emission lines at a rotational and vibrational temperature of 310 ± 30 K and 3500 ± 30 K, respectively. The well-overlapped emission lines indicate that the variation of gas temperature over the investigated range from 200 ns to 5000 ns is negligible.

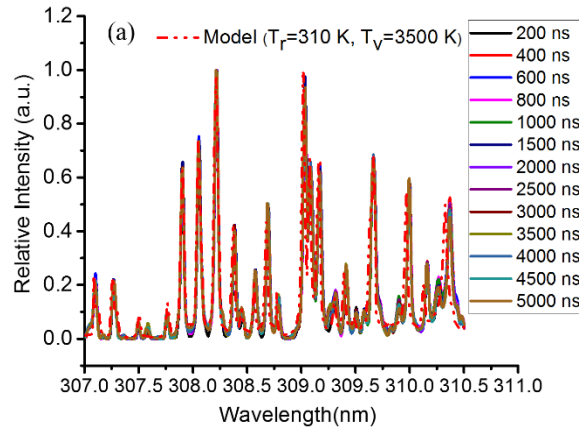


Fig. 2-11. Experimental (solid lines) and simulated (dot line) emission spectra of the OH(A-X) band for pulse widths ranging from 200 ns to 5000 ns [78].

Temporally-wised OH(A-X) emissions are studied regarding pulse width. As shown in Fig. 2-12 (a), a voltage pulse can be divided into four phases: The primary phase can be defined as the first 200 ns from the onset of the voltage pulse, τ_{prim} . The plateau phase (τ_{plat}) covers the additional plateau voltage after the primary phase. In the case of $t_{pw} = 200$ ns, $\tau_{plat} = 0$. For longer pulses, the plateau phase becomes $\tau_{plat} = t_{pw} - 200$ ns (e.g. $\tau_{plat} = 400$ ns for $t_{pw} = 600$ ns). The falling phase (τ_{fall}) is kept constant with duration of 200 ns which follows right after the plateau phase. The post-decay (τ_{post}) has a duration of 2 μ s, which starts right after the falling phase.

Fig. 2-12 (b) shows OH emissions during different temporal phases for various pulse widths. Total OH(A-X) emission intensities show that it stays about the same during the primary phase for pulse width ranging from 200 ns to 5000 ns. Total emissions increased by a factor of 2.3 as pulse width increases from 400 ns to 5000 ns. During the falling phases of the voltage pulses, the emissions of OH first increase from 200 ns to 800 ns and then, followed by an exponential decrease. OH emissions strictly decay exponentially during the post-decay phase from 200 ns to 5000 ns. If we combine the total intensities of each phase, it is shown that the total OH(A-X) increase from pulse width of 200 ns to 600 ns and then decay afterwards. It resembles the shape shown in Fig. 3-6. Both are from the same experiment except that Fig. 3-6 presents the total emission of ionization fronts from high speed imaging, whereas this figure specifically studied the OH(A-X) emissions from optical emission spectroscopy.

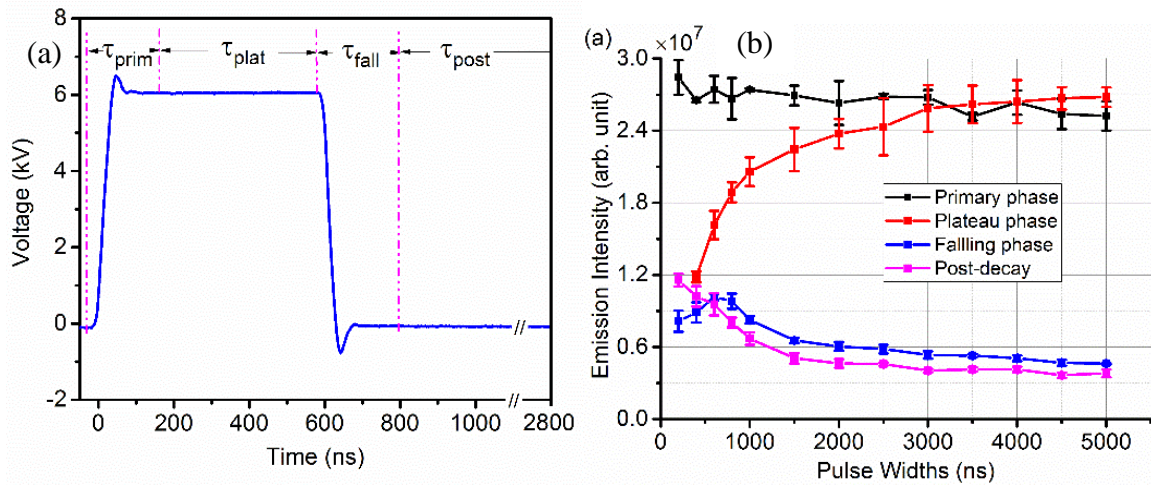


Fig. 2-12. (a) Segmentation of a 600 ns pulse into four different phases: Primary-phase, Plateau-phase, Fall-phase and Post-decay and (b) Total OH(A-X) emission intensities at each phases with respect to the pulse width ranging from 200 ns to 5000 ns [78].

In summary, emissions of OH(A-X) are studied regarding various pulse widths from 200 ns to 5000 ns when driven by 6 kV pulses at 1 kHz with He flow of 70 SCCM. It is shown that the

maximal emission of OH(A-X) occurred at pulse widths of 600 ns. Spatiotemporally resolved optical emission spectroscopy shows that majority of OH(A-X) emissions were produced during the primary phase (within the first 200 ns of a voltage pulse). Longer pulse width results in higher OH(A-X) emissions during the plateau phase and eventually, it slowly saturated. The falling phase allows the OH(A-X) emissions first increase and then decrease after pulse width of 600 ns. The falling phase which associated with secondary discharge is slightly complicated in regards to generation of OH(A-X) species.

CHAPTER 3

CHARACTERISTICS OF ATMOSPHERIC PRESSURE NANOSECOND PLASMA JETS

3-1. ABSTRACT

Study of dynamic of plasma plume matters not only to the fundamental understanding of formation of the APNPJs, but to the biomedical applications. Tunable parameters (e.g. pulse amplitude, repetition rate, and gas flow rate) are vital for biomedical treatments due to their influence on energy deposition, chemical kinetics, and repeatability of APNPJs.

This chapter studies the formation and propagation of ionization fronts in APNPJs under variable operation parameters. The ionization front of the plasma plume shortened with increasing positive voltage from 0 to 300 V whereas the plume length increased when negative voltage increased from 0 to 1000 V when these DC bias applied to a copper electrode is placed right beneath an APNPJ which operated at 7 kV, 200 ns at 1 kHz with He flow of 70 SCCM. It implies that the ionization front of the plume may contain mostly positive charges. Repeatability of the plume is examined regarding pulse amplitude (5 – 10 kV), pulse repetition rate (0.5 – 5 kHz) and He flow rate (100 – 900 SCCM). Higher repeatability of plumes is observed with higher amplitude, repetition rate, and higher flow rate. Among these tunable parameters, pulse width and He flow

rate are the most important parameters on effect of the secondary discharge, i.e. longer pulse width or higher He flow rate induces strong secondary discharges. Study of propagation of ionization fronts regarding aforementioned parameters shows that high amplitude or He flow rate result in faster propagation hence overall longer plume length, while longer pulse width or higher repetition rate trigger earlier initiation of ionization front with slower propagation speed which result in overall shorter plume length.

3-2. PROPERTIES OF A PLASMA PLUME ATMOSPHERIC PRESSURE NANOSECOND PLASMA JETS

From aforementioned results, it is found that higher amplitude, more avalanches to streamer transition would occur for both corona discharge and plasma jets. In the case of plasma jet, such transition produces a streamer development along He flow direction which is called ‘guided streamer’ [34].

If we examine the propagation of ‘guided streamer’ carefully (Fig. 1-2), it is found that the ‘guided streamer’ initiated from the needle nozzle and propagated away from the electrode with a speed in the order of 10^7 m/s, as the ionization front moving forward, a dark channel is left behind. The difference between the corona streamer and ‘guided streamer’ is of its repeatability. ‘Guided streamer’ is somehow repeatable in space and time while corona discharge is more in a randomized order [15]. There are usually two events observed which occurred at the rising and falling edge of a voltage pulse if a pulsed voltage is employed [71].

The charges at the ionization front being positive or negative is still not confirmed. What determined the repeatability of the ‘guided streamer’? What is the mechanism of the secondary discharge? How do the operation parameters (i.e. amplitude, pulse width, repetition rate, and flow

rate) would affect the development of ‘guided streamer’? In this study, the charge polarity of the ionization front is examined, the repeatability of the ‘guided streamer’ as well as the mechanism of secondary discharge are investigated. These properties are of great importance for facilitating the understanding of ‘guided streamer’. Finally, effect of operation parameters on development of ‘guided streamer’ has been investigated regarding the speed of ionization and their voltage-current characteristics.

To understand ionization fronts produced by pulsed plasma jet, a DC voltage is applied to a $7 \times 7 \text{ cm}^2$ copper plate which is placed below the needle electrode with a gap distance of 2.5 cm. The copper plate is perpendicular to the needle axial direction (shown in Fig. 3-1). When a plasma plume is generated with 7 kV, 200 ns at 1 kHz with He flow of 70 SCCM, it propagates towards the center of the copper plate. Both positive and negative DC voltages with various amplitudes were investigated. An ICCD camera is employed to capture the plume variation under the applied DC voltage with an exposure time of 100 ms without synchronization with pulsed power supply.

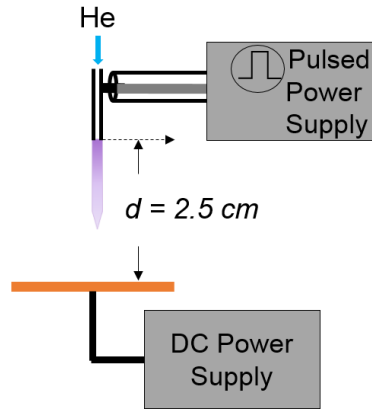


Fig. 3-1. Applying DC polarity (positive or negative voltage) beneath plasma jets, the DC power supply connected to a $7 \times 7 \text{ cm}^2$ copper plate with interelectrode gap of 2.5 cm.

Fig. 3-2 shown emission profiles of the plasma jets under various DC voltage, the upper row (a) is with positive DC bias from 0 to 330 Volts and the lower row (b) is applied with negative DC

bias in the range of 0 to -1000 Volts. It is found that the plume decreased with positive DC bias and extinct at voltage of 330 V. However, the plume is extended slowly with applying negative voltage and a second plume is formed under the primary plume when the negative DC voltage reached -400 volts. Further increase the DC bias resulted in stronger and stronger secondary plume. Eventually, the plasma plume is inhibited at DC bias of -1250 volts.

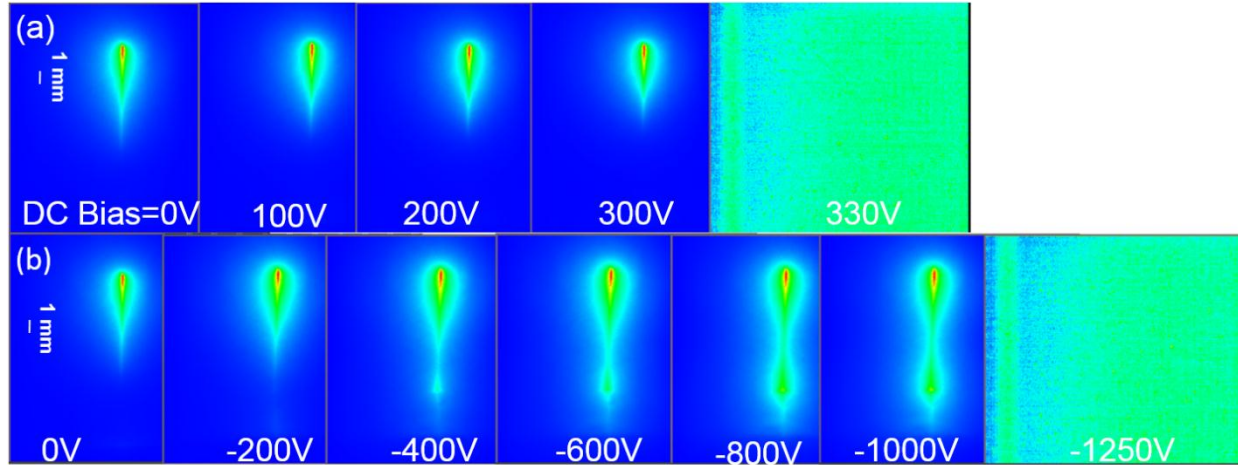


Fig. 3-2. (a) Apply positive DC voltage and (b) apply negative DC voltage.

Repeatability is a distinctive properties compared with other streamers which usually behaves in a random manner [27, 28]. In atmospheric pressure plasma jets, the plume is repeatable, i.e. the propagation of the ionization fronts is repeatable in space and time. However, the repeatability of the plume varied depending on the operation parameters. The following experiments investigated the effect of operation parameters on plume repeatability at the beginning of a voltage pulse. Experimental setup is the same with Fig. 1-7.

Fig. 3-3 presented the abnormal plume regarding various applied voltage at time 0. Figure (a) shows the applied voltage with time delay and (b) plots the counts of abnormal plumes in total captured 50 plumes. Abnormal plume is defined regarding the normal plume which are the most frequent identical plumes that occurred in 500 total counts. That's to say, any observed plume at the fixed time delay (here we use time 0) is either normal plume or abnormal plume. All images

were capture by the ICCD camera with single shot. The baseline condition is 10 kV, 200 ns at 4 kHz with He flow of 400 SCCM unless indicated otherwise.

As one can see from Fig. 3-3, images captured at time 0 at various voltage showed that higher voltage indicates higher amplitude. Figure (b) showed the number of abnormal plume over total 50. Results shown that number of abnormal plumes decreased with amplitude except at 9 kV which has a slight jump compared with others. It indicates that higher amplitude could result in more repeatable plumes.

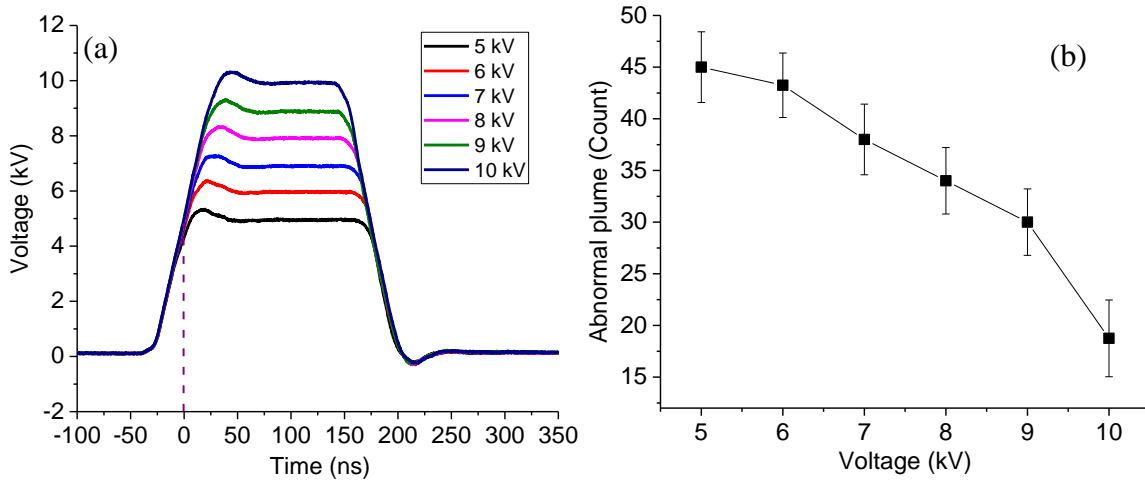


Fig. 3-3. Abnormal plume counts among total 50 under 200 ns at 4 kHz with He flow 400 SCCM with varying amplitude from 5 kV to 10 kV.

Fig. 3-4 shows the repetition rate on number of abnormal plume. Plume is captured at time 0 as show in Fig. 3-4 (a) which corresponds to amplitude of 5 kV. Figure (b) presented the number of abnormal plume versus repetition rate in the range from 500 Hz to 5000 Hz. It is found that the number of abnormal plume decreased linearly from 50 down to 25 with repetition rate. As aforementioned, higher repetition rate could have stronger memory effect which provides more seed electrons for the next discharge. As long as the voltage is sufficiently high (it is in this case), higher repetition rate favored the reproducibility of plumes in space and time.

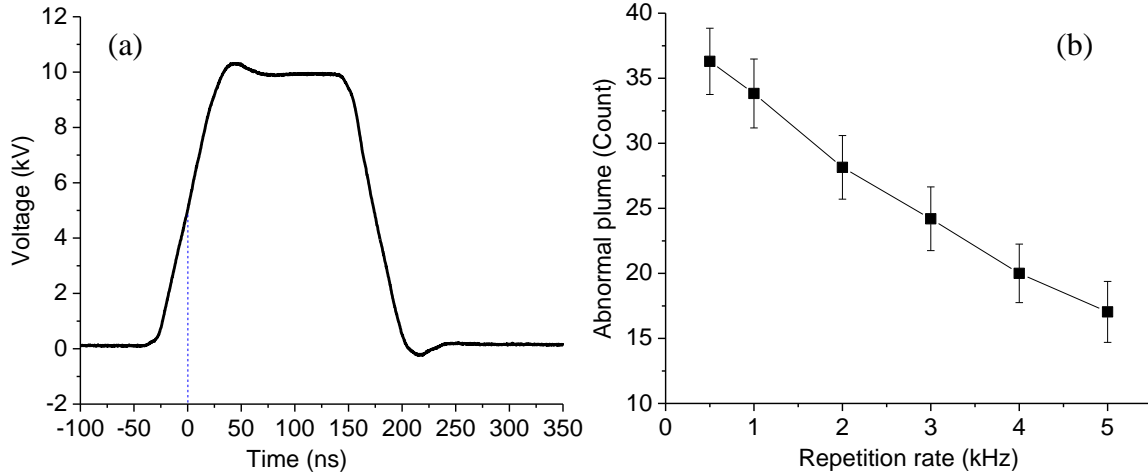


Fig. 3-4. Abnormal plume counts among total 50 under 10 kV, 200 ns with He flow 400 SCCM with varying repetition rate from 500 Hz to 5 kHz.

Effect of He flow rate on abnormal plume was investigated. As shown in Fig. 3-5, the flow rate is from 100 SCCM up to 900 SCCM. Results show that the number of abnormal plume decreased from 30 counts to 12 counts when flow rate increased from 100 to 400 SCCM. Once the flow rate reached 400 SCCM, number of abnormal plume remained almost constant even the flow rate kept increasing.

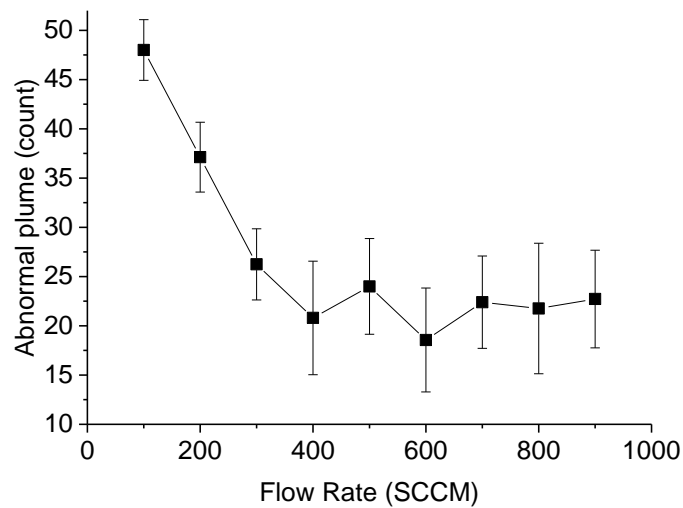


Fig. 3-5. Abnormal plume counts among total 50 under 10 kV, 200 ns at 4 kHz at He flow from 100 to 900 SCCM.

In short, different results were observed and it is found that they are quite different for three different cases of varying flow rate, amplitude, and repetition rate. They are highly variate,

however, the importance here is that they showed a trend that the discharge repeatability will increase with higher flow rate, repetition rate, and voltage amplitude.

As shown in Fig. 1-2, a primary (0 - 50 ns) and a secondary (170 - 210 ns) discharge are usually detectable when a pulsed voltage is applied. The primary discharge which is a 'guided streamer' that initiated near the tip of needle as an ionization front and propagates away from the needle electrode. Such propagation is thought to be caused by energetic photons that can effectively generate photoelectrons in front of the ionization front (even though such photons are randomized while only near the ionization trail could be effectively pulled into the main stream). Once the ionization front propagated further away from the needle, the effect of external field generated by the needle electrode has little impact on the front which resulted in vanishing of the ionization front. If the pulse width is long (e.g. 1000 ns), it is totally dark during the plateau of a voltage pulse after the primary discharge disappeared. A secondary discharge is observed once the voltage starts to decrease. Its emission is relatively weak which mostly localized near the needle nozzle.

Study of the secondary discharge showed that longer pulse width, stronger secondary discharge from pulse width of 200 ns to 600 ns. Emission intensities slowly decreased from 600 ns to 5000 ns. As shown in Fig. 3-6, emission intensity in air showed that the maximum peak intensity of the secondary discharge is at pulse width of 600 ns. It increased rapidly as the pulse width increases from 200 ns to 600 ns which indicates the separation with primary discharge could favor the secondary emission. However, the peak emissions started to decrease if two discharge events separate too long (here if pulse width > 600 ns).

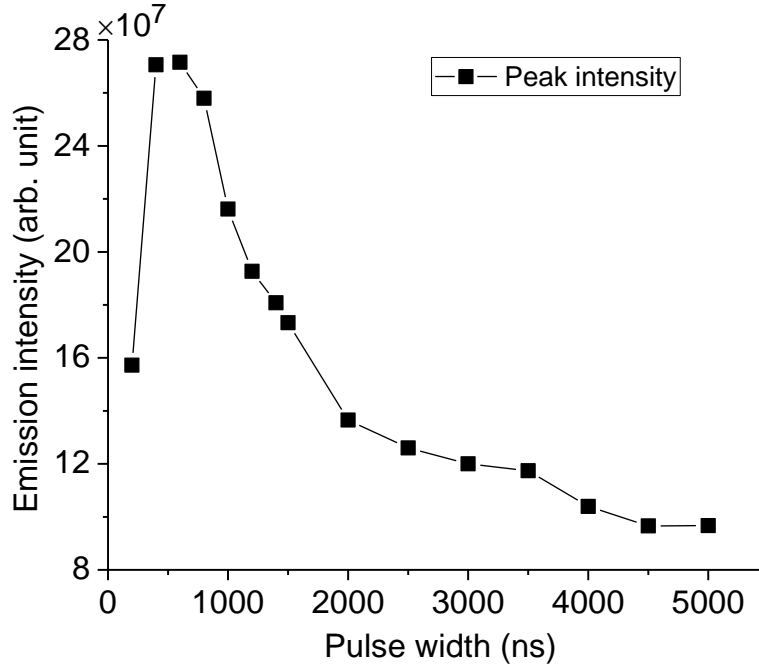


Fig. 3-6. Peak emission intensity from secondary discharge at 7 kV, 200 ns at 1 kHz with He flow of 70 SCCM with varying pulse width from 200 ns to 5000 ns.

Increasing He flow rate will also increase the intensity of the secondary discharge. As He/air ratio near the needle nozzle increased with increase He flow rate, more charges, excited and metastable He generated from primary discharge could be preserved near the needle nozzle and contribute to secondary discharge which greatly enhanced the emissions of secondary discharge (shown in Fig. 3-7). Adding a slide tubing around the needle serves the same purpose as increase flow rate (i.e. longer slide tubing will have stronger secondary discharge due to better preserved charges, metastables etc.).

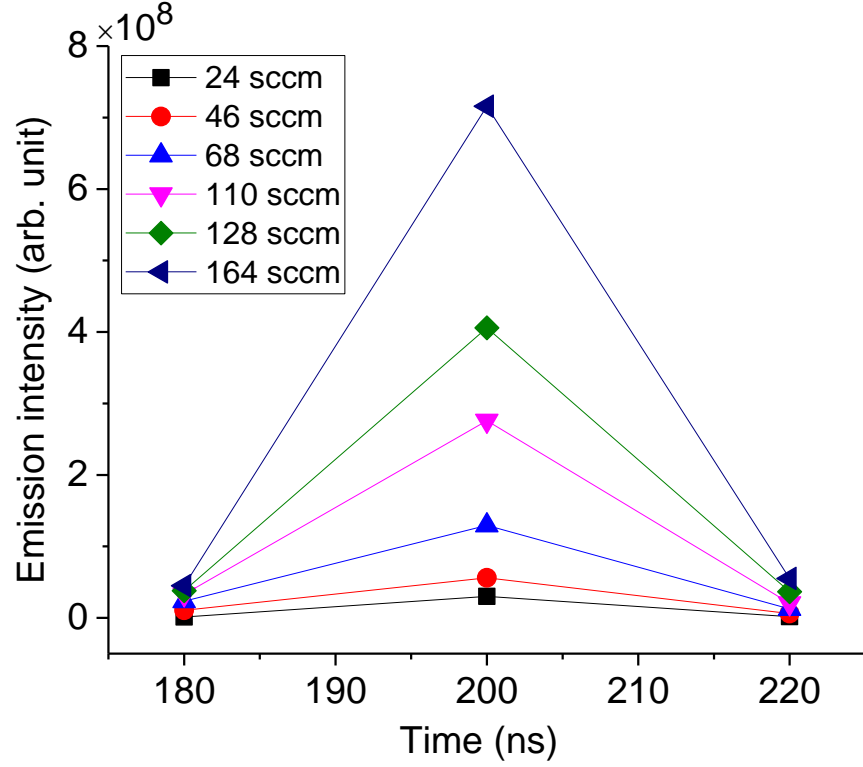


Fig. 3-7. Emission intensities of secondary discharge during the falling edge of a voltage pulse with 7 kV, 200 ns at 1 kHz with varying He flow rate from 24 SCCM to 164 SCCM (too weak at He 8 SCCM).

The formation of secondary discharge can be explained as follow: ionization front in the primary discharge generates lots of electrons, ions, and metastables as it propagates. Positive ions and negative ions mixed together at the tail of the ionization front which forms quasi-neutral plasma. Electric field generated by the needle slowly restored its strength as ionization front propagate away since both contain positive charges. The restored field has highest impact near the needle nozzle and starts to pull negative ions and push positive ions which disturbed the quasi-neutral near the needle nozzle. The space charges then formed a dipole as shown in Fig. 3-8.

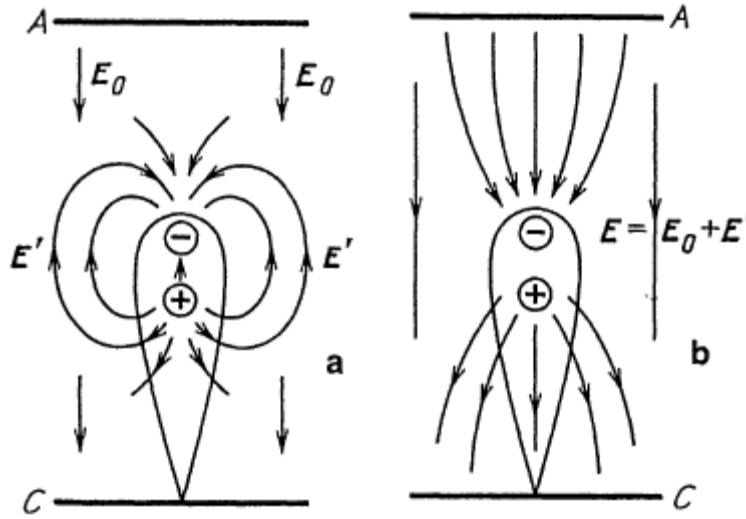


Fig. 3-8. A dipole formed in the discharge gap with two parallel plate containing an electron avalanche, A and C are the anode and cathode, respectively [1].

A sandwich structure of charge layers slowly formed (i.e. the positive electrode, negative ions and positive ions). If, however, it reached the falling phase of a voltage pulse, motion of the ions will slow down quickly due to rapidly dropped external voltage. If the layer of positive charges accumulate not enough charges, it cannot produce strong enough electric field to initiate a secondary discharge even though there is abundant electrons, ions, and metastables near the nozzle which could greatly reduce the initiation of a discharge. If the pulse width is long enough that allow the layer of positive charges formed strong enough, a reversed discharge towards the positive space charges near the needle electrode would occur as soon as the external voltage rapidly decrease. Furthermore, if the pulse width extended too long, excited species, metastables, positive and negative charges near the needle electrode loss due to recombination which resulted in weaker emissions. However, longer pulse width always resulted in stronger initiation of the secondary discharge as seen from Fig.3-9.

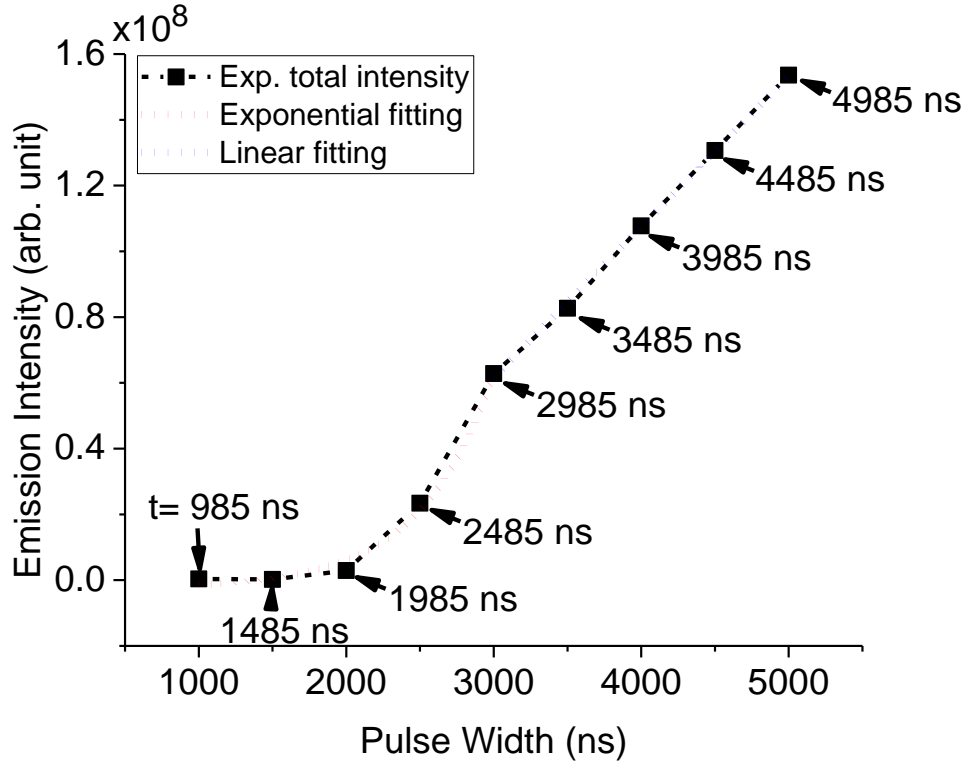


Fig. 3-9. Initial emission intensities of secondary discharge during the falling edge of a voltage pulse with 7 kV, 200 ns at 1 kHz with varying pulse widths from 1000 ns to 5000 ns and He flow 70 SCCM.

For pulse width, longer pulse width in air plasma jet, stronger secondary emission, while when pulse width is sufficiently long, the secondary emissions decrease. This is attributed to reduced effect of positive charges in streamer head when pulse width elongates, however, due to the separation of the first and secondary discharge with longer pulse, more positive charges accumulated near the needle nozzle which made the inception of secondary discharge earlier and stronger (equivalent to increase voltage amplitude: always exponential increase at the beginning $\exp(\alpha x)$) but the later on development is weaker and become linear increase due to first, a dynamic steady state has formed near the nozzle which resulted in a steady positive space charge (no more increase) and secondly, lack of metastables and excited species (they have no charges so tend not to be affected by E-field and die down with time and collision of moving heavy particles during their charge built up processes).

In conclusion, secondary discharge is initiated by the space charge near the needle nozzle. From the perspective of energy usage, secondary discharge is driven by energy stored from primary discharge. It is of great importance to understand such a mechanism and we should calculate energy deposited from power supply by integrating the voltage and the primary pulse of the jet current.

3-3. EFFECTS OF OPERATION PARAMETERS ON ‘GUIDED STREAMER’ IN AMBIENT AIR

As aforementioned, development of ionization front with space and time showed the detailed development of ionization front. However, how the operation parameters (i.e. pulse amplitude, pulse width, repetition rate, and He flow rate) could affect such development is still unclear. From the study of breakdown of plasma jet, it is known that higher amplitude results in stronger external electric field hence caused stronger emission and higher breakdown probability, meanwhile, higher amplitude allows the plume more repeatable. It is reasonable to deduce that higher amplitude may favor the propagation of ionization front hence it will travel longer distance. As shown in Fig. 3-10 (a) and (b), figure (a) is the spatiotemporal development of ionization front at voltage amplitude from 5 kV to 10 kV. Line with different color represents different distribution of ionization front at different amplitude. It is found that at low amplitude (e.g. at 5 kV), the ionization front will first travel away from the nozzle and then slowly shrink later on instead of traveling outwards. If the amplitude is strong enough, the ionization fronts could gradually propagate away from the needle electrode until it dies out further away from the electrode. The higher the amplitude, the sharper the slope of the curve. An estimated formula has been obtained from fitting this propagation trajectory.

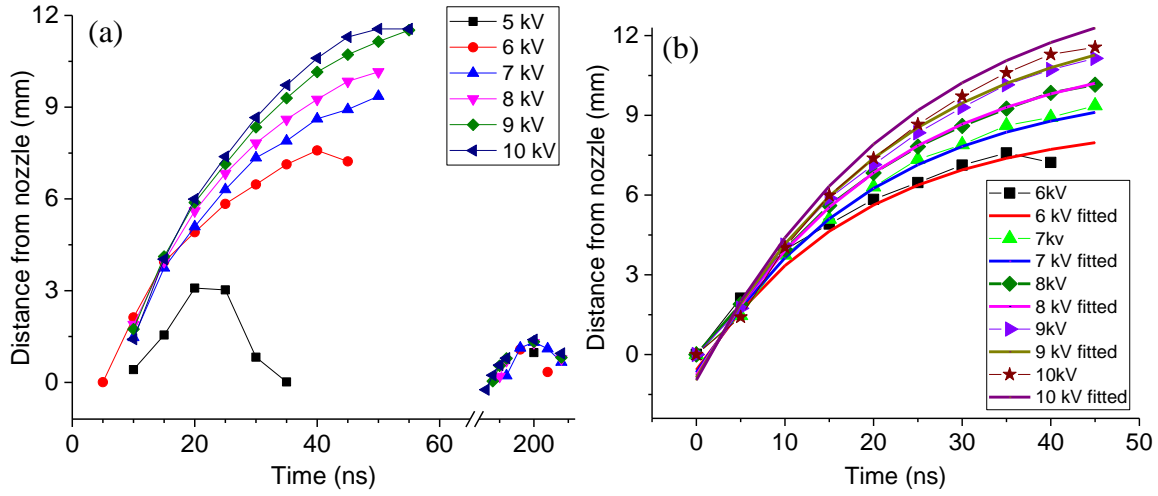


Fig. 3-10. (a) Propagation distance of ionization front from nozzle and (b) fitted projectiles of propagation at different time regarding a voltage pulse of 200 ns at 1 kHz at He 70 SCCM with varying amplitude from 5 kV to 10 kV.

$$f(t) = k * V * (122 - 130 * e^{-\frac{0.133}{\sqrt{V}}t}) \quad (2-1)$$

Where V is the applied amplitude (kV), t is the time delay (ns), $f(t)$ is the distance from nozzle (mm) and $k = 83$. Figure 3-10 (b) presented the fitted curve (solid lines) with the original trajectory (symbolled lines) with amplitude from 6 kV to 10 kV. It fit pretty well for most cases except that discrepancies occurred for the lower bound (5 kV) and higher bound (10 kV).

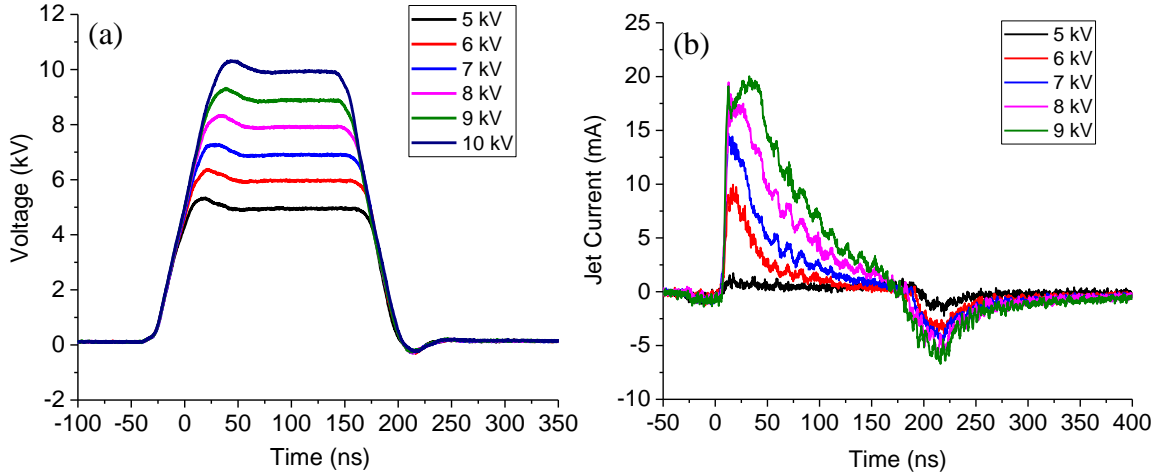


Fig. 3-11. (a) Voltage and (b) current waveforms with a voltage pulse of 200 ns at 1 kHz at He 70 SCCM with varying amplitude from 5 kV to 10 kV.

If we look at the voltage and jet current for different amplitudes (Fig. 3-11), it is found that higher amplitude results in higher jet current which implies stronger emission intensity of the ionization fronts. Jet current of 10 kV is not shown here because of the way jet current is calculated. The jet current is obtained by subtracting the assumed displacement current measured without He flow at the same pulsed voltage from that with He flow and hence the plasma was on. It represents the discharge of the ‘guided streamer’. If we associate the propagation of ionization front with its jet current, it is found that higher jet current presents faster propagation and stronger emission from ionization front.

Study of He flow rate on its propagation of ionization front is shown in Fig. 3-12. As one can see from Fig. 3-12(a), it is found that slower increase of distance from nozzle when flow rate is low, however, the propagation trajectory gets steeper as flow rate increases. Similarly, a formula regarding the flow rate on propagation of ionization front has been derived (formula (2-2)):

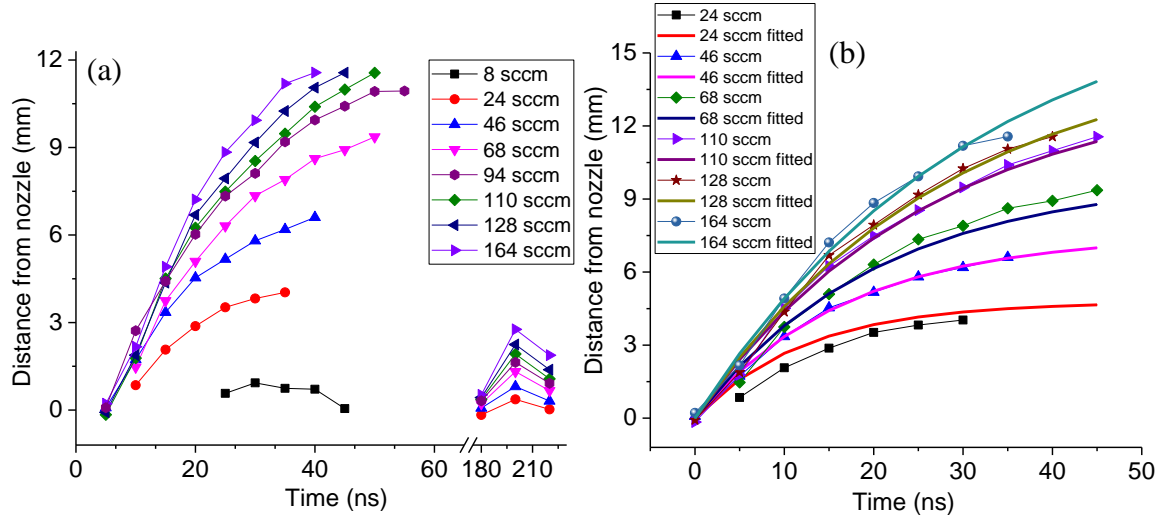


Fig. 3-12. (a) Propagation distance of ionization front from nozzle and (b) fitted projectiles of propagation regarding different time of a voltage pulse at 7 kV, 200 ns and 1 kHz with varying He flow rate from 8 SCCM to 164 SCCM.

$$f(t) = k * 43 * flow^{0.7} (1 - e^{-\frac{0.4}{\sqrt{flow}}t}) \quad (2-2)$$

Where the *flow* is He flow rate (SCCM), *t* is the time (ns), *f(t)* is the distance from nozzle in mm and *k* = 83. Fig. 3-12 (b) presented the fitted values (solid lines) using formula (2-2) and the original data points (symbolled lines). It is found that the formula can generate good fitting for almost all the flow rate except for 24 SCCM which is slightly discrepant.

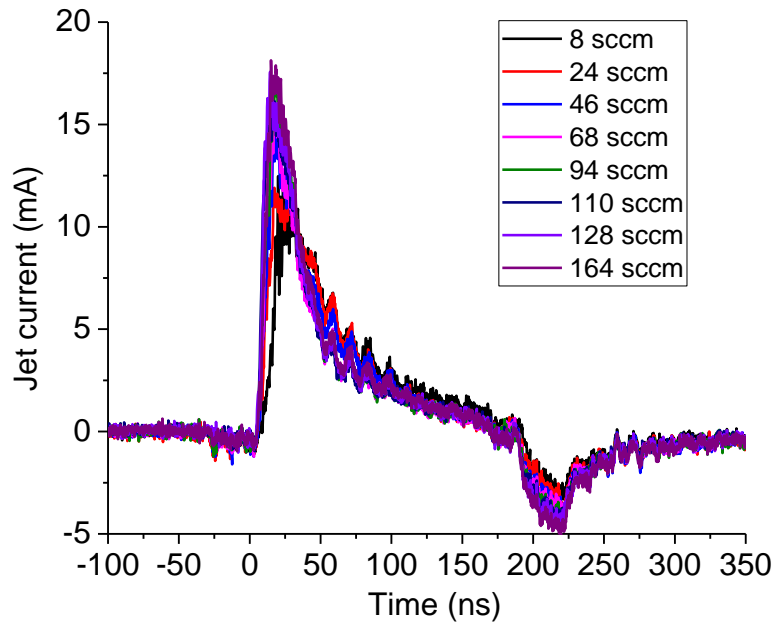


Fig. 3-13. Current waveforms regarding a voltage pulse of 7 kV, 200 ns at 1 kHz with varying He flow rate from 8 SCCM to 164 SCCM.

Considering the voltage and jet current (Fig. 3-13) under different flow rate, it is found that the higher flow rate results in more rapidly increasing of jet current and higher maximum current. In atmospheric air, the speed of electrons are in the order of 10^7 m/s while ions are about 10^5 m/s, so it is reasonable to assume that electrons are the main source to contribute the jet current, rapid changing of jet current revealed that more energetic electrons are generated in higher flow rate.

Effect of repetition rate on propagation of ionization front is investigated as shown in Fig. 3-14. Figure (a) and (b) are the jet current and spatiotemporal evolution of ionization front with respect to various repetition rate ranging from 10 Hz to 4 kHz. As seen from figure (b), higher repetition rate could favor the inception of discharge which result in earlier inception compared to lower repetition rate, however, ionization front under lower repetition rate can propagate much further. The lower repetition rate, the further it will propagate. Accordingly, lower the repetition rate, higher the jet current (fig. 3-14 (a)). The maximum current at repetition rate of 10 Hz is more than 2 times higher than that of 2 kHz.

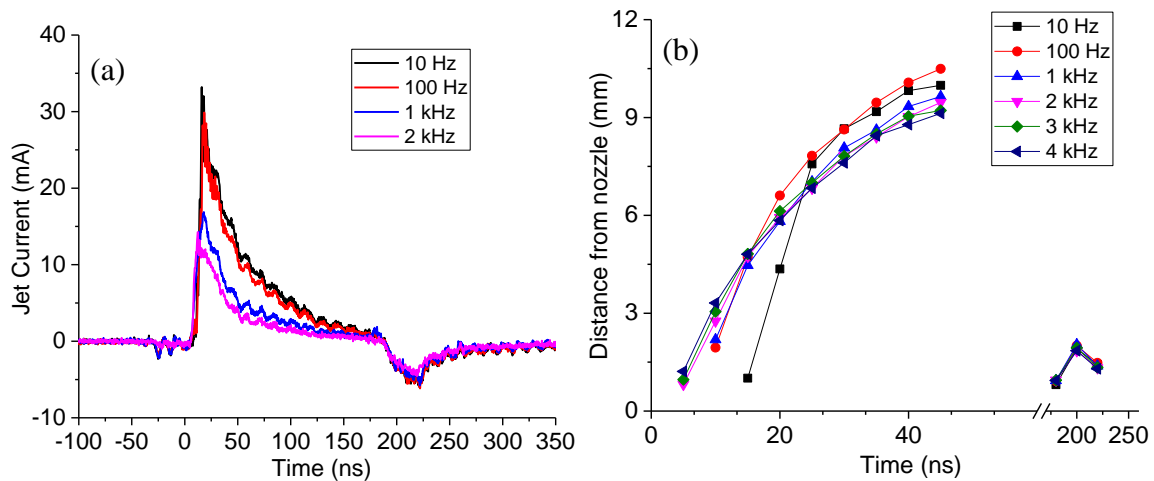


Fig. 3-14. (a) Current waveforms and (b) propagation distance of ionization fronts with a voltage pulse of 7 kV, 200 ns at He 70 SCCM with varying repetition rate from 10 Hz to 4 kHz.

Fig. 3-15 presented the propagation of ionization front with various pulse width ranging from 400 ns to 990 μ s. Figure (a) and (b) presented the jet current and evolution of ionization fronts with different pulse width, respectively. As seen from figure (b), it is found that the trajectories of ionization fronts from pulse width of 400 ns to 5000 ns are almost the same, i.e. the ionization front propagates the same distance from nozzle at the same time delay. However, this does not imply that pulse width has not impact on the evolution of ionization front. As the pulse width further increases, i.e. the pulse off period is further shortened between two consecutive pulses (e.g. pulse width of 850 μ s and 990 μ s), the inception of the ionization front occurred much earlier followed by a slower travel trajectory compared with pulse width in the range of 400 – 5000 ns. In addition, if we compared pulse width of 850 μ s with 990 μ s, it revealed that longer the pulse width, stronger the inception and followed by slower trajectory.

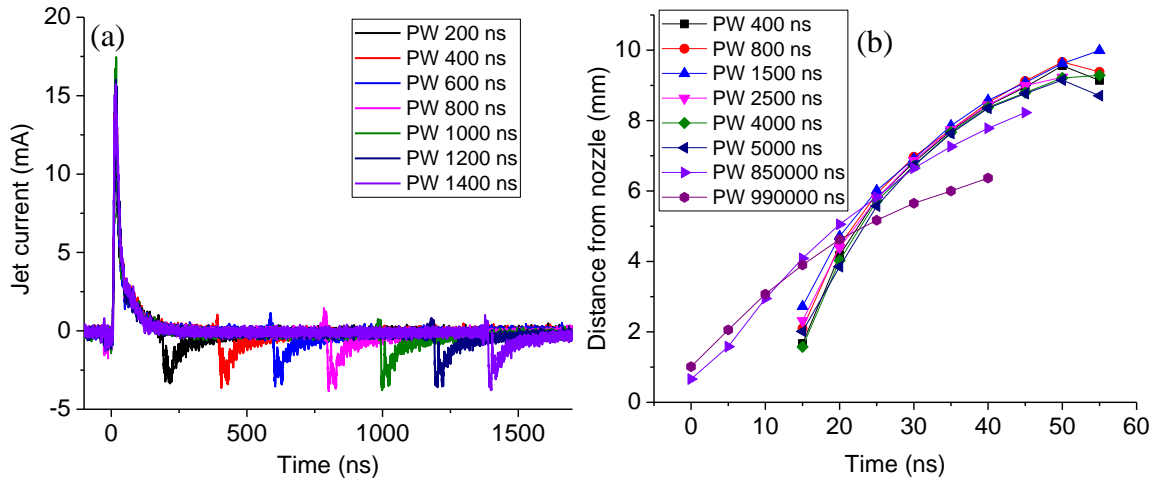


Fig. 3-15. (a) Current waveforms and (b) propagation distance of ionization fronts regarding voltage pulses of 7 kV, 200 ns at He 70 SCCM with varying pulse width from 200 ns to 990 μ s.

Needle diameter is an important parameter for development of ‘guided streamer’. Fig. 3-16 (a) and (b) presented the jet current and its corresponding propagation of ionization fronts regarding various needle diameters (i.e. 25 gauge (diameter = 0.508 mm), 28 gauge (diameter = 0.356 mm) and 30 gauge (diameter = 0.254 mm)). Figure (b) indicated that smaller diameter has earlier

inception of ‘guided streamer’, additionally, earlier inception associated with slower trajectory of the ionization front.

From previous results, it showed that steeper trajectory means higher jet current which also holds true in this case. As one can see from figure (a), their correspondent jet currents showed that higher jet current correspond to larger diameter while smaller diameter associated with earlier rise of the jet current.

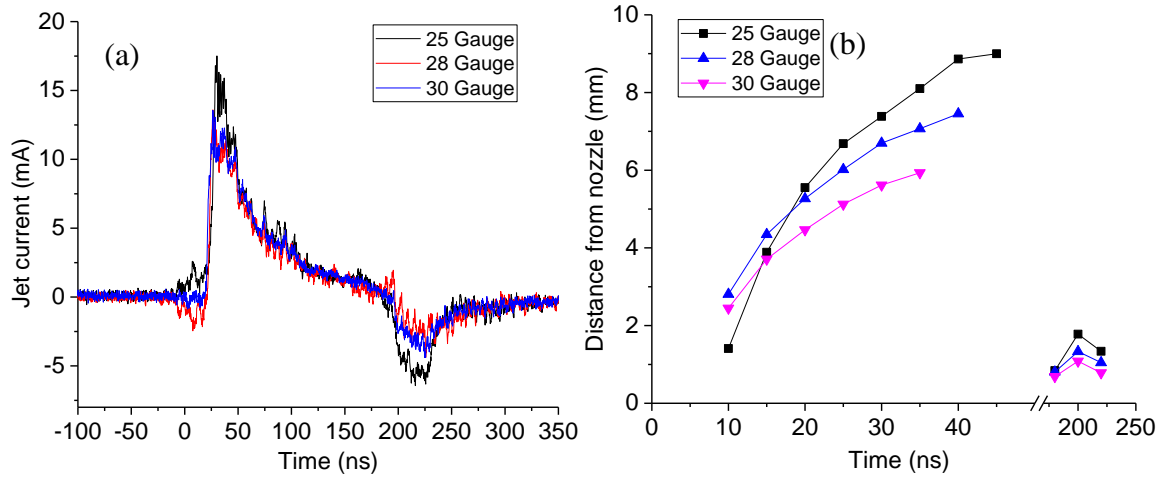


Fig. 3-16. (a) Current waveforms and (b) propagation of ionization fronts regarding voltage pulses of 7 kV, 200 ns at He 70 SCCM with varying needle diameters.

In summary, chapter 3 concentrates on dynamics of the ‘guided streamer’, including the properties of a ‘guided streamer’ (e.g. charge polarity of ionization front, repeatability of plume, and secondary discharge) and the development of the ‘guided streamer’ regarding various operation parameters (i.e. pulse amplitude, pulse width, repetition rate, He flow rate and diameter of electrode). It is found that the ionization front is concentrated with positive charges if a positive voltage is applied. Meanwhile, the repeatability is strongly dependent on the residual from previous pulses, any parameters which could result in richer source of seed electrons would increase the repeatability of the discharge (such as increase repetition rate). More importantly, the mechanism of the secondary discharge is revealed which implies that secondary discharge is using

the stored energy from the primary discharge. The loss of seed electron sources with long pulse and the strengthened positive space charges near the electrode will work together in opposite ways to contribute to the secondary emission. That is to say, the longer the pulse width, the less seed electrons while more accumulated positive charges. We've already known that more positive charge equivalent to increase the voltage amplitude, thus produces stronger secondary discharge. On the contrary, less seed electrons will weaken the secondary discharge. In combination, secondary discharge will become stronger as the pulse width increases at the beginning (i.e. from 200 ns to 600 ns) and then followed by a decrease afterwards (e.g. from 600 ns to 5000 ns).

Considering the effect of pulse amplitude and He flow rate, it is arguably true that these two parameters generate similar behavior on propagation of ionization front as well as on its associated jet current. In addition, long pulse behaves similarly with high repetition rate. That is long pulse and high repetition rate could result in earlier inception of 'guided streamer' but slower trajectory of ionization fronts.

CHAPTER 4

ELECTRICAL BREAKDOWN IN AIR CORONA AND ATMOSPHERIC PRESSURE NANOSECOND PLASMA JETS

4-1. ABSTRACT

Repeatability and stability of APNPJs are of great importance in biomedical applications. Reproducible treatment results rely on various parameters (e.g. variability of biological targets, stability of plasma jets). Minimize the variation of plasma jets is an effective way to improve the repeatability of treatments.

In this chapter, the effects of memory effect, seed electrons as well as tuning parameters on breakdown probability in APNPJs are examined. Single shot images captured by high speed imaging are analyzed to obtain the breakdown probability. Two single shot images with and without He flow are recorded which revealed the corona discharge occurred without He flow, importantly, it can also be mixed in the plasma jet hence branching the plasma plume when both

driven by 10 kV, 200 ns pulses. The breakdown probability of a normal operation in air corona (i.e. without He flow) is ~7% while it is ~87% if injected with excessive electrons at the beginning of the discharge. These results imply that the memory effect from previous pulses could alternate the breakdown probability of the following pulses hence affect the repeatability and stability of discharge. Comparison of the single-electrode discharge with (air corona discharges) and without He flow (plasma jets), it is found that higher amplitude increases the breakdown probability in both discharges. However, the breakdown probability in plasma jet reaches 100% at amplitude of 8 kV which is earlier than that of air corona discharge. Study of pulse widths from 0.2 μ s to 5 μ s in both discharges show that the longer pulse widths, the higher breakdown probability and the breakdown probability reaches 100% at 1 μ s for APNPs and 10% at 5 μ s for air corona. The breakdown probability of air corona increases from 0 to 5% with pulse repetition rate increasing from 0 to 3 kHz and decreased to 3% from 3 kHz to 6 kHz. However, the breakdown probability increased up to 100% from 0 to 100 Hz and maintains such probability afterwards. Interestingly, study of He flow rate from 35 to 200 SCCM indicates that the breakdown probability decreases from 85% down to 30%. These results imply that discharge left over from previous pulses could contribute to the next pulse which eventually modify stability of discharges. Higher amplitude and repetition rate and longer pulse width result in more stable discharges.

4-2. A GENERAL OBSERVATION OF BREAKDOWN IN NANOSECOND PULSED PLASMA JET

High speed imaging and electrical measurements are employed as diagnostic methods for breakdown study. Schematic of the experimental setup for the two methods is shown in Fig. 4-1. A plasma jet device, consisting of a hollow-needle electrode could generate a plasma plume longer

than 1 cm when it was powered by 7 kV pulses at 1 kHz and with a helium flow of 70 SCCM. The hollow needle was made of stainless steel with the inner and outer diameters being 0.254 mm and 0.508 mm, respectively. A nanosecond high voltage (HV) pulse generator (DEI PVX-4110) was used for this study. The ultra-high purity helium (99.999% minimum purity) was used as the feed gas and regulated by a mass flow controller (MKS Instruments 146C) when generate a plasma jet. An ICCD camera employed for high speed imaging which synchronized with the pulsed power is applied to study breakdown process.

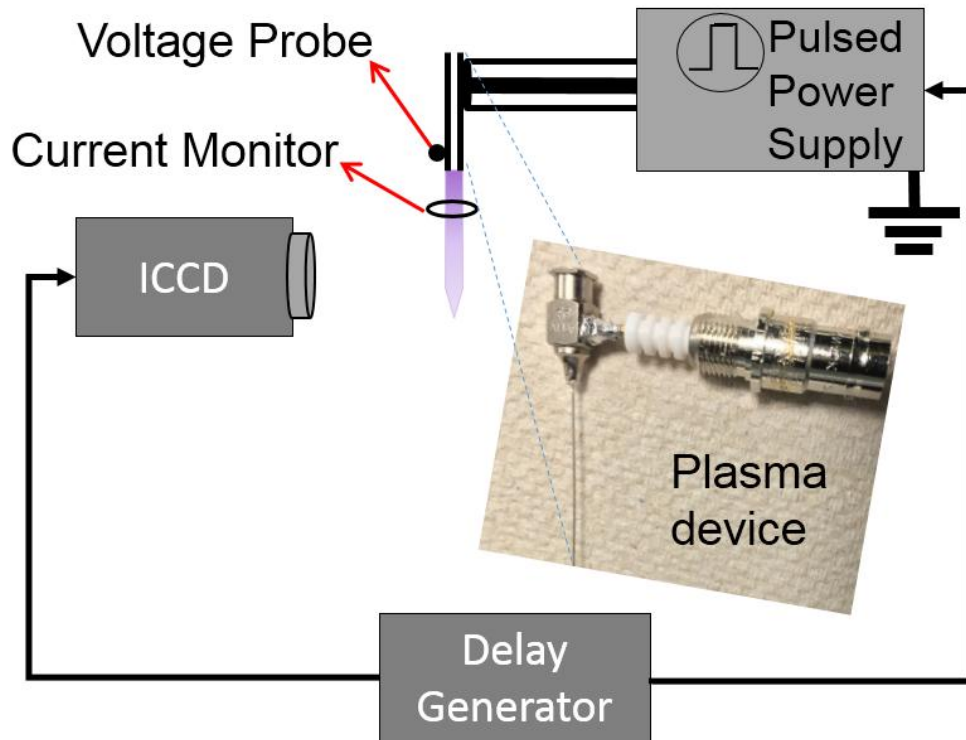


Fig. 4-1. Experimental setup of a nanosecond pulsed corona discharge in ambient air without He flow.

Fig. 4-2 (a) and (b) shown a plasma jet with He flow of 70 SCCM and without He flow (i.e. an air corona discharge) from the single needle electrode driven by a 10 kV, 200 ns pulses at 1 Hz. Both images are single shot images. As one can see, both the corona and plasma jet are quite branching which raises an important question: at such small electrode, corona is an inevitable phenomena if driven by a high voltage. Corona discharge interference is inevitable

when generating an APNPJ under some conditions. To thoroughly understand this, we will exam both corona discharge and plasma jets.

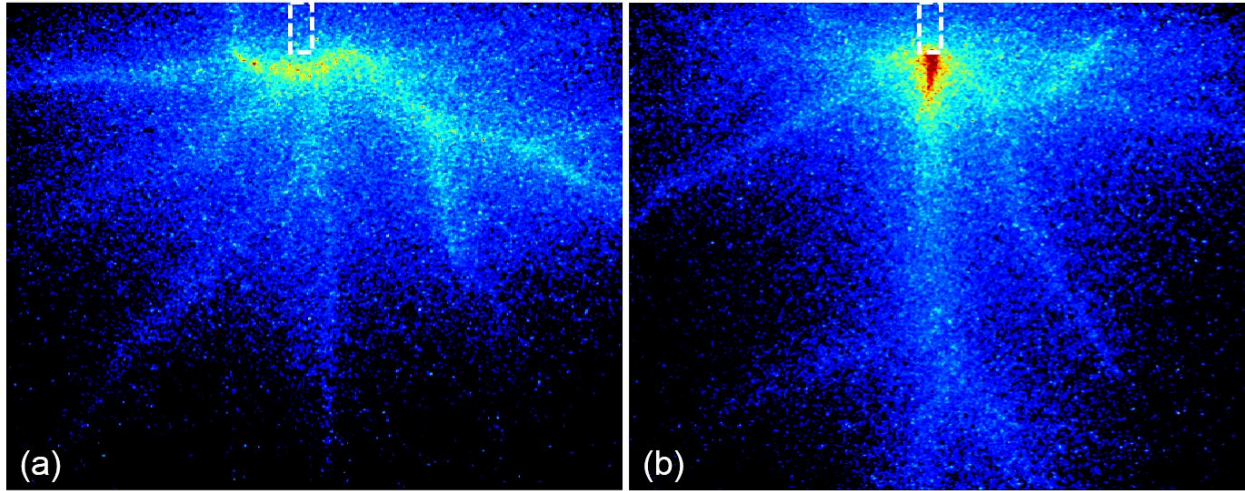


Fig. 4-2. Typical discharge from single-needle electrode (a) corona discharge in ambient air and (b) plasma jet imping into ambient air with He flow of 70 SCCM, both at 10 kV, 200 ns pulses at 1 Hz.

4-3. BREAKDOWN IN CORONA DISCHARGES

Starting with corona discharges in ambient air, the breakdown probability has been evaluated when the single-needle electrode was driven by 8 kV, 200 ns pulses at 1 Hz. Single shot image has been captured and repeated 100 times, the breakdown probability was calculated using the number of success discharges divided by the total 100 repeats. Each single shot image is accumulated over the whole voltage pulse. As seen from Fig. 4-3, at time 0 the single-needle electrode drove by a 10 kV, 200 ns pulses at 1 Hz for 15 seconds, then the discharge condition has been switched to 8 kV, 200 ns pulses at 1 Hz at time 0. The reason for operating at 10 kV for 15 s is to make sure the breakdown probability reach a value higher than zero (by providing extra seed electrons). At time 0, the breakdown probability now reached 20% (i.e. breakdown 20 times over 100 times). Then the plasma was kept running for 5 minutes which made the breakdown probability increase to

50%. After that, the plasma was turned off for 10 mins and then turned on to record the breakdown probability. As one can see, the breakdown probability decreased if the plasma is off for several minutes. However, once the breakdown probability reached about 20%, further off the plasma would not decrease the breakdown probability (Fig. 4-3 from 20 to 40 mins). If one turned off the plasma for longer duration (e.g. OFF 40 mins), the breakdown probability would further reduce. On the other hand, however, if the single-needle is touched with the pencil for about 15 ns (the pencil core provides extra electrons), the breakdown probability will abruptly increase from 4% to 70% and maintain at that high level of breakdown until the plasma ceases for 20 mins, and eventually it decreased down to 20%.

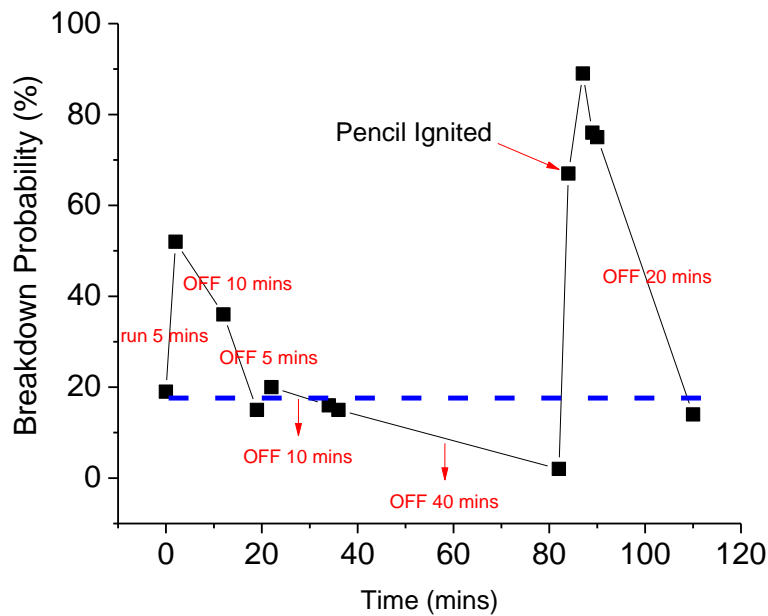


Fig. 4-3. Breakdown probability of air corona with time at 8 kV, 200 ns pulse with 1 Hz.

From this observation, one could realize that the breakdown probability heavily rely on previous discharges (i.e. seed electrons) in the discharge gap. Breakdown probability increased with providing abundant seed electrons. In addition, voltage off duration between two discharge gaps are essentially important to breakdown probability which can be attributed to the memory

effect [25]. To further analyze the effect of seed electrons on breakdown probability, three cases were analyzed experimentally as follows.

In the first case, the normal operation case in which the plasma is driven by 8 kV, 200 ns pulses at 1 Hz without any interference from previous charges. The pulsed power is always on (i.e. there is no OFF voltage time like in Fig. 4-3) and keeps driven the plasma. As shown in Fig. 4-4, each breakdown is a single shot image with exposure time (~ 400 ns) covering the whole pulse. It clearly shows that the breakdown probability which has a range from 22% to 2% during 100 mins. It implies that the breakdown at such condition is relatively stable (even though statistic) and breakdown probability is in average at 7% with a stand deviation of 7%.

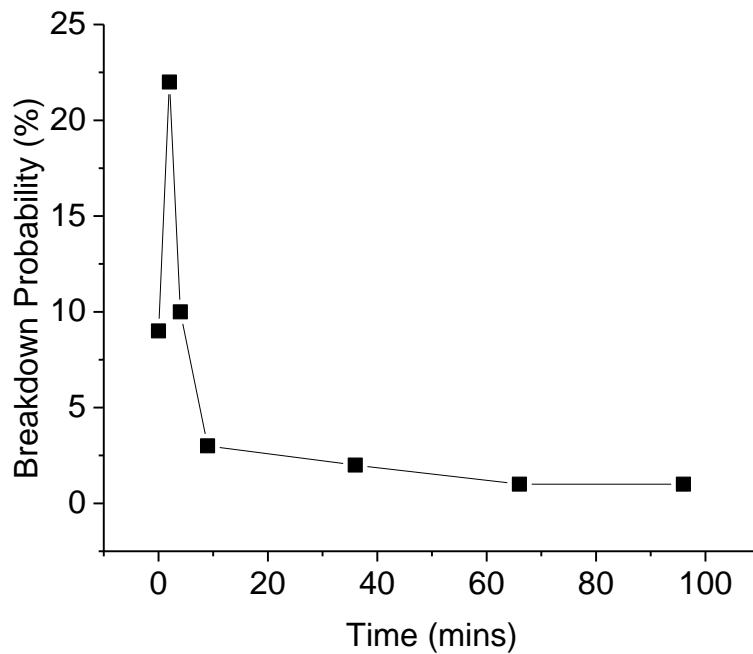


Fig. 4-4. Breakdown probability of air corona versus time under normal discharge at 8 kV, 200 ns pulses with 1 Hz.

In the second case, the excessive seed electrons have been provided by touching the pencil for about 15 ns at the beginning with other operation conditions the same as normal operation. As one can see from Fig. 4-5, the breakdown probability is quite high compared to normal operation,

which in the range from 100% to 75% during the whole 250 mins. The average breakdown probability is 87% with a standard deviation of 8.2%.

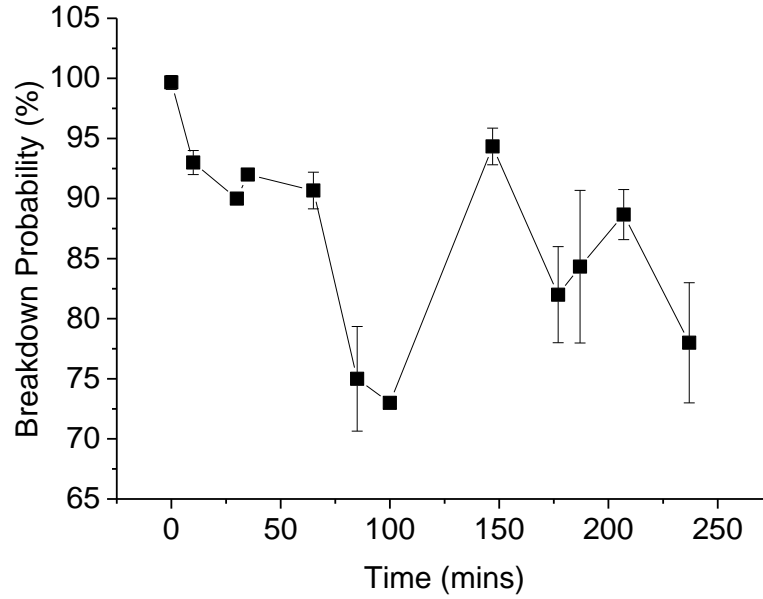


Fig. 4-5. Breakdown probability of air corona with time under excessive electrons at 8 kV, 200 ns pulses at 1 Hz.

With pencil ignition for 15 seconds.

In the third case (shown in Fig. 4-6), depletion of seed electrons was carried out by placing a tubing with an inner diameter of 4 mm perpendicular to the needle direction, the distance from the outer edge of the needle to the nozzle of the tubing is about 2.8 cm. As a start, the discharge was provided with excessive seed electrons using the same procedure performed as the second case which allows the breakdown probability at an average of 99% with a standard deviation of 1% at time 0. Then, air flows towards to the plasma with a flow rate of 6000 SCCM while keeping the plasma running. As one can see, the breakdown dramatically decreased down to about 20% in 5 mins. The average breakdown probability from 5 mins to 25 mins is about 12% with a standard deviation of 6.0%.

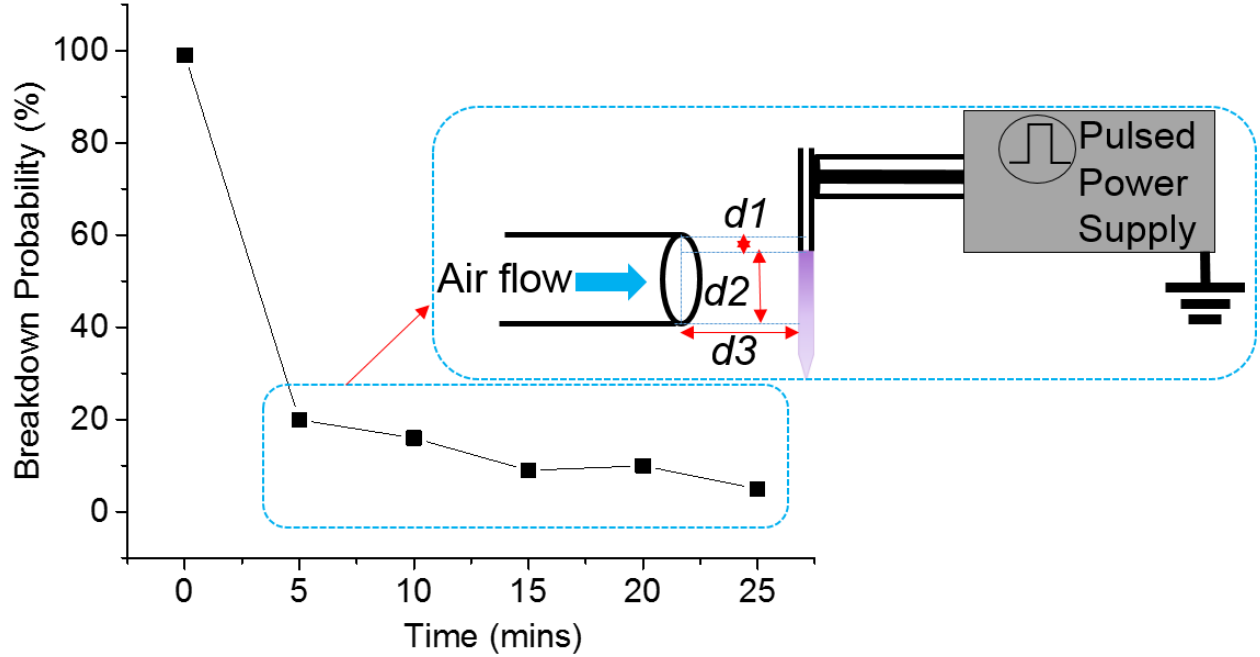


Fig. 4-6. Breakdown probability of air corona with time under with depletion electrons at 8 kV, 200 ns pulses at 1 Hz. with strong air flow 6 L/min, $d1=1$ mm, $d2=3$ mm, distance between exit of the air flow tubing to outer edge of the needle $d3=2.8$ cm.

In summary, seed electrons on effect of breakdown probability under three different conditions were examined. Results from general observation show that the memory effect generated by previous pulses could sustain up to about 40 mins at an average breakdown probability of 20% compared that the breakdown probability is in average of 7% with normal operation at 7 kV, 200 ns pulses at 1 Hz. Importantly, the discharge has an ability to retain its state. For example, the discharge was able to maintain at an average of 87% breakdown probability under the condition with excessive electrons. Even though the operation conditions are all the same comparing the normal operation with condition of excessive electrons, the resulting breakdown probability is vastly different (i.e. the ratio of breakdown probability between excessive and normal operation is $87\%/7\% = 12.4$). This can be attributed to the memory effect from previous pulses which further dramatically modified the discharge itself. Using a high flow rate targeting the discharge could

increase the loss of seed electrons that being accumulated in the discharge column and eventually bring the breakdown probability back to normal.

However, there are several questions raised from the above observations:

(1) Why is the breakdown so heavily dependent on the initial condition?

Short pulse do not favor electron accumulation, but if there are excessive electrons, series of avalanches could be launched at the same time under such short pulse which strengthen the discharge.

(2) What are the sources of the seed electrons (excited and metastable atoms, positive and negative ions? or generated stable molecules?).

There are two main reasons that the seed electrons could last such a long time: first, it hold inside the needle tubing which could be preserved longer (as seen from Fig. 4-7). Second, it's highly possible the source of these electrons is from stable species or metastables (as seen from Fig. 4-8). The metastable $O_2(^1\Delta_g)$ has a lifetime ~ 2700 s which equivalent to 45 mins.

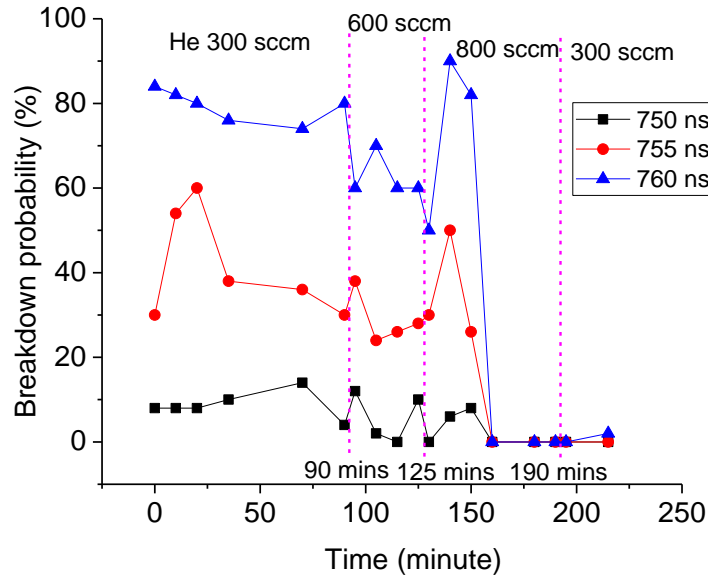


Fig. 4-7. Breakdown probability of He plasma jet at 9 kV, 200 ns pulses at 1 Hz with varying He flow at 300 SCCM during the first 90 mins, 600 SCCM from 90 mins to 125 mins, 800 SCCM from 125 mins to 190 mins and 300 SCCM from 190 mins to 220 mins.

TABLE 4-1

Excitation energy, lifetime and excitation cross sections of atoms and molecules [1]

Atom, molecule	Excitation energy, E^* eV (metastable levels: *)	Lifetime, s	Interpolation of the total excitation cross section at the threshold, $\sigma^* = C^*(\epsilon - E^*)$	
			C^* , 10^{-18} cm ² /eV	E_{eff}^* , eV
H(2s)	10.20*	0.142	25	10
H(2p)	10.20			
He(2^3S_1)	19.82*	$6 \cdot 10^5$		
He(2^1S_0)	20.6*	$2 \cdot 10^{-2}$	4.6	20
He	21.21			
Ne	16.62*			
	16.7*		1.5	16
	16.85			
Ar($4^3P_2^0$)	11.55*	> 1.3		
	11.61		7	11.5
	11.72*	> 1.3		
H ₂	8.7*		7.6	8.7
	11.5			
N ₂ ($A^3\Sigma_u^+$)	6.2*	1.3–2.6		
N ₂ ($a^1\Sigma_u^-$)	8.4*	0.5		
O ₂ ($1\Delta_g$)	0.98*	$2.7 \cdot 10^3$		
O ₂ ($b^1\Sigma_g^+$)	1.64*	12		
Hg(6^3P_0)	4.65*			
(6^3P_1)	4.87		$\sigma_{\text{max}}^* = 1.7 \cdot 10^{-16}$ cm ²	
	5.4*		for $\epsilon = 6.5$ eV	
	6.7			

To further understand the breakdown process and effect of pulse parameters (i.e. voltage amplitude, pulse width, and pulse repetition rate) on breakdown probability were investigated with a baseline condition of 7 kV, 200 ns at 1Hz. All the breakdown images were single shot images with exposure time covering a whole voltage pulse (i.e. depending on the pulse width). The breakdown probability is based on their normal operation as in the first case (Fig. 4-4) unless mentioned otherwise.

Fig. 4-8 showed the breakdown probability regarding the voltage amplitude ranging from 6 kV to 10 kV. The black and red solid lines are two repeats under normal operation while the blue dot

line represents the condition with excessive electrons. Under the normal operation, the breakdown probability increased exponentially with amplitude while largely different when driven by excessive seed electrons. The correspondent breakdown images were shown in Fig. 4-9. It indicates that higher amplitude, stronger emissions.

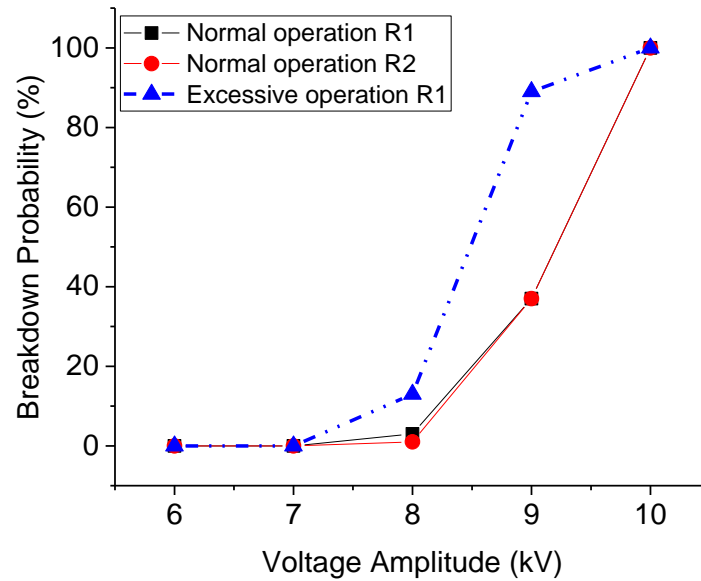


Fig. 4-8. Breakdown probability of air corona with varying amplitude (6 – 10 kV) for 200 ns pulses at 1 Hz, two repeated normal operations and one under excessive operation condition.

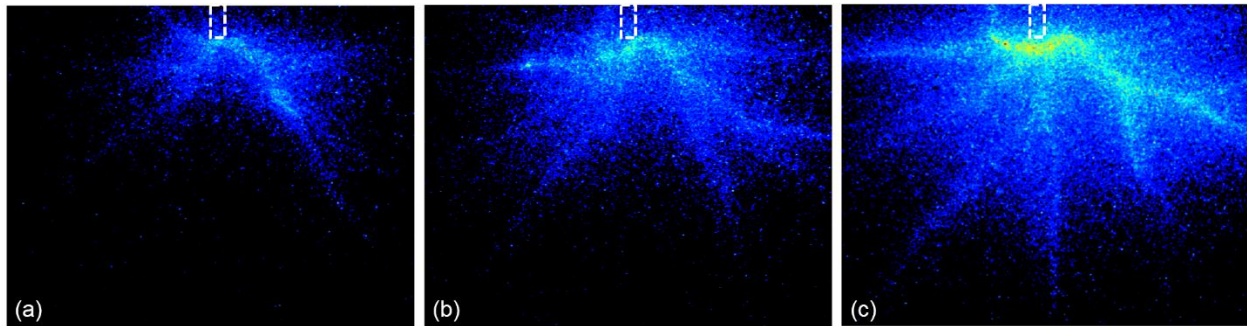


Fig. 4-9. Breakdown images of air corona with varying amplitude for 200 ns pulses at 1 Hz, single shot images (a) 8 kV, (b) 9 kV and (c) 10 kV.

Effect of pulse width on breakdown probability is illustrated in the range of 200 ns to 5000 ns. The breakdown probabilities and their correspondent sample image were shown in Fig. 4-10 and

Fig. 4-11, respectively. As one can see, the breakdown probability increased with pulse width. In addition, longer pulse width resulted in stronger emissions.

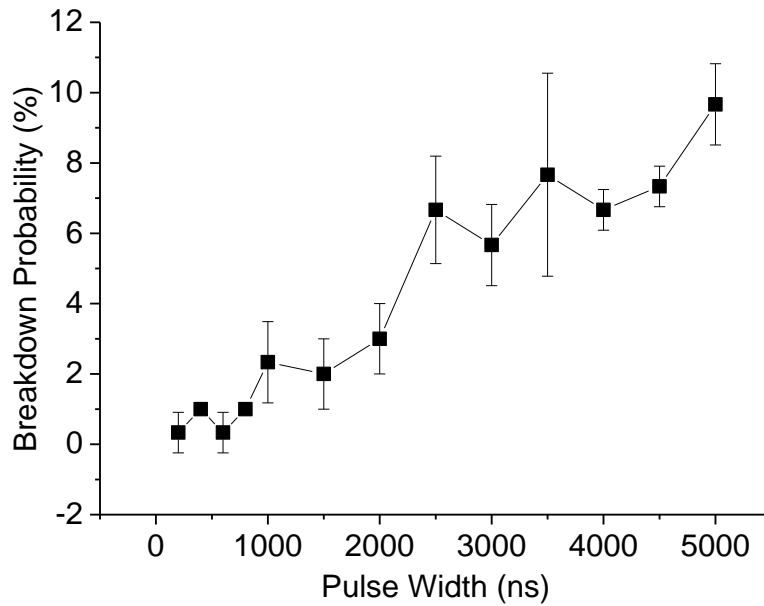


Fig. 4-10. Breakdown probability of air corona with pulse width (200 – 5000 ns) at 7 kV pulses at 1 Hz.

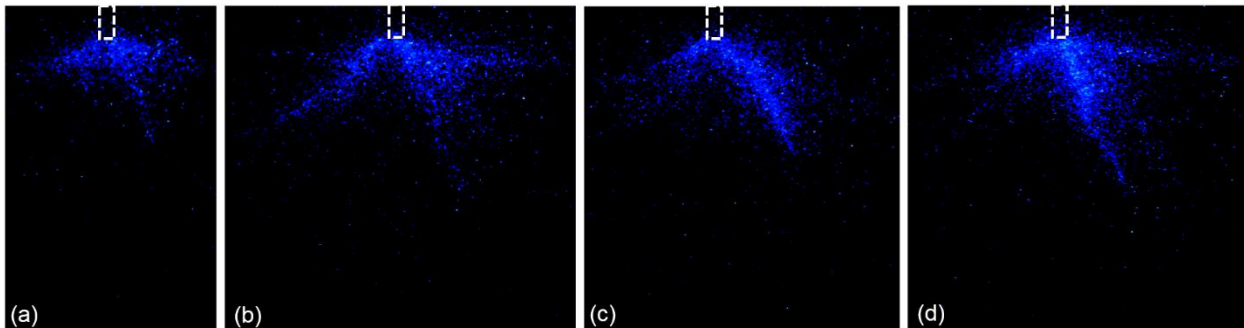


Fig. 4-11. Breakdown images of air corona with varying pulse widths for 7 kV pulses at 1 Hz, single shot (a) 400 ns, (b) 1000 ns, (c) 3000 ns and (d) 4000 ns.

When operating at 7 kV, 200 ns pulses from repetition rate of 1 Hz to 3 kHz, there is no breakdown observed. From 3 kHz to 6 kHz, however, the breakdown probability firstly increased and then slightly decreased after it reached the maximum probability at 5 kHz as seen from Fig. 4-12. Single shot images showed no appreciable difference on repetition rate.

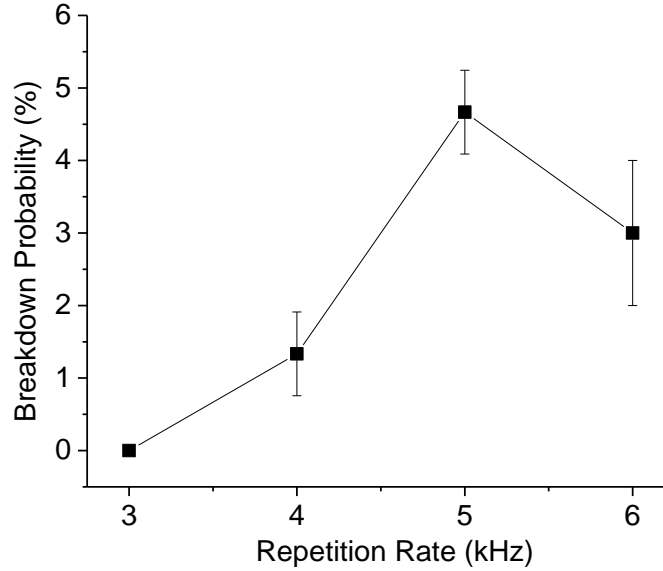


Fig. 4-12. Breakdown probability of air corona with various repetition rate (3 – 6 kHz) at 7 kV, 200 ns pulses.

In summary, breakdown probability would increase when either amplitude or pulse width increases while it will not keep increasing with repetition rate. As described in Townsend theory, the electron proliferation is proportional to $\exp(\alpha x)$. Therefore, from a single electron avalanche to streamer, the development of one avalanche at increasing collisional amplifications through two possible ways: a greater field strength (larger α) with a constant collision time; prolonging the collision time (greater x) with a constant field strength [45]. The transition from avalanche to streamer requires the proliferation reach to a certain value (i.e. $\alpha x \sim 18 - 20$). Higher amplitude creates a stronger electric field which resulted in higher α value (Fig. 4-8), hence higher breakdown probability. Longer pulse width, on the other hand, could increase x which is the travelled distance from cathode (in this experiment, it's the travelled distance from where the electron starts). In short, both amplitude and pulse width could exponentially increase the breakdown probability. Pulse repetition rate, however, is slightly more complicated since it not only increases the density of seed electrons but also decreases the total electric field [79].

4-4. BREAKDOWN IN ATMOSPHERIC PRESSURE NANOSECOND PLASMA JETS

Breakdown with varying operation parameters (i.e. pulse amplitude, pulse width, repetition rate, and gas flow rate) were studied with the same setup as in Fig. 4-1, except a gas tubing is connected to the Luer[®] cap of the needle with flowing of helium. Fig. 4-13 showed the breakdown probability under various amplitude. It indicated that higher amplitude has higher breakdown probability. Compared with the results in corona discharge in air (Fig. 4-8), it implies that it is easier to breakdown with He flow than in static air. That is, the breakdown occurs at slightly higher than 5 kV for plasma jet but for about 7 kV in corona discharge. Looking at the sample images (single shot with exposure 400 ns) in Fig. 4-14, it indicates that higher voltage, longer plume, and stronger emission with more branching.

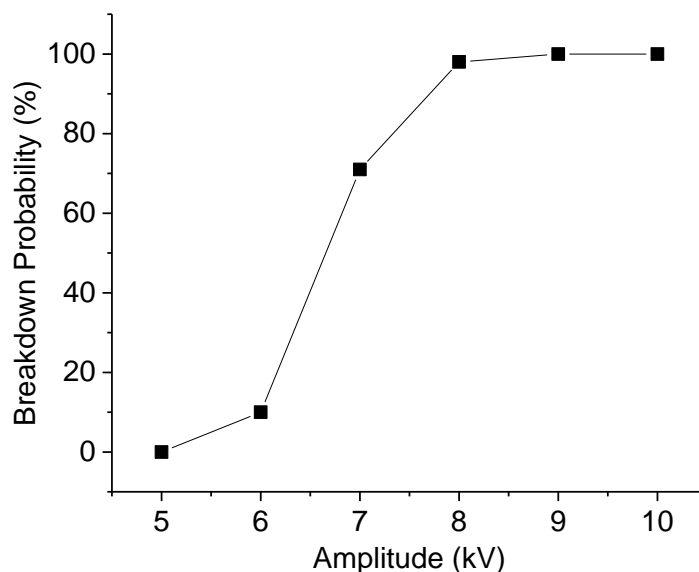


Fig. 4-13. Breakdown probability of plasma jet with varying amplitude (5 – 10 kV) for 200 ns pulses at 1 Hz with He flow 70 SCCM.

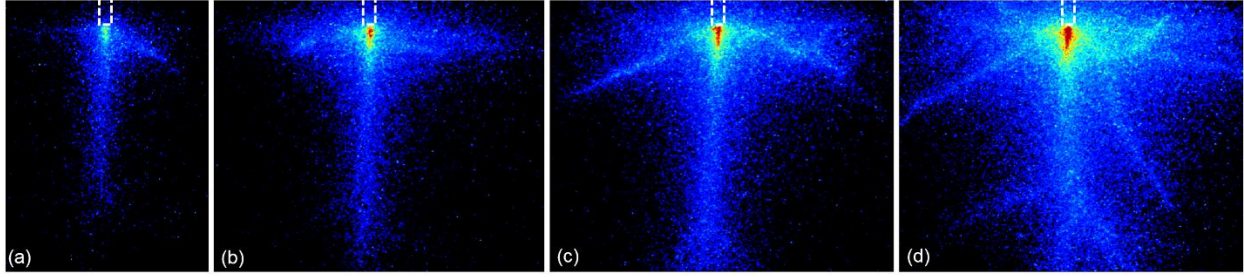


Fig. 4-14. Breakdown images of plasma jet with varying amplitude for 200 ns pulses at 1 Hz with He flow 70 SCCM with (a) 7 kV, (b) 8 kV, (c) 9 kV and (d) 10 kV.

With varying repetition rate, breakdown probability increased with repetition rate (Fig. 4-15). The breakdown probability reached 100% when the repetition rate is higher than 100 Hz (studied range from 1 Hz to 5000 Hz). As seen from Fig. 4-16, the correspondent sample images shows that higher repetition rate would result in shorter plasma plume.

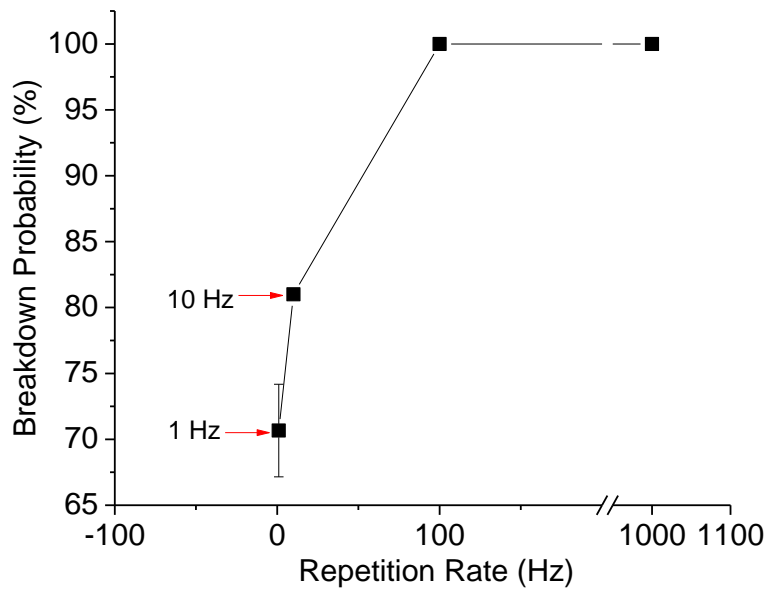


Fig. 4-15. Breakdown probability of air corona with repetition rate (1 – 1000 Hz) at 7 kV, 200 ns pulses.

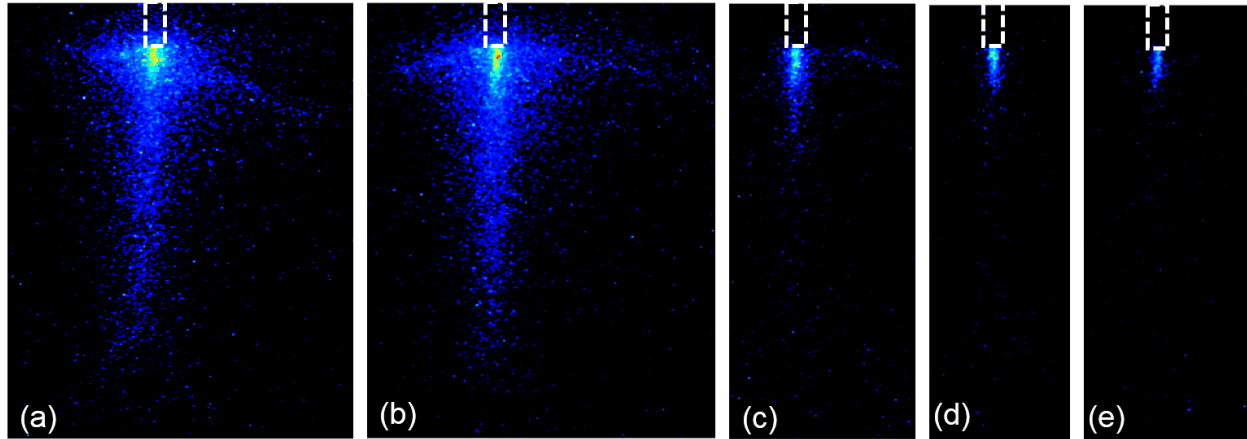


Fig. 4-16. Breakdown images of plasma jet with repetition rate at 7 kV, 200 ns pulses (a) 1 Hz, (b) 10 Hz, (c) 100 Hz, (d) 1000 Hz and (e) 5000 Hz.

As shown in Fig. 4-17, breakdown probability increased with pulse width from 200 ns to 5000 ns. The breakdown probability sharply increased with pulse width as 70% breakdown probability at 200 ns and 97% probability at 600 ns. By examining the sample images (Fig. 4-18), it seems there is no appreciable difference among different pulse widths under the investigated range. Compared with the corona discharge, the breakdown probability rose more rapidly with plasma jet in helium than with corona in air.

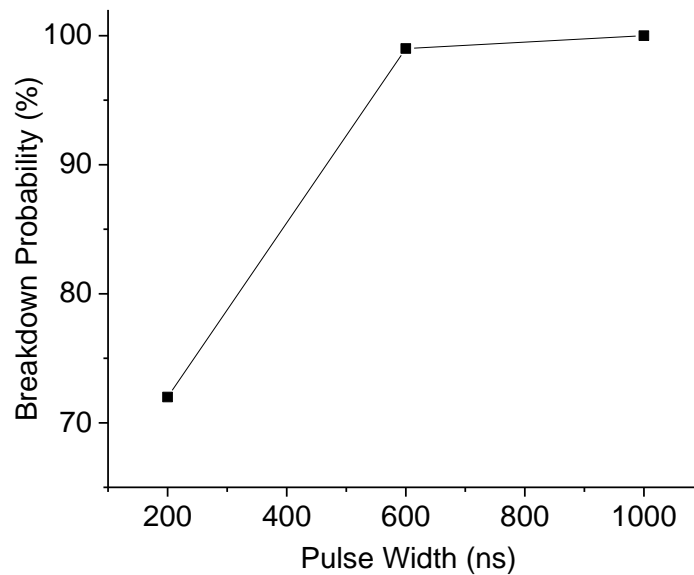


Fig. 4-17. Breakdown probability of plasma jet with pulse width (200 – 1000 ns) at 7 kV, 1 Hz with 200 ns to 1000

ns.

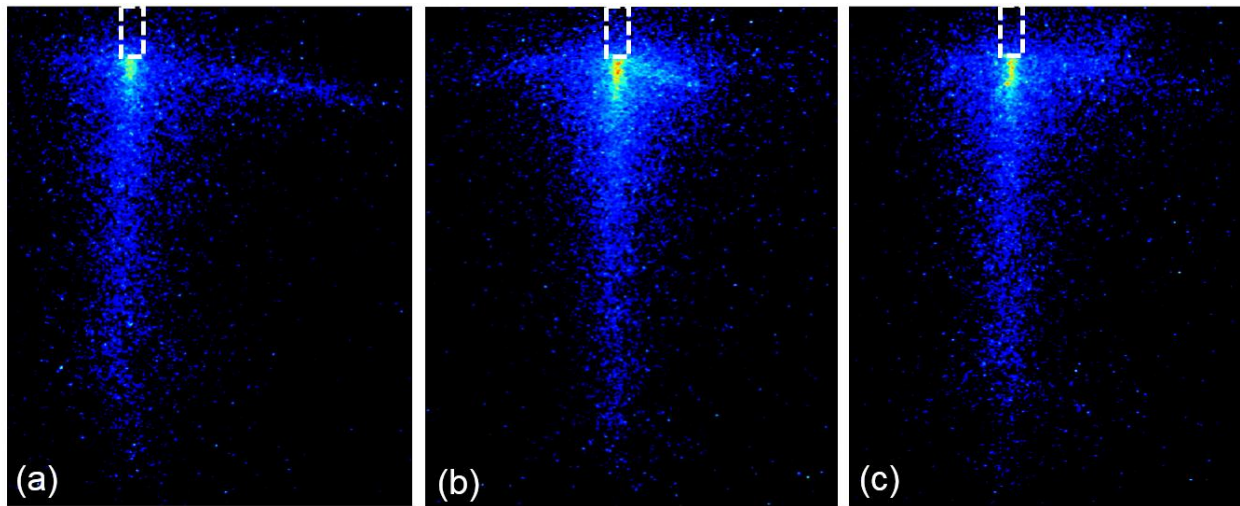


Fig. 4-18. Breakdown images of plasma jet with pulse width at 7 kV, 1 Hz with (a) 200 ns, (b) 1000 ns and (c) 5000

ns.

He flow rate is an important operating parameter in plasma jet. As shown in Fig. 4-19, results clearly shown that the breakdown probability decreased with flow rate in the range from 35 SCCM to 200 SCCM (i.e. 35, 70, 100, 150 and 200 SCCM) which are laminar flows. At He flow of 35 SCCM, the breakdown probability is about 85% which decreased down to 40% at flow rate of 200 SCCM. The sample images shown in Fig. 4-20 indicates that higher flow rate result in longer and brighter plume.

In summary, breakdown probabilities with various operating conditions has been investigated in He plasma jet. Results shown that higher amplitude, longer pulse width, and higher repetition rate could result in higher breakdown probability under the investigated conditions, while higher flow rate decreases breakdown probability from 35 SCCM to 200 SCCM. From the perspective of the single shot images, with higher amplitude, higher breakdown associated with longer plasma

plume. However, trends were negatively correlated for both pulse repetition rate and He flow, i.e. higher breakdown probability associated with shorter plume.

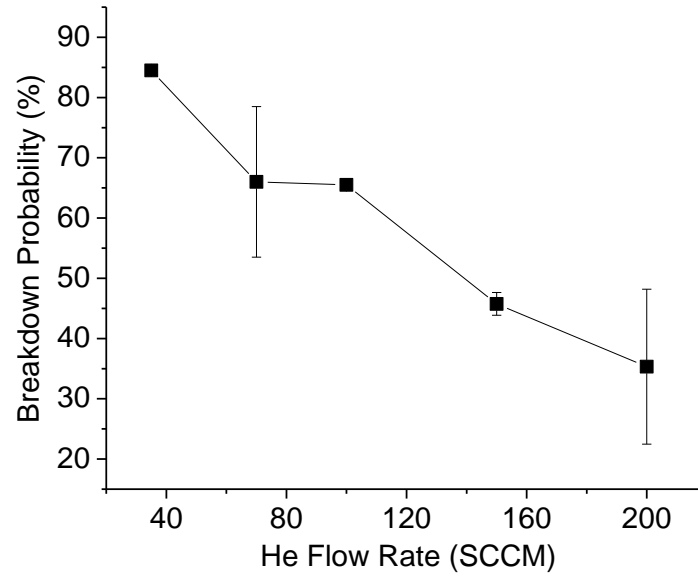


Fig. 4-19. Breakdown probability of plasma jet at 7 kV, 200 ns at 1 Hz with He flow rate from 35 SCCM to 200 SCCM.

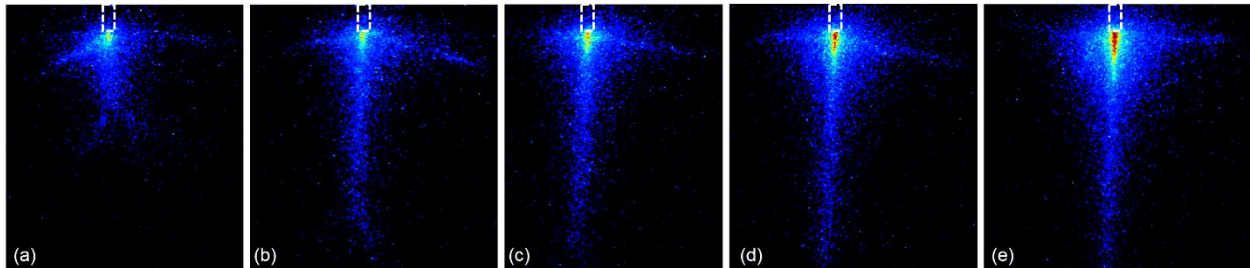


Fig. 4-20. Breakdown images of plasma jet at 7 kV, 200 ns pulses at 1 Hz with varying flow rate (a) 35 SCCM, (b) 70 SCCM, (c) 100 SCCM, (d) 150 SCCM and (e) 200 SCCM.

CHAPTER 5

CONCLUSIONS

A single-needle electrode driven by pulsed power supply with flow helium is investigated via electrical measurement and optical emission spectroscopy. Reactive species are essentially the key to understand APNPJs. They are closely related to potential applications of such discharge, especially on biomedical applications. Rich reactive nitrogen and oxygen species can be generated in our APNPJ. Short pulse rise time allows more reactive species to be generated in plasma plume and favor the generation of energetic electrons hence dominating the reaction pathways through direct electron impact reactions. When the plasma jet impinged onto a water surface, reactive species as well as the electrical characteristics of a plasma jet is greatly enhanced compared with the free jet. Effect of pulse width on OH(A-X) emissions indicate that the majority of OH intensities are produced during the rising phase of a voltage pulse.

Development of ‘guided streamer’ is important in application-wise. Operation parameters eventually result in different application effects, hence it is of great importance to study the effect of these parameters on ‘guided streamer’. It is found that increasing both voltage amplitude and He flow rate (in laminar flow region) will result in similar effect which produce longer and stronger plumes. Pulse width and repetition rate also show resemble effect on development of plasma plumes, that is, long pulse tends to have similar effect on plume as higher repetition rate which both could favor the earlier inception but lower the electric field.

The configuration of single-electrode not only can produce APNPJs with flowing of He flow but also corona discharges without gas. Memory effect generated from previous pulses favored the

breakdown probability of the next pulse. This effect seems much stronger and lasts much longer than one would expect. Seed electrons provided by memory effect allow the next pulse to retain a breakdown probability which highly depend on the level of seed electrons. If the memory effect is strong (i.e. higher seed electrons), the breakdown probability can retain in a high level. The retain ability is of great importance in atmospheric pulsed plasmas. Increasing pulse amplitude and pulse width increased breakdown probability for both corona discharge and APNPJ. Pulse repetition rate for both discharges enhanced the breakdown probability when PRR is below 5 kHz.

APPENDIX A

VOLTAGE AND CURRENT MEASUREMENTS

1. HIGH VOLTAGE PROBE (P6015A)

The high voltage probe P6015A is designed to take accurate voltage measurements between 1.5 kV and 20 kV (DC + peak AC), up to 40 kV peak for pulses (see the manual for details). It has a 100 M Ω resistance, 3.0 pF capacitance with 1000 \times attenuation. It should connect to oscilloscope with input resistance of 1 M Ω with an input capacitance of 7 pF to 49 pF [80].

A few cautions when take measurements with P6015A [80]:

1. Do not place the probe tip near the conductive surface which changes the input capacitance of the probe resulting the change of the probe compensation, hence causing the voltage pulse overshoot or undershoot regarding its true pulse amplitude.

2. Do not allow the conductor, to which the probe is attached to pass along the side of the probe body which will induce capacitance of the probe, causing the inaccurate measurements. Keep the probe perpendicular to the attached conductor.

3. Do not modify the probe tip or ground leads. At high frequency, a slightly longer wire or sharp edges will result in significant impedance change and introduce extra inductance which will result in ringing and signal distortion.

2. CURRENT MEASUREMENTS (PEARSON 6585 AND 2877)

Model 6585 has maximum peak current 500 A with usable rise time 1.5 ns. Model 2877 ($I_{\text{peak}} = 100$ A and $\tau_{\text{rise}} = 2$ ns). The current measurements, especially when the measured current is small and comparable to noise, become critically important.

To measure current accurately, we need to understand where the noise come from. Any signals that mixed with the desired signals are noises. Electromagnetic interference (EMI), Radio frequency interference (RFI) and cross talk are three common source for noise. Here I only consider the main noises come from our plasma system.

1. Fast rising pulse currents: the fast pulses may produce current ringing due to high frequency current flowing on the outside of cable shield. These noise can be suppressed by increasing the inductance of the shield through threading the cable into several ferrites (as shown in Fig. A1).

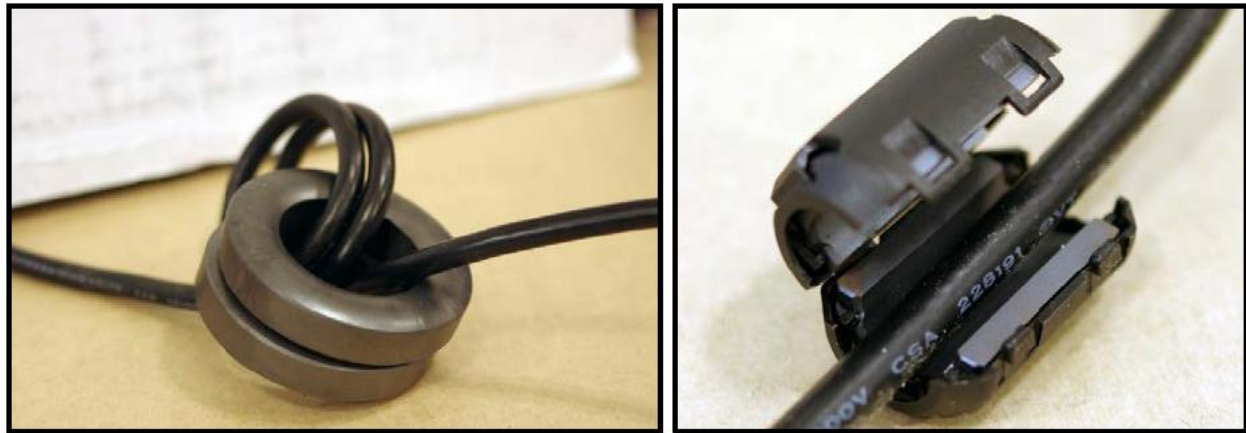


Fig. A1. Coaxial cable through two ferrites (left) and Coaxial cable through a ferrite clamp (right) [80].

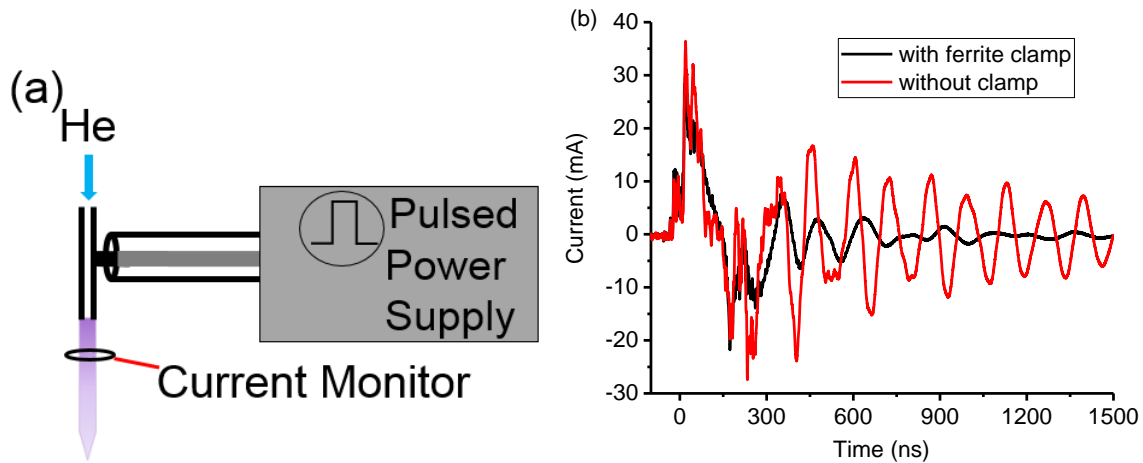


Fig. A2. (a) Experimental setup for current measurement at 8 kV, 200 ns pulse at 1 kHz with He flow rate at 164 SCCM and (b) currents measured from plasma jets using Pearson 6585 with (black solid line) and without (red solid line) two ferrite clamps.

The currents measured in our system with and without ferrite clamp are dramatically different (shown in Fig. A2 (b)). Here the inductance of the coaxial shield increased by wrapping two ferrite clamps along the cable which suppressed the noise a lot.

2. Ground loop: ground loop occurs when more than one ground connection path between two pieces of equipment, especially when there are potential difference in these different ground wires causing currents flowing which further modify the interconnect currents. The loop in our system can be describe as in Fig. A3.

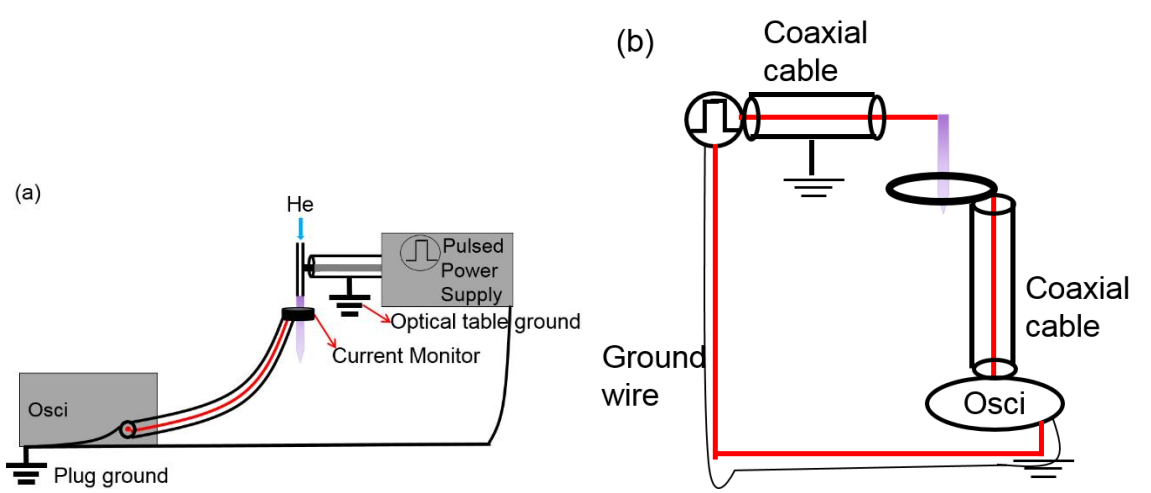


Fig. A3. (a) Experimental setup for current measurement (black line is ground wire, red is the center core) and (b) the equivalent circuit of (a).

The transmission line of the power supply is grounded to the optical table which forms one ground loop, while the coaxial cable from the current monitor formed another ground loop. The shield of the transmission line has strong current flow which is higher than shield of the coaxial cable for current monitor, eventually this current difference resulted in modified signal displayed on the oscilloscope. To eliminate this noise, one can ground the threaded mounting hole in the current monitor. A sample result is shown in Fig. A4 which compared the currents with and without grounded to the transmission line shield.

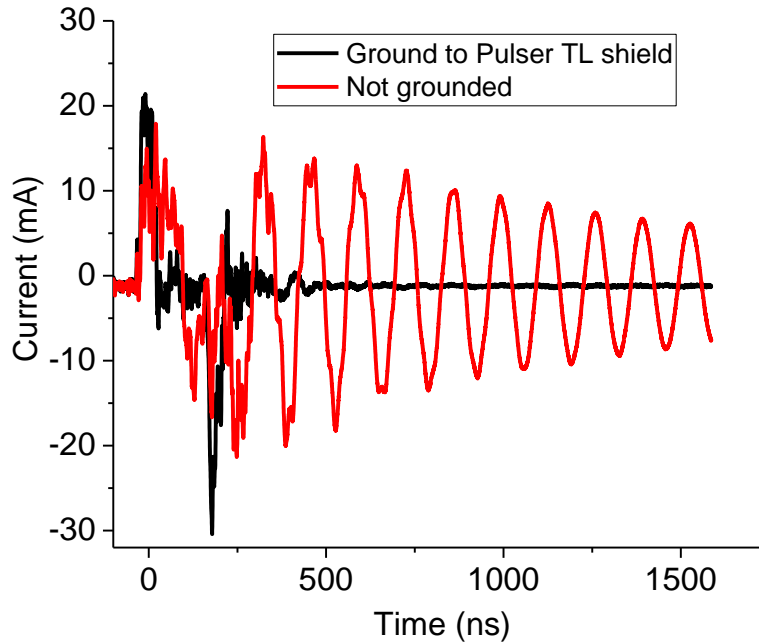


Fig. A4. Current measured using Pearson 6585 as in Fig. 3(a) with (black solid line) and without (red solid line) connecting to the transmission line shield.

3. Poor quality coaxial cable: the shield (usually braid) of the coaxial cable is quite important when dealing with high frequency signal since bad shield could allow high frequency signal to seep in or leak out. Imagine that a high frequency noise travel along the outer side of the shield which could easily affect the desired signal if the quality of the cable is poor (particularly the shield of the coaxial cable). Below (Fig. A5) showed the RG 58/U with shield coverage 70% and RG 58 C/U with 95% coverage. The measured currents with the two coaxial cable are compared and shown in Fig. A6.



CATALOG NUMBER	AWG SIZE NOM. DCR	INSULATION MATERIAL		SHIELD COVERAGE NOM SHLD DCR	NOMINAL O.D.		NOMINAL CAPACITANCE		VELOCITY OF PROPAGATION, %	NOMINAL IMPEDANCE, Ω	NOMINAL ATTENUATION	
		INCHES	mm		INCHES	mm	pF/ft	pF/m			MHz	dB/100'
C1117 RG 58/U Type 	20 Ga. Solid Bare Copper 10.1 Ω/Mft.	Solid PE		70% Tinned Copper Braid 6.0 Ω/Mft.	Black PVC		28.50	93.51	66	53	1	0.40
					0.195 4.95						10	1.20
					50	2.90						
					100	4.20						
					200	6.00						
					500	10.17						
		1000	16.50									
C1155 RG 58 C/U Type MIL-C-17G Type 	20 Ga. (19/.0071) Tinned Copper 10.8 Ω/Mft.	Solid PE		95% Tinned Copper Braid 4.3 Ω/Mft.	Non-Contaminating Black PVC		30.80	101.05	66	50	1	0.42
					0.195 4.95						10	1.50
					50	3.70						
					100	5.40						
					200	8.10						
					500	13.86						
		1000	22.80									

Fig. A5. Comparison of coaxial cable RG 58/U and 58 C/U with specifications [81].

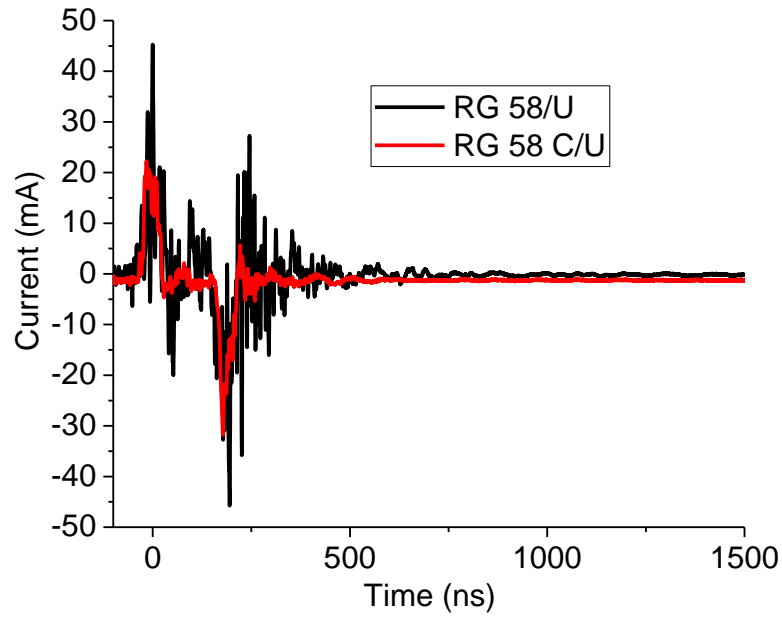


Fig. A6. Currents measured using Pearson 6585 with coaxial cable RG 58/U (black solid line) and 58 C/U (red solid line).

4. Other sources of noise: there are a lot of other noises depending on setup of one's experiments.

The important thing is to identify sources of noise.

APPENDIX B

PERMISSIONS FROM THE COPYRIGHT HOLDER

1. Reuse of IEEE graphics published in IEEE publications

IEEE permission: ‘Reusing IEEE graphics previously published in IEEE publications. You will need to request permission directly from IEEEExplore. In most cases, the only requirements will be to give full credit to the original source and to obtain the author’s approval (as a courtesy to the author). At the end of the caption, add the reference number of the articles from which the graphics are being used’ [79].

2. Reuse publications from Japanese Journal of Applied Physics

As an original author of "Effects of pulse width on He plasma jets in contact with water evaluated by OH(A-X) emission and OH₂ production" and "Ignition and dynamics of nanosecond pulsed helium streamers over a water electrode" you have the right to reuse any original figures, tables or parts of your own articles, as applicable, provided:

- The current Author Rights Policy is followed: <https://publishingsupport.iopscience.iop.org/current-policy-author-rights-policy-for-subscription-articles-for-which-the-copyright-form-was-submitted-on-or-after-26-april-2016/>
- The article(s) are cited as reference
- The copyright line including year of publication is added to the reproduced content (at the end of the figure captions): Copyright (year of publication) The Japan Society of Applied Physics

This does not apply to any material/figure which is credited to another source in the publication or has been obtained from a third party. Express permission for such materials/figures must be obtained from the copyright owner.

REFERENCES

1. Yu.P.Raizer, *Gas discharge physics*. 1991, Berlin: Springer-Verlag Berlin Heidelberg. 449.
2. Abe, H., M. Yoneda, and N. Fujlwara, *Developments of plasma etching technology for fabricating semiconductor devices*. Japanese Journal of Applied Physics, 2008. **47**(3): p. 1435-1455.
3. Niemira, B.A., *Cold Plasma Decontamination of Foods*. Annual Review of Food Science and Technology, Vol 3, 2012. **3**: p. 125-142.
4. Graves, D.B., *Low temperature plasma biomedicine: A tutorial review*. Physics of Plasmas, 2014. **21**(8).
5. Weltmann, K.D., et al., *Plasma Processes and Plasma Sources in Medicine*. Contributions to Plasma Physics, 2012. **52**(7): p. 644-654.
6. Graves, D.B., *The emerging role of reactive oxygen and nitrogen species in redox biology and some implications for plasma applications to medicine and biology*. Journal of Physics D: Applied Physics, 2012. **45**(26): p. 263001.
7. Ninomiya, K., et al., *Evaluation of extra- and intracellular OH radical generation, cancer cell injury, and apoptosis induced by a non-thermal atmospheric-pressure plasma jet*. Journal of Physics D-Applied Physics, 2013. **46**(42).
8. Kaneko, T., et al., *Gas-liquid interfacial plasmas producing reactive species for cell membrane permeabilization*. J Clin Biochem Nutr, 2017. **60**(1): p. 3-11.
9. Kurake, N., et al., *Effects of center dot OH and center dot NO radicals in the aqueous phase on H2O2 and NO2- generated in plasma-activated medium*. Journal of Physics D-Applied Physics, 2017. **50**(15).
10. Jeong, J.Y., et al., *Etching materials with an atmospheric-pressure plasma jet*. Plasma Sources Science & Technology, 1998. **7**(3): p. 282-285.
11. Jiang, C.Q., et al., *Nanosecond Pulsed Plasma Dental Probe*. Plasma Processes and Polymers, 2009. **6**(8): p. 479-483.
12. Neuber, J.U., et al., *Nanosecond Pulsed Plasma Brush for Bacterial Inactivation on Laminate*. Ieee Transactions on Radiation and Plasma Medical Sciences, 2017. **1**(4): p. 368-375.
13. Lu, X., M. Laroussi, and V. Puech, *On atmospheric-pressure non-equilibrium plasma jets and plasma bullets*. Plasma Sources Science & Technology, 2012. **21**(3).
14. Teschke, M., et al., *High-speed photographs of a dielectric barrier atmospheric pressure plasma jet*. Ieee Transactions on Plasma Science, 2005. **33**(2): p. 310-311.

15. Lu, X., et al., *Guided ionization waves: Theory and experiments*. Physics Reports-Review Section of Physics Letters, 2014. **540**(3): p. 123-166.
16. Lu, X.P., et al., *Effect of E-field on the length of a plasma jet*. Ieee Transactions on Plasma Science, 2008. **36**(4): p. 988-989.
17. Sands, B.L., R.J. Leiweke, and B.N. Ganguly, *Spatiotemporally resolved Ar (1s(5)) metastable measurements in a streamer-like He/Ar atmospheric pressure plasma jet*. Journal of Physics D-Applied Physics, 2010. **43**(28).
18. Shashurin, A., M.N. Shneider, and M. Keidar, *Measurements of streamer head potential and conductivity of streamer column in cold nonequilibrium atmospheric plasmas (vol 21, 034006, 2012)*. Plasma Sources Science & Technology, 2012. **21**(4).
19. Breden, D., K. Miki, and L.L. Raja, *Computational study of cold atmospheric nanosecond pulsed helium plasma jet in air*. Applied Physics Letters, 2011. **99**(11).
20. Naidis, G.V., *Simulation of streamers propagating along helium jets in ambient air: Polarity-induced effects*. Applied Physics Letters, 2011. **98**(14).
21. Breden, D., K. Miki, and L.L. Raja, *Self-consistent two-dimensional modeling of cold atmospheric-pressure plasma jets/bullets*. Plasma Sources Science & Technology, 2012. **21**(3).
22. Li, Q., et al., *Effects of Penning ionization on the discharge patterns of atmospheric pressure plasma jets*. Journal of Physics D-Applied Physics, 2010. **43**(38).
23. Urabe, K., et al., *Investigation of discharge mechanisms in helium plasma jet at atmospheric pressure by laser spectroscopic measurements*. Journal of Physics D-Applied Physics, 2010. **43**(9).
24. Wu, S., et al., *The Effect of Nitrogen Diffusion From Surrounding Air on Plasma Bullet Behavior*. Ieee Transactions on Plasma Science, 2011. **39**(11): p. 2286-2287.
25. Hofmann, S., A. Sobota, and P. Bruggeman, *Transitions Between and Control of Guided and Branching Streamers in DC Nanosecond Pulsed Excited Plasma Jets*. Ieee Transactions on Plasma Science, 2012. **40**(11): p. 2888-2899.
26. Walsh, J.L., et al., *Three distinct modes in a cold atmospheric pressure plasma jet*. Journal of Physics D-Applied Physics, 2010. **43**(7).
27. Chang, L., et al., *The effect of seed electrons on the repeatability of atmospheric pressure plasma plume propagation. II. Modeling*. Physics of Plasmas, 2016. **23**(12).
28. Nie, L., et al., *The effect of seed electrons on the repeatability of atmospheric pressure plasma plume propagation: I. Experiment*. Physics of Plasmas, 2016. **23**(9).

29. Xiong, Q., et al., *Length control of He atmospheric plasma jet plumes: Effects of discharge parameters and ambient air*. Physics of Plasmas, 2009. **16**(4).
30. Walsh, J.L., P. Olszewski, and J.W. Bradley, *The manipulation of atmospheric pressure dielectric barrier plasma jets*. Plasma Sources Science & Technology, 2012. **21**(3).
31. Wu, S., et al., *Effect of Pulse Rising Time of Pulse dc Voltage on Atmospheric Pressure Non-Equilibrium Plasma*. Plasma Processes and Polymers, 2013. **10**(2): p. 136-140.
32. Leiweke, R.J. and B.N. Ganguly, *Effects of pulsed-excitation applied voltage rise time on argon metastable production efficiency in a high pressure dielectric barrier discharge*. Applied Physics Letters, 2007. **90**(24).
33. Karakas, E. and M. Laroussi, *Experimental studies on the plasma bullet propagation and its inhibition*. Journal of Applied Physics, 2010. **108**(6).
34. Boeuf, J.P., L.L. Yang, and L.C. Pitchford, *Dynamics of a guided streamer ('plasma bullet') in a helium jet in air at atmospheric pressure*. Journal of Physics D-Applied Physics, 2013. **46**(1).
35. Xian, Y.B., et al., *From short pulses to short breaks: exotic plasma bullets via residual electron control*. Scientific Reports, 2013. **3**.
36. Karakas, E., M. Koklu, and M. Laroussi, *Correlation between helium mole fraction and plasma bullet propagation in low temperature plasma jets*. Journal of Physics D-Applied Physics, 2010. **43**(15).
37. Li, Q., et al., *Role of metastable atoms in the propagation of atmospheric pressure dielectric barrier discharge jets*. Journal of Applied Physics, 2010. **107**(4).
38. Naidis, G.V., *Modeling of helium plasma jets emerged into ambient air: Influence of applied voltage, jet radius, and helium flow velocity on plasma jet characteristics*. Journal of Applied Physics, 2012. **112**(10).
39. Xiong, R.H., et al., *Influence of helium mole fraction distribution on the properties of cold atmospheric pressure helium plasma jets*. Journal of Applied Physics, 2012. **112**(3).
40. Mericam-Bourdet, N., et al., *Experimental investigations of plasma bullets*. Journal of Physics D-Applied Physics, 2009. **42**(5).
41. Zhu, W.C., et al., *Characteristics of atmospheric pressure plasma jets emerging into ambient air and helium*. Journal of Physics D-Applied Physics, 2009. **42**(20).
42. Park, H.S., et al., *Optical and electrical characterization of an atmospheric pressure microplasma jet with a capillary electrode*. Physics of Plasmas, 2010. **17**(3).
43. Loeb, L.B., *Fundamental Processes of Electrical Discharge in Gases*. 1939: John Wiley.

44. Meek, J.M., *Electrical breakdown of gases*. 1978, United States: John Wiley and Sons, Ltd.
45. Raether, H., *Electron Avalanches and Breakdown in Gases*. 1964, London: Butterworths.
46. Loeb, L.B., *Basic processes of gaseous electronics*. 1960: University of California Press.
47. Rogowski, W., *Extract from impulse potential and breakdown in gases*. *Electrical breakdown in gases*, ed. J.A.Rees. 1973, New York - Toronto: John Wiley and Sons. A Halsted Press Book.
48. Wilson, R.R., *Very Short Time Lag of Sparking*. *Physical Review*, 1936. **50**(11): p. 1082-1088.
49. Xueji Xu, D.Z., *Gas discharge physics*. 1996: Fudan University Press.
50. Roth, J.R., *Industrial Plasma Engineering vol. 1*. *Industrial Plasma Engineering*. 1995: Bristol and Philadelphia: Institute of Physics Publishing.
51. Walsh, J.L., J.J. Shi, and M.G. Kong, *Contrasting characteristics of pulsed and sinusoidal cold atmospheric plasma jets*. *Applied Physics Letters*, 2006. **88**(17).
52. Xiong, Q., et al., *Pulsed dc- and sine-wave-excited cold atmospheric plasma plumes: A comparative analysis*. *Physics of Plasmas*, 2010. **17**(4).
53. Lu, X. and M. Laroussi, *Dynamics of an atmospheric pressure plasma plume generated by submicrosecond voltage pulses*. *Journal of Applied Physics*, 2006. **100**(6).
54. van Veldhuizen, E.M. and W.R. Rutgers, *Pulsed positive corona streamer propagation and branching*. *Journal of Physics D-Applied Physics*, 2002. **35**(17): p. 2169-2179.
55. Lu, X.P., et al., *A single electrode room-temperature plasma jet device for biomedical applications*. *Applied Physics Letters*, 2008. **92**(15).
56. Wang, R.X., et al., *Temporal and spatial profiles of emission intensities in atmospheric pressure helium plasma jet driven by microsecond pulse: Experiment and simulation*. *Journal of Applied Physics*, 2015. **118**(12).
57. Wang, R.X., et al., *Effect of pulse polarity on the temporal and spatial emission of an atmospheric pressure helium plasma jet*. *Plasma Sources Science & Technology*, 2016. **25**(1).
58. Xiong, Q., et al., *Experimental investigations on the propagation of the plasma jet in the open air*. *Journal of Applied Physics*, 2010. **107**(7).
59. Begum, A., M. Laroussi, and M.R. Pervez, *Atmospheric pressure He-air plasma jet: Breakdown process and propagation phenomenon*. *Aip Advances*, 2013. **3**(6).

60. Ivkovic, S.S., et al., *Measurement of electric field development in dielectric barrier discharge in helium*. Journal of Physics D-Applied Physics, 2009. **42**(22).
61. Laroussi, M., *Low-Temperature Plasmas for Medicine?* Ieee Transactions on Plasma Science, 2009. **37**(6): p. 714-725.
62. Kong, M.G., et al., *Plasma medicine: an introductory review*. New Journal of Physics, 2009. **11**.
63. Vorac, J., et al., *Measurement of hydroxyl radical (OH) concentration in an argon RF plasma jet by laser-induced fluorescence*. Plasma Sources Science & Technology, 2013. **22**(2).
64. Verreycken, T., et al., *Time and spatially resolved LIF of OH in a plasma filament in atmospheric pressure He-H₂O*. Journal of Physics D-Applied Physics, 2012. **45**(4).
65. Kanazawa, S., et al., *Observation of OH radicals produced by pulsed discharges on the surface of a liquid*. Plasma Sources Science & Technology, 2011. **20**(3).
66. Laroussi, M. and X. Lu, *Room-temperature atmospheric pressure plasma plume for biomedical applications*. Applied Physics Letters, 2005. **87**(11).
67. Fridman, G., et al., *Applied Plasma Medicine*. Plasma Processes and Polymers, 2008. **5**(6): p. 503-533.
68. Kolb, J.F., et al., *Cold atmospheric pressure air plasma jet for medical applications*. Applied Physics Letters, 2008. **92**(24).
69. Ikawa, S., K. Kitano, and S. Hamaguchi, *Effects of pH on Bacterial Inactivation in Aqueous Solutions due to Low-Temperature Atmospheric Pressure Plasma Application*. Plasma Processes and Polymers, 2010. **7**(1): p. 33-42.
70. van Gils, C.A.J., et al., *Mechanisms of bacterial inactivation in the liquid phase induced by a remote RF cold atmospheric pressure plasma jet*. Journal of Physics D-Applied Physics, 2013. **46**(17).
71. Song, S.T., J. Lane, and C.Q. Jiang, *Comparison Study of Spatiotemporally Resolved Emissions of Nanosecond Pulsed Microplasma Jets*. Ieee Transactions on Plasma Science, 2018. **46**(3): p. 587-593.
72. Bruggeman, P.J., et al., *Plasma-liquid interactions: a review and roadmap*. Plasma Sources Science & Technology, 2016. **25**(5).
73. Jiang, C.Q. and S.T. Song, *Ignition and dynamics of nanosecond pulsed helium streamers over a water electrode*. Japanese Journal of Applied Physics, 2017. **56**(4).
74. Kajiyama, H., et al., *Future perspective of strategic non-thermal plasma therapy for cancer treatment*. J Clin Biochem Nutr, 2017. **60**(1): p. 33-38.

75. Norberg, S.A., et al., *Atmospheric pressure plasma jets interacting with liquid covered tissue: touching and not-touching the liquid*. Journal of Physics D-Applied Physics, 2014. **47**(47).
76. Sasaki, S., et al., *Characterization of plasma-induced cell membrane permeabilization: focus on OH radical distribution*. Journal of Physics D-Applied Physics, 2016. **49**(33).
77. Joh, H.M., et al., *Effects of the pulse width on the reactive species production and DNA damage in cancer cells exposed to atmospheric pressure microsecond-pulsed helium plasma jets*. Aip Advances, 2017. **7**(8).
78. Song, S.T., E.B. Sozer, and C.Q. Jiang, *Effects of pulse width on He plasma jets in contact with water evaluated by OH(A-X) emission and OHaq production*. Japanese Journal of Applied Physics, 2019. **58**(6).
79. Huang, B.D., et al., *The effect of the pulse repetition rate on the fast ionization wave discharge*. Journal of Physics D-Applied Physics, 2018. **51**(22).
80. Slobodov, I., *High Voltage Nanosecond Pulse Measurement Techniques*. 2016: p. https://www.eagleharbortech.com/wp-content/uploads/2016/06/High-Voltage-Nanosecond-Pulse-Measurement-Techniques_TN1.pdf.
81. Automation, A.E.: p. <https://www.alliedelec.com/m/d/b6728848b37672a49202d050a0ff49b5.pdf>.
79. http://ieeauthorcenter.ieee.org/wp-content/uploads/IEEE_Style_Manual.pdf
80. P6015A manual, [https://download.tek.com](https://download.tek.com/manual) › manual.

VITA

Shutong Song was born in China. He received his B.S. degree in Applied Physics from Donghua University in Shanghai, China in 2010 and his M.S. degree in Plasma Physics from Donghua University in Shanghai, China in 2013. He joined Dr. Chunqi Jiang's group at department of electrical & computer engineering at Old Dominion University as a graduate student in 2014. Before that, he spent one and a half years in a semiconductor company in Shanghai, China from 2013 to 2014. His Ph.D. research focus on non-equilibrium plasma jets at atmospheric pressure, including plasma diagnostic using high speed imaging, spectroscopy and laser-induced fluorescence. Also, he has a simulation background in atmospheric pressure dielectric barrier glow discharges which focused on stability research of atmospheric pressure glow discharges. He has published authored and co-authored 7 papers in peer-reviewed journals and presented his research work in more than 10 scientific conferences. He also received a student travel award to present his work at GRS and GRC Plasma Processes Conference held in Smithfield, RI in 2018.